Università degli Studi di Torino
Scuola di Dottorato in Scienza ed Alta Tecnologia

Indirizzo di Fisica ed Astrofisica

Alignment of CMS Tracker detector using cosmic ray particles and its impact on early physics performance

Roberto Castello

Supervisor: Dr. Ernesto Migliore

Date of dissertation
22^{nd} January 2010

Candidate
Roberto Castello

Supervisor
Dr. E. Migliore (Università degli Studi di Torino)

Degree board
Dr. A. Andreazza (Università degli Studi di Milano)
Dr. J. Alcaraz Maestre (Universitad Autonoma de Madrid)
Dr. A. Pellegrino (Vrije Universiteit, Amsterdam)
Dr. E. Maina (Università degli Studi di Torino)

PhD coordinator
Prof. G. Boffetta (Università degli Studi di Torino)

Ai miei *maestri*.

Made weak by time and fate, but strong in will
To strive, to seek, to find, and not to yield.
A. Tennyson, *Ulysses* (1842).

Aknowledgments

I must admit that I have learnt a lot during my PhD experience. Both inside and outside my office. I would like to say a word of thanks to people who somehow contributed to this.
My deepest gratitude goes to Ernesto, for the infinite care he has dedicated to me and to the quality of my work. To the CMS Torino group members, in particular Amedeo, Chiara, Nicolò, Nadia, Lino, Marco, Nicola and Vincenzo. My sincere thanks to Alessandra for her constant presence and interest in my activity.

A word of thanks to the youngest branch of the CMS Torino group, who now lies around the world: Sara, Gianluca and Riccardo for their precious advice.

I could not help mentioning the CMS Tracker alignment people I have worked with since the first module aligned at TIF: Gero Flucke, Roberto Covarelli, Johannes Hauk , Matthias Edelhoff, Daniel Sprenger, Frank Meier and Zijin Guo. My sincere admiration goes to Andrei Gritsan and Martin Weber.
Jula, Nhan and Alessio: it has been a pleasure and a honor working with special people like you.

Thanks to Domenico Giordano, Fabrizio Palla, Tommaso Dorigo and Marco De Mattia for the help in my work experience outside the Tracker alignment activity and to Attilio Andreazza for the careful reading and comments provided to this work.

A thought to friends who simply *have been*, in their own way, during this experience: Cristina, Paolo, Giorgia, Daniele, Susy, Cecilia, Filippo, Stefano, Marco and Matteo.
To my parents and Claudia, for all that really counts.

Contents

Introduction

The prime motivation of the Large Hadron Collider (LHC) is to investigate the hidden sectors of the *Standard Model* of fundamental interactions. In particular, the main goal of the physics program is the study of the electroweak symmetry breaking for which the Higgs mechanism is presumed to be responsible, by searching for the intermediate boson or super-symmetric partners explaining the mechanism.
Those sectors are accessible only at high energy scale and therefore the pp collisions occurring at LHC are designed to reach an energy of 7 TeV per beam, providing a centre of mass energy of $\sqrt{s} = 14\,\text{TeV}$ at the design luminosity of $\mathcal{L} = 10^{34}\text{cm}^{-2}\,\text{s}^{-1}$, when working at full performance. The major physics signatures expected for these processes at TeV scale are muons and the Compact Muon Solenoid (CMS), one of the four LHC experiments, has been designed for the identification and the measurement of the kinematics of this lepton. The high luminosity and the high energy of the colliding protons lead to challenging demands to the detector: for the particles momentum measurement, a precise inner tracking system, the Tracker, has been developed, in order to provide high resolution in the measurement of muon momentum. For a system like Tracker, with more than 15 000 independent modules, one of the main source of systematic on this measurement, and consequently on the related physics observables, is given by the unknown positions of modules inside the geometry. Given the inaccessibility of the detector volume during collisions, the most accurate way to determine the silicon module positions is to use the data from the detector itself when traversed *in situ* by charged particles.
This thesis is devoted to the *alignment* of the full CMS Tracker using cosmic rays particle, the only particles available before collisions.
A first experience, ahead of installation of the Tracker in the underground cavern, came from the alignment test performed at the Tracker Integration Facility during Summer 2007: in this configuration 15% of the Tracker was powered on and about 5 millions of cosmic rays were collected. I have studied alignment strategies for this scenario using one of the three CMS track based alignment algorithms, *Millepede*, based on a linearized least square combined fit of alignment parameters and track parameters (Chapter 3). But the real challenge came up with the alignment of the full Tracker using

the cosmic rays data from the CMS Cosmic Runs at Four Tesla, CRAFT (Chapter 4): having Tracker operating together with all other CMS subdetectors for the first time and the possibility to measure the momentum of the cosmic muon tracks using the magnetic field, offered a new opportunity to tune and to consolidate strategies for providing the desired alignment precision level. I contributed to the study of an alignment strategy with Millepede algorithm (called the *global* method), which together with the combination of the HIP algorithm (called *local* method) strategy, led to a precision in the position of the modules with respect to the cosmic ray trajectories of 3-4 μm in the barrel and 3-14 μm in the endcap. Furthermore I studied possible non-trivial trasformations of the geometry, the so called *weak* modes, which are χ^2 invariant and are of large concern. Using cosmic ray tracks as input, nine systematic distorsions have been investigated, in order to test the sensitivity to the alignment, and the track based alignment capability in solving them.
Finally I studied the impact of the remaining misalignment after CRAFT, properly modeled by a misalignment scenario, on a simulated sample of resonance decays ($Z \rightarrow \mu\mu$ and $\Upsilon \rightarrow \mu\mu$) expected after $\int \mathcal{L}dt = 10$ pb^{-1} (Chapter 5). Exploiting an existing method based on a multivariate likelihood approach, I have determined the scale corrections and the momentum resolution as a function of the muon kinematics variables, which are essential for performing first accessible precision measurements during the collision phase.

Chapter 1

Physics at the Large Hadron Collider

The Standard Model (SM) of fundamental interactions of particles is built on two gauge theories [1, 2, 3]. The former is the theory of electroweak interactions, that unifies the electromagnetic and the weak interactions, the latter is the theory of strong interactions or Quantum Chromo Dynamics. The SM for weak and electromagnetic interactions is constructed on a gauge theory with four gauge fields corresponding to massless bosons. Since only the photon is massless, whereas W and Z are massive, something has to happen in order to give mass to the bosons. The masses of the gauge fields, as well as the fermions, in the SM are generated by spontaneous symmetry breaking. The theory describes its phenomenology by the Higgs mechanism [4]. The implication of this model is the presence of a new scalar particle, the Higgs boson, which has not yet been experimentally observed. If the Higgs boson does not exist, some other phenomena should appear. However, even in presence of a Higgs boson, additional new physics can be required, depending on its mass. In fact only a limited range of Higgs masses are compatible with the stability of the SM up to the Planck scale (10^{19} GeV): a very different mass would imply a breakdown of the Standard Model and give an indication of the scale at which new physics would become evident.
The LHC collider was conceived to accomplish the important task of checking the consistency of the SM at energy scales up to about 1 TeV and finally solving the electroweak symmetry breaking puzzle. Although the investigation of this mechanism is the LHC main goal, a wide research program, both in the SM and beyond, has been developed.

1.1 Experimental tests of the Standard Model

The SM has been successfully tested in the last 40 years, starting from the *Gargamelle* experiment (discovery of weak neutral currents), coming to the

UA1/UA2 experiments (Z and W boson discovery), until the more recent *LEP*, *SLC* and *Tevatron* colliders (precision test of the SM observables).

The UA1 experiment, designed for colliding proton with antiproton at $\sqrt{s} = 540\,\text{GeV}$, led to the discovery of the W boson and to a first determination of its mass: $M_W = (80.5 \pm 0.5)\,\text{GeV}$[1]. After this important scientific achievement, the center of mass energy was increased up to 630 GeV and this allowed for the discovery of Z boson and the measurement of its mass: $M_Z = (93.0 \pm 2.9)$ GeV. A first experimental test of the parameters of the SM was therefore possible:

$$M_W^2 = M_Z^2 \cdot \cos^2\theta_W \quad \rightarrow \quad \sin^2\theta_W = 0.220 \pm 0.009 \tag{1.1}$$

After the Z and W boson discovery, the real challenge became the measurements of their properties to an high precision level, as a test of the validity of the SM predictions. Particular emphasis was given to the following quantities:

- Z e W boson mass measurement to a precision level of 10^{-5} e 10^{-4}, respectively.
- the number of leptonic families
- measurement of Z boson couplings with fermions (leptons and quarks, in particular b and c quark), particularly the Weinberg angle ($\sin^2\theta_W$) with an uncertainty better than per mill.
- the non abelian coupling among bosons in the SM (Triple and Quartic Gauge Coupling)
- quark top and Higgs boson discovery.

One of the experiments designed for measuring these quantities was the Large Electron Positron collider (LEP), an electron-positron collider at a centre of mass energy of 100/200 GeV during its first/second run phase (LEP-I/LEP-II). LEP-I achieved the first four goals of the list and the obtained precision allowed to estimate, through radiative corrections to the observables, the most probable value for the Higgs boson mass, even if not directly observed, to be $M_H = 96^{+60}_{-38}\,\text{GeV}$.
In the 1995, the $\sqrt{s} = 2\,\text{TeV}$ proton-antiproton collisions at the Tevatron machine led to the discovery of the top quark: the measurement of its mass added more precision to the global electroweak fit and allowed to set more stringent indirect bounds to the Higgs boson mass.

[1] In this thesis, mass and momentum will be expressed in natural units, where $\hbar$=1 and c=1.

Observables like the top and $W^{\pm}$ masses and Z decay parameters are logarithmically sensitive to m_H through radiative corrections. These data can therefore be fitted taking the Higgs mass as a free parameter. The outcome of the procedure [5], combining results from various experiments, is summarised in the left plot of Figure 1.1. The plot shows the value of $\Delta\chi^2 = \chi^2 - \chi^2_{min}$ as a function of m_H. The solid curve is the result of the fit, while the shaded band represents the uncertainty due to so far not calculated higher order corrections. Fit privileges low values of the Higgs mass. An upper limit of 157 GeV was set at 95 % confidence level (C.L.): this limit increases to 186 GeV when including the LEP-II direct search.

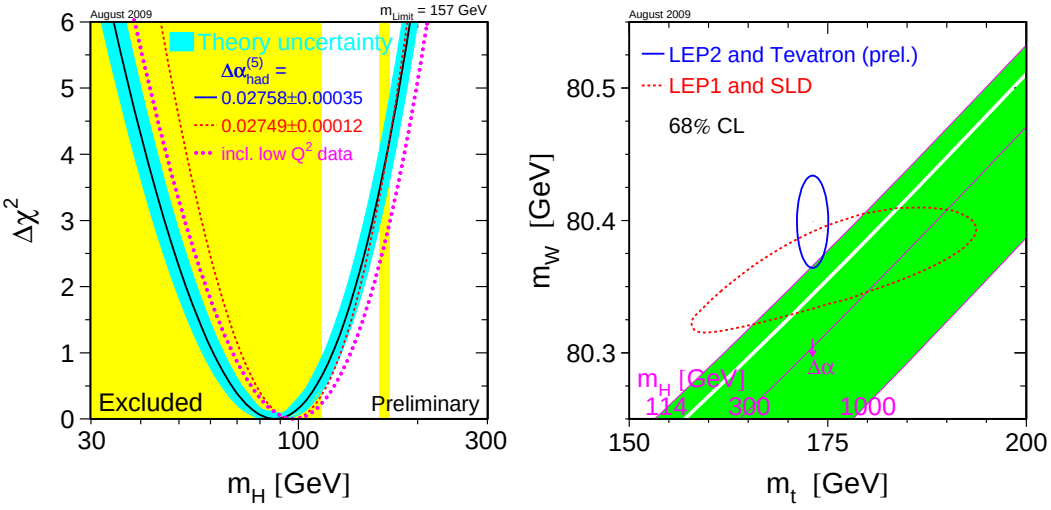

Figure 1.1: *Left plot.* $\Delta\chi^2$ *of the fit of electroweak measurements from LEP, SLD and Tevatron as a function of the Higgs mass. The vertical yellow bands shows the* 95% *CL exclusion limit on* m_H *from the direct searches at LEP-II and Tevatron. Right plot. The comparison of the indirect constraints on* m_W *and* m_t *based on LEP-I/SLD data (dashed contour) and the direct measurements from the LEP-II/Tevatron experiments (solid contour). In both cases the* 68% *C.L. contours are plotted. Also shown is the SM relationship for the masses as a function of the Higgs mass in the region favoured by theory (*$M_H < 1000\,\text{GeV}$*) and allowed by direct searches (*$114 < M_H < 170\,\text{GeV}$ *and* $M_H < 180\,\text{GeV}$*) [5].*

The electroweak results obtained up to now can be also used to determine the top quark and the W masses indirectly and the results can be compared to the direct measurements performed at Tevatron and LEP-II. This is illus-

trated in the right plot of Figure 1.1 which also shows the SM prediction for the Higgs mass between 114 and 1000 GeV. The indirect and direct measurements of m_W and m_t are in good agreement. To have the same weight on the Higgs mass prediction, the precision on the top mass (Δm_t) must be increased in order to have $\Delta m_W \sim 7 \cdot 10^{-3}\, \Delta m_t$.

LEP-II and Tevatron investigated directly the production channel of the boson via W and Z associated production (or Higgs-strahlung) using $e^+e^- \to ZH \to Xb\bar{b}$ (LEP-II) and $p\bar{p} \to WH \to l\nu b\bar{b}$ (Tevatron) decay channels. Since it was not observed, an inferior limit on the Higgs mass was set to $M_H > 114.3\,\text{GeV}$ by LEP-II and an exclusion range $163 < M_H < 166\,\text{GeV}$ (95% C.L.) was confirmed by Tevatron collaboration during 2009. The exclusion bands are reported in yellow on the left plot of Figure 1.1.
Further limits are imposed from the theoretical calculation, predicting the validity of the Standard Model up to the Plank scale if the Higg mass is in the range $130 < M_H < 180\,\text{GeV}$.

1.2 The Large Hadron Collider

To explore the hidden sectors of the SM and in particular the Higgs mechanism, searching for the intermediate boson or its super-symmetric partner, the Large Hadron Collider accelerator was built [6].
The need to investigate any new physics process at the TeV scale requires a challenging machine, able to accelerate particles at a high energy and providing collisions with high luminosity. These requirements dictated the main features of the machine:

- a hadron collider: the fundamental constituents entering in the scattering are the partons which carry a variable fraction x of the four-momentum of the particles in the beam. Therefore the center-of-mass energy of the hard scattering process $\sqrt{\hat{s}}$ can span several orders of magnitude. The design center-of-mass energy for hadronic collisions is $\sqrt{s} = 14\,\text{TeV}$. In this way, partons momentum fractions $x_1, x_2 \approx 0.15 - 0.20$ of the incoming protons momenta, give $\sqrt{\hat{s}} = \sqrt{x_1 x_2 s} \approx 1 - 2\,\text{TeV}$, the energy range to be explored. With respect to an electron-positron machine, it is easier to accelerate protons to high energy since the energy lost for synchrotron radiation, proportional to γ^4 (where $\gamma = E/m$), is much lower than for the electrons.

- a proton-proton collider: with respect to a proton-antiproton machine, it is easier to accumulate high intensity beam of protons. Furthermore, the Higgs production process is dominated by gluon fusion, and therefore its cross section is nearly the same in proton-antiproton and

proton-proton collision.

- a high luminosity collider. To compensate for the low cross section of the interesting processes the LHC must have a very high luminosity: the very short bunch crossing interval (25 ns, i.e. a frequency of 40 MHz) and the high number of bunches accelerated by the machine (2808 per beam) will allow to reach the peak luminosity of $10^{34}\,\mathrm{cm}^{-2}\,\mathrm{s}^{-1} = 10\,\mathrm{nb}^{-1}\mathrm{s}^{-1}$.

The idea behind the LHC is to reuse the existing 27 Km long LEP tunnel to install the new collider. The parameters of the machine are summarized in Table 1.1.

Parameters	**p-p**	**Pb-Pb**
Circumference (km)	26.659	
Centre of mass energy (TeV)	14	1148
Dipole magnetic field (T)	8.3	
Number of particles per bunch	1.1×10^{11}	8×10^{7}
Number of bunches	2808	608
Bunch length (mm)	53	75
Bunch crossing rate (MHz)	40.08	0.008
Design Luminosity ($cm^{-2}s^{-1}$)	10^{34}	2×10^{27}
Beam radius at interaction point (μm)	15	

Table 1.1: *LHC parameters for p-p and Pb-Pb ($^{208}Pb^{82+}$) collisions.*

Figure 1.2 shows the cross sections and the production rate at LHC of interesting processes as a function of the center-of-mass energy and of the mass of the produced particle. In Table 1.2 the cross section and the number of events produced for a given process per experiment at a luminosity of $\mathcal{L} = 2 \cdot 10^{33}\mathrm{cm}^{-2}\,\mathrm{s}^{-1}$ are reported.

Process	σ	**Events/sec**	**Events/year**
$W \to e\nu$	20 nb	15	10^8
$Z \to ee$	2 nb	1.5	10^7
$t\bar{t}$	1 nb	0.8	10^7
$b\bar{b}$	0.8 mb	10^5	10^{12}
gg (m= 1 TeV)	1 pb	0.001	10^4
H (m= 0.8 TeV)	1 pb	0.001	10^4
H (m= 0.2 TeV)	20 pb	0.01	10^5

Table 1.2: *Expected cross sections and number of events per second and per year for one experiment at LHC at $\mathcal{L} = 2 \cdot 10^{33}\mathrm{cm}^{-2}\,\mathrm{s}^{-1}$.*

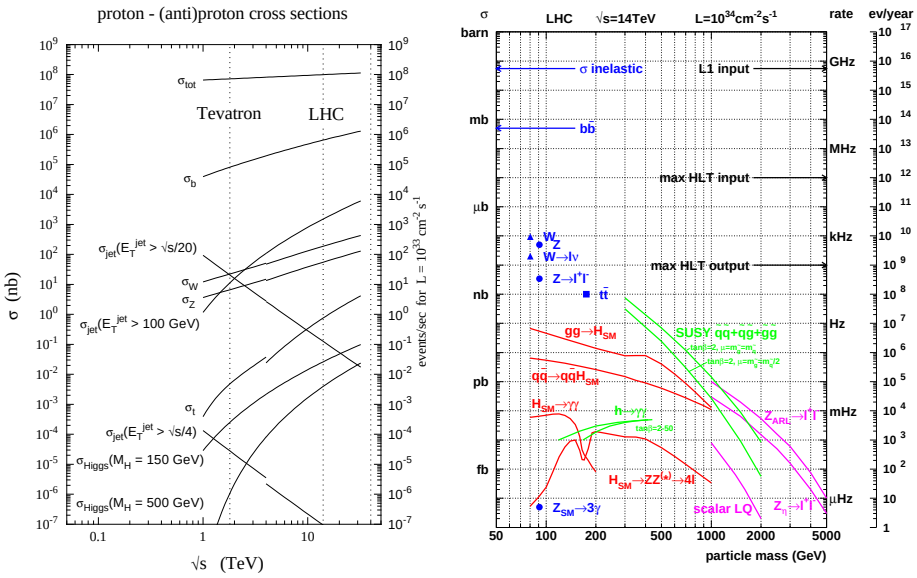

Figure 1.2: *Cross section as a function of the center-of-mass energy (left) and rate of events at LHC as a function of the mass of the produced particle (right) for interesting processes [7].*

One very remarkable aspect of LHC physics is the overwhelming background rate compared to the interesting physics processes: the Higgs production, for instance, has a cross section at least ten orders of magnitude smaller than the total inelastic cross section, as shown in Figure 1.2. In fact, the bulk of the events produced in pp collisions is either due to low p_T scattering, where the protons collide at large distance, or to the QCD high p_T processes of the type $q_i\bar{q}_i \rightarrow q_k\bar{q}_k$, $gg \rightarrow gg$, or $q_ig \rightarrow q_ig$. All these events are collectively called *minimum bias* and in LHC studies are in general considered uninteresting since they constitute a background for other processes, where massive particles like the Higgs are created in the hard scattering. The cross section for the Higgs boson production increases steeply with the center of mass energy, while the total cross section remains almost constant. Therefore the highest center of mass energy should be used.
Finally, the fact that the two partons interact with unknown energies implies that the total energy of an event is unknown. The proton remnants, that carry a sizable fraction of the proton energy, are scattered at small angles and are predominantly lost in the beam pipe, escaping undetected. Experimentally, it is therefore not possible to define the total and missing energy of the event, but only the total and missing transverse energies. Thus, all the interesting physics observable are measured in the plane transverse to the beams.

1.3 The Higgs boson search at LHC

The main processes which contribute to the Higgs production in a pp collision at the energy scale reached by LHC are shown in the diagrams in Figure 1.3. The fundamental interaction takes place between the partons, i.e. quark and gluons: the gluon fusion is the dominant process on the whole m_H spectrum and only at very high masses the vector boson fusion becomes comparable (see Figure 1.4). Cross sections are typically of the order of few picobarns, which at the LHC design luminosity correspond to rates of about $10^{-2}Hz$. In the gg fusion, since the Higgs coupling with the fermion is proportional to the squared fermion mass, the main contribution comes from the diagram in which the quark exchanged in the loop is the heaviest, i.e. the top quark ($m_t = 171.4 \pm 2.1\,\text{GeV}$ [9]).

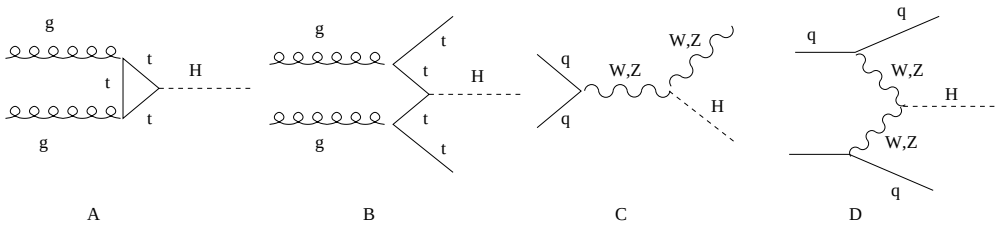

Figure 1.3: *Higgs boson production mechanisms at tree level in proton-proton collisions: gluon-gluon fusion (a), $t\bar{t}H$ associated production (b), W and Z associated production or Higgsstrahlung (c), VV fusion (d).*

Even if other processes have small cross section, they can have a clear experimental signature, and therefore being easily detectable. The WW scattering has on average a cross section about 5 to 10 times smaller than that of gg fusion, but this channel is extremely promising thanks to its clean experimental signature as the presence of two spectator jets provides a powerful tool for tagging the signal events. The associated production channels $q_i\bar{q}_j \to WH$ or $q_i\bar{q}_j \to ZH$ where an off-shell boson is produced and radiates a Higgs, have very small cross sections, except for very low m_H. Also $gg, q_i\bar{q}_j \to t\bar{t}H$ has a cross section almost 100 times smaller than that of gluon-gluon fusion. However, also in this case a powerful signature is given by the additional bosons or jets in the final state.
Once produced, the Higgs can decay in different ways, according to its mass. The branching ratios for different decay channels as a function of the Higgs mass are shown in Figure 1.5.

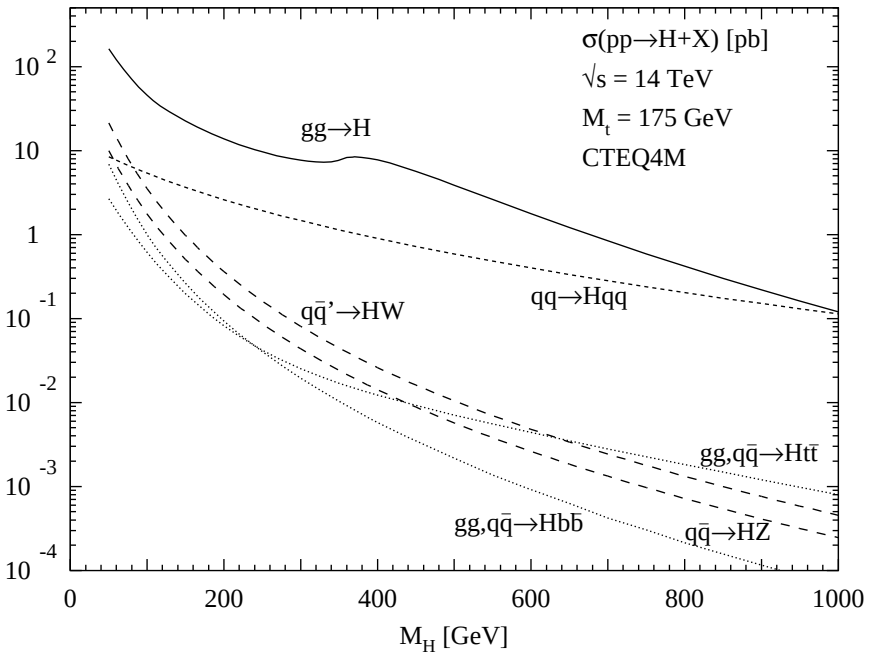

Figure 1.4: *Higgs boson production cross sections at* $\sqrt{s} = 14\,\text{TeV}$ *as a function of the Higgs boson mass.The cross sections contain higher order corrections and the CTEQ4M PDF has been adopted [8].*

They can be interpreted on the basis of the Higgs couplings, being proportional to the fermion masses and to the square of the boson masses.

Low mass Higgs ($m_H < 130\,\text{GeV}$)

The heaviest available fermion is the b quark and $H \to b\overline{b}$ dominates. However, this decay channel is difficult to observe at the LHC because of the huge QCD background. In this mass region the most promising channel is $H \to \gamma\gamma$ which despite the very low branching ratio ($\sim 10^{-3}$) has a very clean signature. The signal should appear as a narrow peak over the continuum background $q\overline{q}, gg \to \gamma\gamma$, but excellent photon energy and angular resolution are required as well as good π^0 rejection.

Intermediate mass Higgs ($130 < m_H < 500\,\text{GeV}$)

The production of WW and ZZ pairs becomes possible; the branching ratio is high, but purely hadronic final states are again not accessible. The Higgs decay in four leptons is the *golden* channel: even with a low branching ratio, it has a clean final state and does not suffer from irreducible background. The channel $H \to WW$ has the disadvantage that experimentally accessible

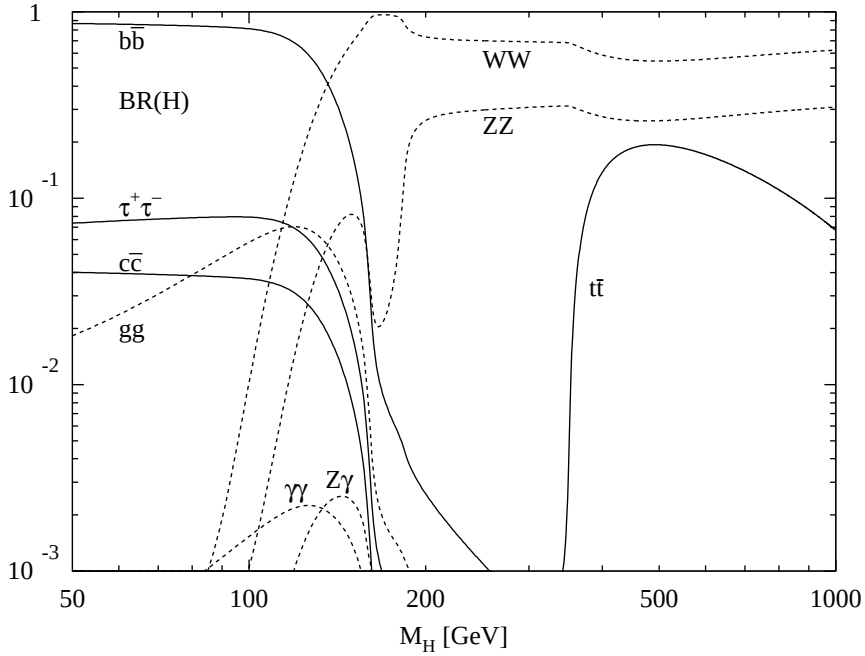

Figure 1.5: *Branching ratios for different Higgs boson decay channels as a function of the Higgs boson mass.*

final states ($l\nu l\nu$,$l\nu jj$) have at least one neutrino that escapes detection; however it will be a good discovery channel, especially for $m_H \sim 2m_W$ where the WW production is at threshold and the ZZ branching ratio drops to 20%.

High mass Higgs ($m_H > 500\,\mathrm{GeV}$)

The cross section becomes low and semi-leptonic $l\nu jj$ and $lljj$ final states have to be used. The Higgs width becomes also very broad so that the reconstruction of a mass peak becomes difficult.

1.4 Other physics at LHC

1.4.1 Z and W boson production

The cross sections of W and Z bosons production at LHC will be huge: $\sigma(pp \to W \to l\nu) \sim 20\,\mathrm{nb}$, $\sigma(pp \to Z \to ll) \sim 2\,\mathrm{nb}$. Moreover the W and Z decay processes have been measured with high accuracy in previous experiments. Thus these processes will play a key role during the first data taking at LHC allowing to test the detector performances (calibration of the scale of muon momentum, alignment of the muon system and of the inner tracker and understanding of the track reconstruction) and tune the Monte Carlo

programs used to describe the physics processes. The study of Z and W events will also improve the knowledge of the Parton Distribution Functions (PDF) at LHC scale and it will provide a raw luminosity monitoring. The actual knowledge of the PDF derives mainly from deep inelasting scattering experiments, like H1 and ZEUS. The extrapolation of those functions to the LHC energy scale is one of the main systematic uncertainties in the measurement of the cross section of a physics process [10, 11, 12]. Using the angular distribution of the leptons produced from $pp \to WX$ and $pp \to ZX$ decays is possible anyway to reduce this uncertainty. The kinematic region accessible at LHC is visible in Figure 1.6.

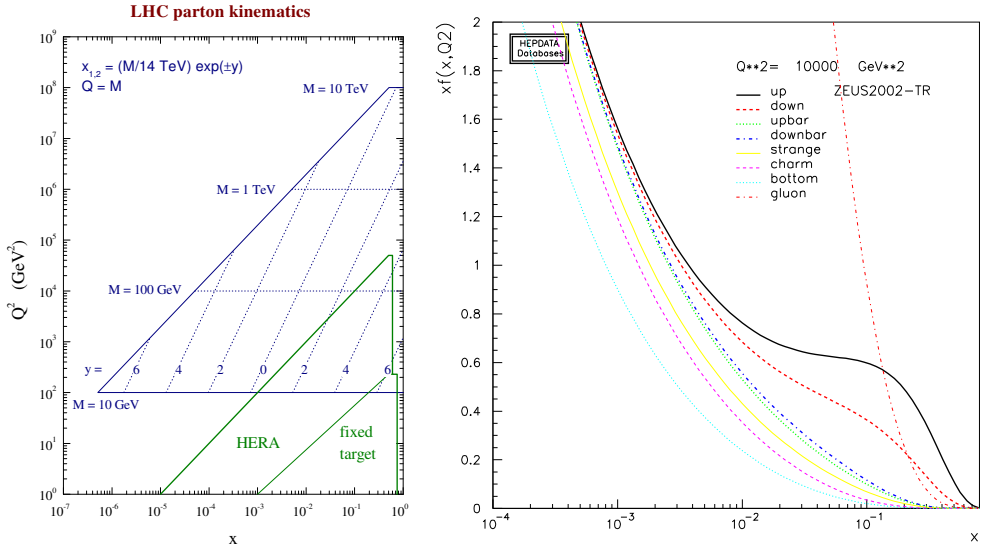

Figure 1.6: *Left. Kinematic region in the (x, Q^2) plane, accessible at LHC. Right. PDFs distribution at the scale* $Q^2 = 10\,000\,\mathrm{GeV}^2$ *[12].*

1.4.2 Top quark mass measurement

The most promising channel for the measurement of the top mass is $t\bar{t} \to W^+W^-b\bar{b}$ with one leptonic and one hadronic W decay, where the hadronic part is used to reconstruct the top mass and the leptonic part to select the event. The main source of uncertainty will be the jet energy scale, which is affected by the accuracy of the fragmentation model, the knowledge of the gluon radiation and the response of the detectors. The final uncertainty on m_t will be better than 2 GeV. This will constrain the Higgs mass to better

than 30% but, in order not to become the dominant source of uncertainty, the W mass will have to be measured with a precision of about 15 MeV.

1.4.3 B-physics and CP violation

In the field of b-physics, LHC will benefit from a very large $b\bar{b}$ production cross section. The main interest is the study of the decays of neutral B mesons, and in particular of the CP violation in the $B_d^0 - \bar{B}_d^0$ and $B_s^0 - \bar{B}_s^0$ system. B decays can be identified in leptonic final states, especially in the case of muons. However these leptons are usually soft and the identification is difficult due to the high backgrounds and pile-up. One LHC experiment, LHCb, is dedicated to b-physics which will be studied also by ATLAS and CMS in the low-luminosity phase.

1.4.4 Supersimmetry

Supersymmetry (SUSY) is a theory that introduces a new symmetry between bosons and fermions [13]. SUSY predicts that each particle has a supersymmetric partner whose spin differs by one half.
The simplest supersymmetric model, called the Minimal Supersymmetric Standard Model (MSSM), predicts the existence of two Higgs doublets, corresponding to five Higgs particles: two charged bosons, $H^{\pm}$, two scalar bosons, h and H and one pseudo-scalar, A. At tree level, all masses and couplings depend on two parameters, chosen as the mass of the A boson, m_A, and the ratio of the vacuum expectation values of the two Higgs doublets, $\tan\beta$.
In most of the parameter space, charged Higgs bosons decay predominantly to $\tau\nu$. For the neutral Higgs bosons, the decays to vector bosons are suppressed, so that the golden channels described for the case of a SM Higgs will not be observable. The dominant decays modes are those to $b\bar{b}$ and $\tau^+\tau^-$ but the former is hidden by the large background of b-jets. The observation of MSSM Higgs bosons will therefore rely on the identification the leptons coming from τ decays and of τ-jets.

1.4.5 Search for new massive vector bosons

The detector requirements for high momenta can be determined by considering decays of high-mass objects such as $Z' \to e^+e^-$ and $\mu^+\mu^-$. The discovery of an object like a Z' boson will be very likely limited by the statistical significance of the signal. Ways of distinguishing between different models involve the measurement of the natural width and the forward-backward asymmetry, both of which require sufficiently good momentum resolution at high p_T to determine correctly the sign of the leptons and a pseudorapidity coverage up to $\eta = 2.4$.

Chapter 2

The Compact Muon Solenoid experiment

The main goal of the LHC machine is the study of the electroweak symmetry breaking mechanism: two experiments have been built specifically in order to detect and discover every new physics process accessible at the LHC energies, the *A Toroidal LHC ApparatuS* (ATLAS) and the *Compact Muon Solenoid* (CMS) experiment. Their design differs significantly, since different solutions were chosen for the configuration of the magnetic field: ATLAS uses a toroidal field produced by three sets of air-core toroids complemented by a small inner solenoid, while CMS uses a solenoidal field generated by a big superconducting solenoid.
Both ATLAS and CMS are conceived as general purpose experiments which at the LHC energy allows for detecting and measuring the mass of new particles produced by collisions, up to the mass limit of $3 - 4\,\text{TeV}$.
The most important detector requirements for CMS to meet the goals of LHC physics program are [14]:

- good muon identification and momentum resolution over a wide range of momenta in the region $|\eta| < 2.5$ and capability to determine unambiguously the charge of muons with $p < 1\,\text{TeV}$;
- good dimuon mass resolution, $\sim 1\%$ at $100\,\text{GeV}$;
- good charged particle momentum resolution and reconstruction efficiency in the Tracker together with efficient triggering and offline tagging of τ's and b-jets;
- good electromagnetic energy resolution, good diphoton and dielectron mass resolution, measurement of the direction of photons and correct localization of the primary interaction vertex, π^0 rejection and efficient photon and lepton isolation at high luminosities;

- good missing energy and dijet mass resolution, using hadron calorimeters with a large hermetic geometric coverage ($|\eta| < 5$) and with fine lateral segmentation.

In order to fulfill this requirements CMS was built according to the layout shown in Figure 2.1 [15]. The final design of the detector allows a reliable identification and precise measurement of the muon momentum by means of a redundant muon identification system, a precise measurement of photons and electrons energy with a high resolution calorimeter system and an excellent reconstruction of the charged particle tracks and measurement of their momentum resolution thanks to a high quality inner tracking system. The detector structure consists of a cylindrical barrel closed by two endcap disks.

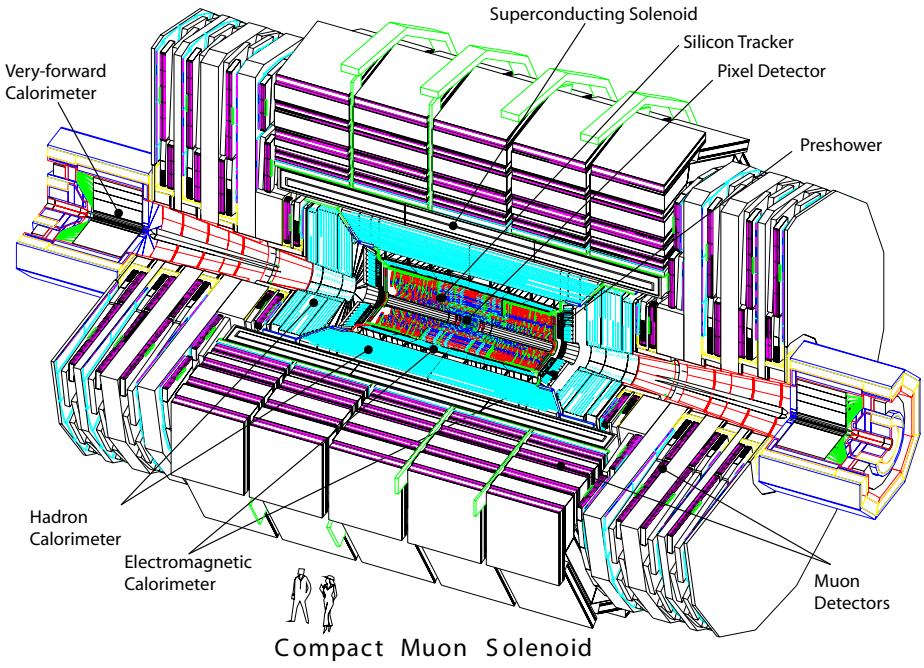

Figure 2.1: *View of CMS layout*

The overall length is 21.6 m, the diameter 14.6 m and the total weight about 12 500 tons. The thickness of the detector in radiation lengths is greater than 25 X_0 for the electromagnetic calorimeter, and the thickness in interaction lengths varies from 7 to 11 λ_I for the hadronic calorimeter, depending on the η region.

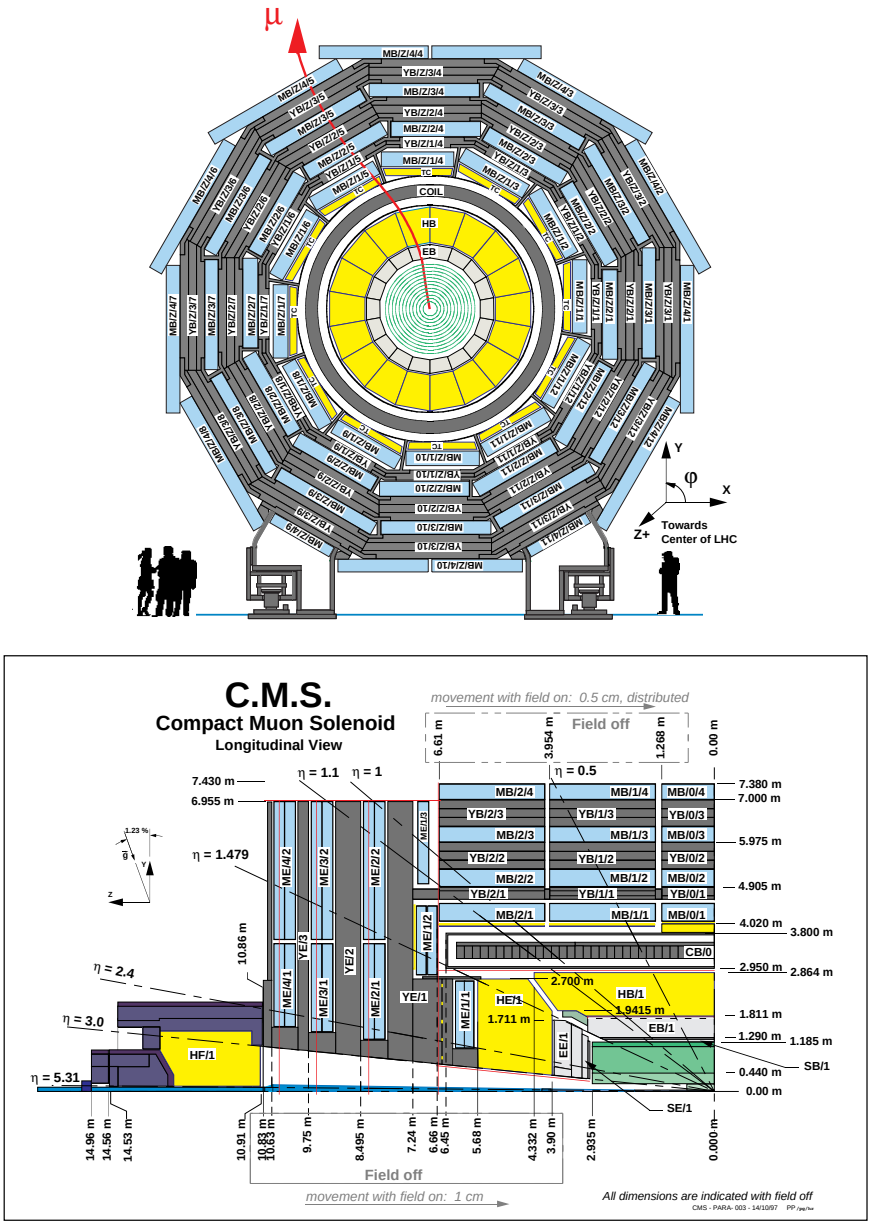

Figure 2.2: *Transverse view of the barrel region (top) and longitudinal view (bottom) of one quarter of the CMS detector [14].*

In addition to the right-handed coordinate system frame presented in Section 3.1, the CMS reconstruction use a system of spherical coordinates, based on the distance r from the z axis and azimuthal angle ϕ from with respect to the x axis.

For a particle carrying quadri-momentum $\mathbf{p} = (E, p_x, p_y, p_z)$, the rapidity is defined as:

$$y = \frac{1}{2} \ln \frac{E + p_z}{E - p_z} \tag{2.1}$$

where the variable y transforms as an additive quantity under longitudinal boost of the centre-of-mass. The rapidity is used for describing angular distribution of the events, being invariant under boost of the centre-of-mass along the z direction. For an ultra-relativistic particle ($p >> m$) y can be approximated to the pseudorapidity:

$$\eta = -\ln(\tan \theta/2) \tag{2.2}$$

were θ is the angle between the particle momentum p and the z axis.
The choice of a solenoidal magnetic field led to a very compact design for the CMS system, allowing calorimeters to be installed inside the magnet, with a strong improvement in the detection and energy measurement of electrons and photons. For a precise measurement of the momentum, it exploits both the constant field within the magnet and the field inside the return yoke. Moreover, tracks exiting the yoke point back to the interaction point, a property that can be used for track reconstruction. However the multiple scattering effect within the yoke degrades the resolution of the muon system. The longitudinal view of one quarter of CMS and the transverse view of the barrel region are shown in Figure 2.2.
The iron return yoke of the magnet (YB, YE) hosts the muon spectrometer, composed by 4 stations of drift tube detectors (DT) in the barrel region (MB) and 4 stations of cathode strip chambers (CSC) in the endcaps (ME). Both the barrel and the endcaps are equipped with resistive plate chambers (RPC), which ensure redundancy and robustness at the muon trigger system. The overall pseudorapidity coverage of the muon system goes up to $|\eta| < 2.4$. The core of the apparatus is the magnet (CB), a 13 m long super-conductive solenoid cooled with liquid helium, which can provide a 4 T magnetic field. The magnet coil has a diameter of 5.9 m and contains the hadronic and electromagnetic calorimeters and the Tracker.
The hadronic calorimeter (HCAL) is a brass/scintillator sampling calorimeter. The barrel and endcap parts (HB and HE) have the same pseudorapidity coverage as the electromagnetic calorimeter, and are complemented by a very forward calorimeter (HF), which extends the coverage up to $|\eta| < 5.3$. Inside HCAL, the electromagnetic calorimeter (ECAL) is installed: it is an homogeneous calorimeter made of lead tungstate scintillating crystals. The pseudorapidity coverage extends up to $|\eta| < 3.0$. In the endcaps a lead/silicon pre-shower detector is installed to improve the resolution on electron and photon direction and help pion rejection.
The tracking detector is placed in the core of CMS: its design was driven by the requirement of a precise vertex reconstruction and a reliable b-tagging

with very high track multiplicity. To achieve this goal very fine segmentation is crucial. The choice of CMS was to employ 10 layers of silicon microstrip detectors, which provide the required granularity and precision. In addition, 3 layers of silicon pixel detectors are placed close to the interaction region in order to improve the measurement of the impact parameter of charged particle tracks, as well as the position of primary and secondary vertices. The tracking device allows charged particle tracks reconstruction with at least 12 measurement points and a coverage of $|\eta| < 2.5$.

2.1 The inner tracking system

A highly performing tracking system is essential in order to fulfill the CMS physics goals. In a proton collider the longitudinal momentum is not exactly known event by event, and the measurement of the physics observables is performed in the transverse plane. Therefore, it becomes essential measuring the transverse momentum p_T with a very high resolution. The trajectory of a particle with transverse momentum p_T and charge ze inside a magnetic field B is an helix, with radius R. The relation among these quantities is:

$$p_T = 0.3 \cdot z \cdot B \cdot R$$

where p_T is expressed in GeV, B in T e R in m. What is experimentally measured is the radius R, or better, the curvature $k = 1/R$. The distribution of the measurements is gaussian, and the error can be written as the sum in quadrature of two contributions, the resolution on the measurement (δk_{res}) and the multiple Coulomb scattering (δk_{ms}):

$$\delta k = \sqrt{\delta k_{res}^2 + \delta k_{ms}^2}$$

Parametrizing the formula in terms of p_T, the particle transverse momentum resolution can be written as:

$$\frac{\delta p_T}{p_T} = C_1 \cdot p_T \oplus C_2$$

where the term C_2 contains the multiple Coulomb scattering effects, while the angular coefficient C_1 depends on the detector geometry, in particular from the number of point used for the track reconstruction (n), its length (L), and the resolution on the single point measurement (σ_x): $C_1 \propto \frac{\sigma_x}{\sqrt{n} \cdot B \cdot L^2}$ For low energetic particles C_2 is dominant. C_1 is minimized having a long tracker detector, and a consistent number of points n in the track fit. The resolution σ_x on the measured point is given by:

$$\sigma_x = \sqrt{\sigma_{int}^2 + \sigma_{syst}^2}$$

where σ_{int} is the intrinsic resolution of the detectors and σ_{syst} the systematic error given by the unknown spatial position of hit module: this last one can

be minimzed by alignment procedures. The major requirements for the CMS Tracker [16] can be summarized in the:

- promptness in the performance, given the high track population during the nominal LHC collisions of one event every 25 ns.
- robustness of its components to the radiation exposure, given the high density of hadronic tracks up to 10^{14} MeV n eq cm^2.
- minimization of the crossed material, with the aim of reducing the multiple Coulomb scattering of charged particles crossing the detector, photon conversion and electron energy loss via Bremsstrahlung.
- perfect alignment, internal of its components and with the muon system, in order to provide a reliable measurement of the particle momentum.

Therefore, the detector was designed in order to fulfill these requirements, giving at its nominal performance:

- reconstruction capability in the pseudorapidity region $|\eta| < 2.5$ with an efficiency of at least 95% for charged tracks having $p_T > 10\,\text{GeV}$.
- high momentum resolution for isolated tracks:

$$\frac{\delta p_T}{p_T} = (1.5 \cdot p_T \oplus 0.5)\% \quad \text{for } |\eta| < 1.6$$
$$\frac{\delta p_T}{p_T} = (6.0 \cdot p_T \oplus 0.5)\% \quad \text{for } |\eta| < 2.5$$

  were the p_T is expressed in TeV. Adding the information from the muon system, as shown in Figure 2.3, the resolution, for $p_T > 0.1\,\text{TeV}$ muons, becomes

$$\frac{\delta p_T}{p_T} \approx (4.5\% \cdot \sqrt{p_T})$$

- high resolution for transverse impact parameter, $\sigma(d_{xy}) = 35\,\mu$m and longitudinal impact parameter $\sigma(d_z) = 75\,\mu$m.

The CMS collaboration decided to build the whole detector using a silicon detector technology. This type of detector provides a high spatial resolution, from 10 to 20 μm and a fast collection of the charge deposited on the sensible elements, below 10 ns.
The Tracker covers the pseudorapidity region $|\eta| < 2.5$ with a radius ranging between 4.3 cm and 120 cm in the z interval between -270 and 270 cm. The innermost region is made of pixel detectors, while the outermost one is build with strip detectors.

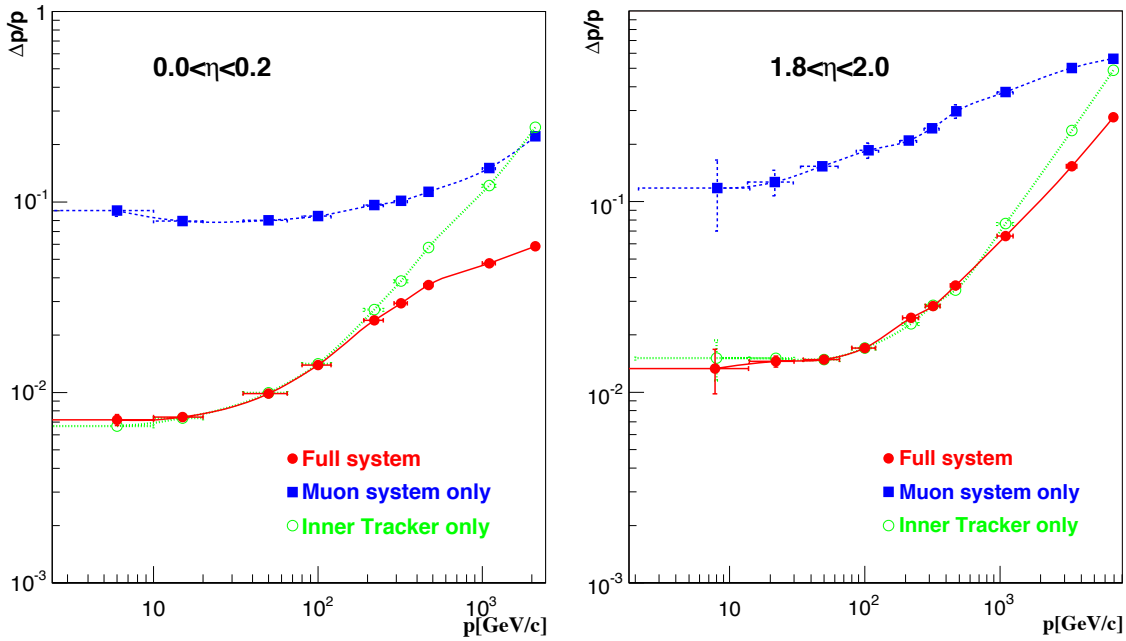

Figure 2.3: *Relative momentum resolution of muons as a function of momentum p, using mesurements of the muon system only (blue), the Tracker only (green) or both detectors (red). Left. Central region* $0 < \eta < 0.2$. *Rigth. Forward endcap region* $1.8 < \eta < 2.0$ *[14].*

2.1.1 The pixel Tracker

The pixel Tracker consists of three 53.3 cm long barrel layers and two endcap disks on each side of the barrel section, as shown in Figure 2.4. The innermost barrel layer has a radius of 4.4 cm, while for the second and third layer the radii are 7.3 cm and 10.2 cm, respectively. The layers are composed of modular detector units (called *modules*) placed on carbon fiber supports (called *ladders*). Each ladder includes eight modules, consisting of thin (285 μm), segmented silicon sensors with highly integrated readout chips (ROC) connected by Indium bump-bonds. Each ROC serves a 52×80 array of 150 μm × 100 μm pixels.
The barrel region is composed of 672 full modules and 96 half modules, each including 16 and 8 ROCs, respectively. The number of pixels per module is 66 560 (full modules) or 33 280 (half modules). The total number of pixels in the barrel section is 47 923 200.
The endcap disks, extending from 6 to 15 cm in radius, are placed at $z = \pm 35.5$ cm and $z = \pm 48.5$ cm. Disks are split into half-disks, each including 12 trapezoidal blades arranged in a turbine-like geometry.

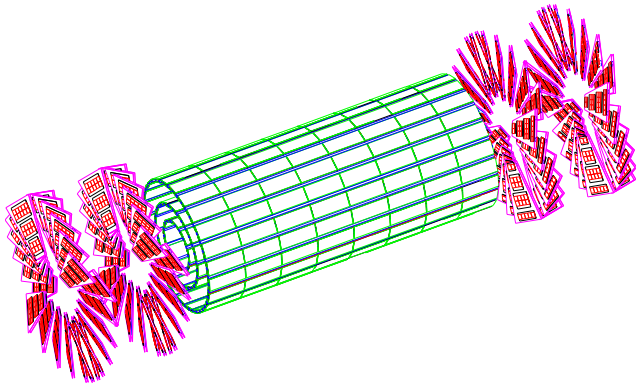

Figure 2.4: *Schematic illustration of the pixel Tracker.*

Each blade is a sandwich of two back-to-back panels. Rectangular sensors of five sizes are bump-bonded to arrays of ROCs, forming the so-called *plaquettes*. Three (four) plaquettes are arranged on the front (back) panels with overlap to provide full coverage for charged particles originating from the interaction point. The endcap disks include 672 plaquettes (270 μm thick), for a total of 17 971 200 pixels. The minimal pixel cell area is dictated by the readout circuit surface required for each pixel. In localizing secondary decay vertices both transverse ($r\phi$) and longitudinal (z) coordinates are important and a nearly square pixel shape is adopted. Since the deposited charge is often shared among several pixels, an analog charge readout is implemented. Charge sharing enables interpolation between pixels, which improves the spatial resolution. In the barrel section the charge sharing in the $r\phi$-direction is largely due to the Lorentz effect. In the endcap pixels the sharing is enhanced by arranging the blades in the turbine-like layout.

2.1.2 The strip Tracker

Outside the pixel detector, the Tracker is composed of 10 layers of silicon microstrip detectors (Figure 2.5).
The barrel region ($|\eta| < 1.6$) is divided into two parts: the Tracker Inner Barrel (TIB, covering $20 < r < 60$ cm) and the Tracker Outer Barrel (TOB, covering $60 < r < 120$ cm). The TIB is composed by four layers of n-type silicon sensors with a thickness of 320 μm and strip pitches varying from 80 to 120 μm . The first two layers are made with double sided (*stereo*) modules, composed by two detectors mounted back to back with the strips tilted by 100 mrad. This kind of sensors provides a measurement in both $r\phi$ and $r\,z$ coordinates with a single point resolution between $23 - 34\,\mu$m and 230 μm respectively.

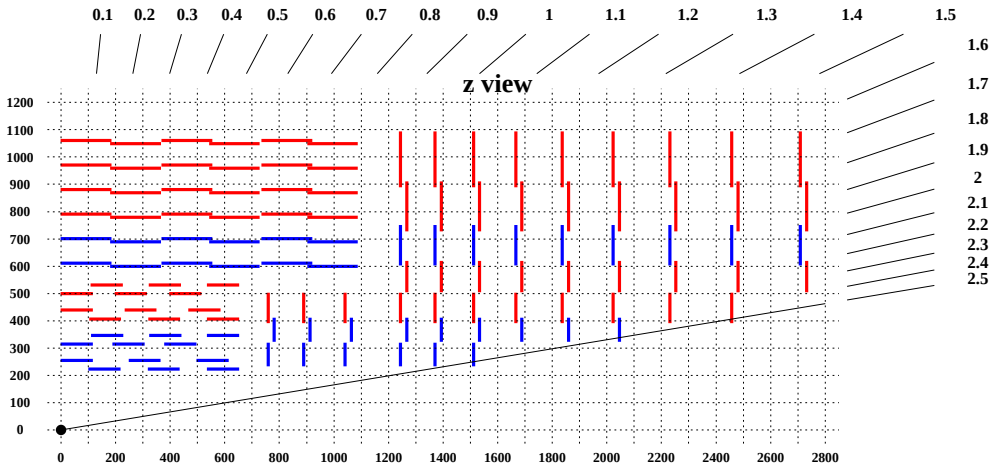

Figure 2.5: *Longitudinal view of one quarter of the strip Tracker: blue modules are double sided, red ones single sided.*

The TOB is made of six layers. In this region the radiation levels are smaller and thicker silicon sensors (500 μm) can be used to maintain a good signal-to-noise ratio for longer strip length and wider pitch. The strip pitch varies from 120 to 180 μm. Also the first two layers of the TOB provide a *stereo* measurement with a single point resolution which varies from 35 to 52 μm in the r direction and 530 μm in z.
The endcap region ($|\eta| > 1.6$) is covered by the Tracker Inner Disks (TID) and Tracker End Cap (TEC). The three disks of the TID fill the gap between the TIB and the TEC while the TEC comprises nine disks that extend into the region $120 < |z| < 280$ cm. Both subdetectors are composed of wedge shaped modules arranged in rings, centred on the beam line, and have strips that point towards the beam line.

2.1.3 Sensors working principle and signal readout

The basic working principle of the silicon Tracker sensors is the *pn* junction. The two semiconductor regions, one doped with atoms having 3 valence electrons (p-type) and the other doped with atoms having 5 valence electrons (n-type) are neutral if taken as single. If they become in contact, holes and electrons diffuse towards the junction, creating a depletion zone at the junction point: in this volume the electric field created offers resistance to

the free charge carriers migration. The depletion region can be increased applying a reverse bias voltage to the junction: the electron and hole pairs, created in the depletion region by the ionizing particle can now drift in the electric field and be collected by the relative substrate.
The pixel detectors (Figure 2.6, right) have an active surface of $6.4 \times 1.6\,\mathrm{cm}^2$ segmented in cells of $150 \times 100\,\mu m^2$. The active area is a $n^+ - n$ junction, with a p^+ implant in the ground layer for polarizing the junction. The implant has an area of $78 \times 78\,\mu\mathrm{m}^2$ surrounded by a p^+ guard ring: the nominal polarization voltage required to create the depletion region is 300 V, also imposed from the radiation dose, which acts inverting dopant concentration.
The strip detectors (Figure 2.6, left) have an active surface of $6 \times 12\,\mathrm{cm}^2$ in the TIB and $6 \times 18\,\mathrm{cm}^2$ in the TOB with a thickness of 320 (500) μm for the innermost (outermost) sensors. They are made of silicon n-type substrate, on which are implanted, at regular distance, strips of p-type silicon. There are 15 000 microstrip detectors, with a pitch between two neighbour strips ranging from 80 to 180 μm.

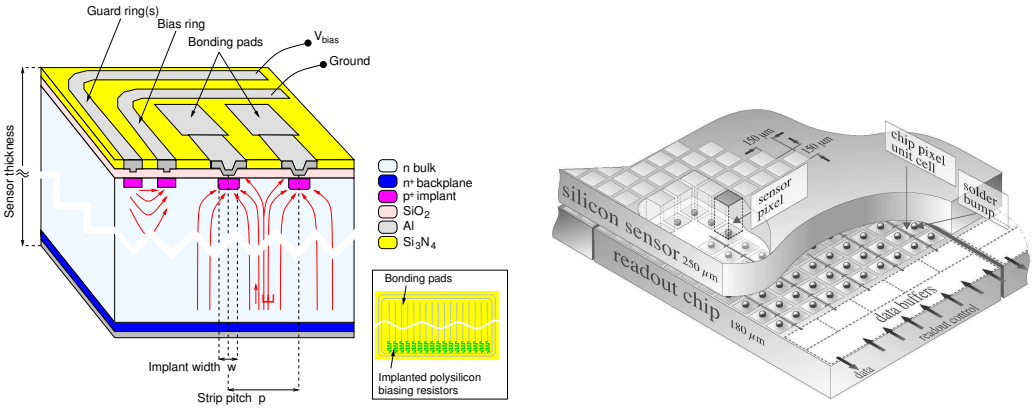

Figure 2.6: *Schematic view of a microstrip detector (left) and of a pixel detector (right) adopted in the CMS Tracker.*

In the pixel Tracker the readout chain starts in the pixel cell of the ROC, where the signals from individual pixels are amplified and shaped. To reduce the data rate, on-detector zero suppression is performed with adjustable thresholds for each pixel. Only pixels with charge above threshold are accepted by the ROC, marked with a time-stamp derived from the 40 MHz LHC bunch crossing clock, and stored on chip for the time of the trigger latency (about 3.7 μs) until readout.
In the strip Tracker the main components of the readout system are: 15 148 front-end detector modules that host about 76 000 APV25 readout chips [17],

an analogue optical link system comprising 38 000 individual fibres, and 440 off-detector analogue receiver boards, known as Front-End Drivers (FED). The control system is driven by 46 off-detector digital transceiver boards, known as Front-End Controllers (FEC). The FECs distribute the LHC clock, triggers and control signals to the front-end detector modules via Communication and Control Units (CCU), which are hosted on 368 control rings. The APV25 readout chip samples, amplifies, buffers, and processes signals from 128 detector channels at a frequency of 40 MHz. Fast pulse shaping is therefore required to provide bunch crossing identification and minimise event pileup. This is difficult to achieve with low noise and power levels, so the chip uses pre-amplifier and shaper stages to produce a CR-RC pulse shape with a relatively slow rise-time of 50 ns in an operating mode known as *peak*. An alternative mode, *deconvolution*, performs additional signal processing to constrain the signal to a single bunch crossing at the expense of a reduced signal-to-noise ratio. Deconvolution is expected to be the standard mode of operation during LHC collisions.

2.2 The calorimeters

2.2.1 The electromagnetic calorimeter

The goal of the electromagnetic calorimeter is the accurate measurement of the energy and position of electrons and photons. The physics process that imposes the strictest requirements on its performance is the low mass ($m_H \sim 120\,\text{GeV}$) Higgs decay into two photons, aiming 1% resolution on the $\gamma\gamma$ invariant mass. The natural choice to achieve this task is a homogeneous calorimeter.

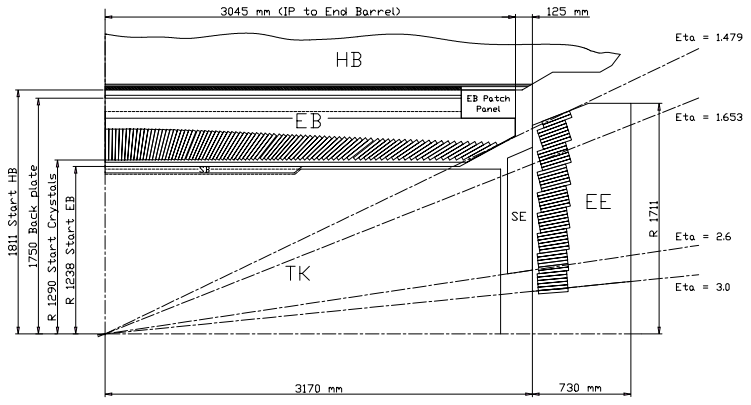

Figure 2.7: *Longitudinal view of one quarter of the CMS electromagnetic calorimeter [14].*

The ECAL is composed of 75848 finely segmented lead tungstate ($PbWO_4$) crystals. Lead tungstate is a fast, radiation-hard scintillator characterised by a small Moliere radius (21.9 mm) and a short radiation length (8.9 mm), that allows good shower containment in the limited space available for the detector. Moreover, these crystals are characterised by a very short scintillation-decay time that allows the electronics to collect about 80% of the light within 25 ns.
A pre-shower detector is installed in front of the endcaps, consisting of two lead radiators and two planes of silicon strip detectors, with a total radiation length of $3X_0$. It allows rejection of photon pairs from π^0 decays and improve the estimation of the direction of photons, to improve the measurement of the two-photon invariant mass.
The geometric coverage of the calorimeter extends up to $|\eta| = 3.0$, as shown in Figure 2.7. The crystals are arranged in a η-ϕ grid in the barrel and a x-y grid in the endcaps and they almost pointing to the interaction point: the axes are tilted at 3° in the barrel and at 2°-5° in the endcaps with respect to the line from the nominal vertex position.
The energy resolution of a calorimeter is usually parameterized as:

$$\left(\frac{\sigma}{E}\right)^2 = \left(\frac{a}{\sqrt{E}}\right)^2 + \left(\frac{b}{E}\right)^2 + c^2$$

where a is the stochastic term and it includes the effects of fluctuations in the number of photo-electrons as well as in the shower containment, b is the noise from the electronics and pile-up and c is a constant term related to the calibration of the calorimeter. The values of the three constants measured on test beams are reported in Table 2.1. The different contributions as a function of the energy are shown in Figure 2.8.

Contribution	Barrel ($\eta = 0$)	Endcap($\eta = 2$)
Stochastic term a	2.7%	5.7%
Noise (low luminosity) b	0.155 GeV	0.205 GeV
Noise (high luminosity) b	0.210 GeV	0.245 GeV
Constant term c	0.55%	0.55%

Table 2.1: *Different contributions to the energy resolution of ECAL [14].*

2.2.2 The hadron calorimeter

The goal of the hadron calorimeter is to measure the direction and energy of jets, the total transverse energy and the missing transverse energy of the

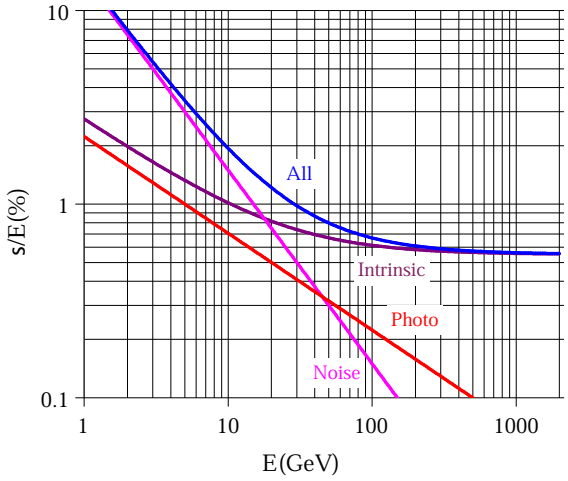

Figure 2.8: *Different contributions to the energy resolution of the ECAL. The curve labelled* intrinsic *includes the shower containment and a constant term [14].*

event. High hermeticity is required for this purpose. For this reason, the barrel and endcap parts installed inside the magnet are complemented by a very forward calorimeter which is placed outside the magnet return yokes, with a total coverage of $|\eta| < 5.3$.
The barrel and endcap HCAL cover the region $|\eta| < 3.0$. They are sampling calorimeters, whose active elements are plastic scintillators interleaved with brass absorber plates and read out by wavelength-shifting fibres. The first layer is read out separately, while all others are read out together. The absorber material has been chosen for its short interaction length, and its non-magnetic property. Both barrel and endcap are read-out in towers with a size of $\Delta\eta \times \Delta\phi = 0.087 \times 0.087$. In the barrel, full shower containment is not possible within the magnet volume, and an additional *tail catcher* is placed outside the magnet, consisting of an additional layer of scintillators. The projective depth in terms of nuclear absorption length goes from $5.1\,\lambda_0$ at $\eta = 0$ to $9.1\,\lambda_0$ at $\eta = 1.3$ and is $10.5\,\lambda_0$ in the endcap.
The very forward calorimeter is placed outside the magnet yoke, 11 m from the interaction point. The active elements are quartz fibres parallel to the beam, inserted in steel absorber plates. The signal originated from the quartz fibres is Cerenkov light.
The expected energy resolution is $\sigma/E \sim 65\%\sqrt{E} \oplus 5\%$ in the barrel, $\sigma/E \sim 85\%\sqrt{E} \oplus 5\%$ in the endcaps and $\sigma/E \sim 100\%\sqrt{E} \oplus 5\%$ (E in GeV) in the very forward calorimeter.

2.3 Muon identification system

Muons will provide a clear signature for many physics processes. For this reason, the muon spectrometer must provide a robust trigger and an accurate measurement of the muon momentum and charge, also without the contribution of the Tracker. The muon system, shown in Figure 2.9, is embedded in the iron return yoke of the magnet, which shields the detectors from charged particles other than muons. The minimum value of the muon transverse momentum required to reach the system is $\sim 5\,\text{GeV}$. The muon spectrometer consists of three independent subsystems.

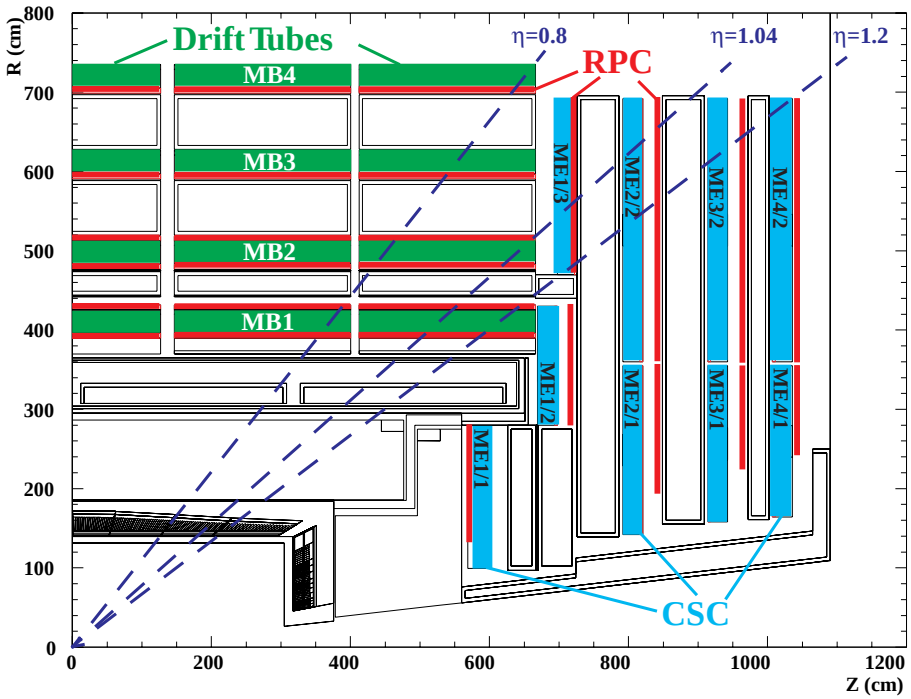

Figure 2.9: *Longitudinal view of one quarter of the CMS muon spectrometer [14].*

In the barrel ($|\eta| < 1.2$), where the track occupancy and the residual magnetic field are low, four layers (*stations*) of drift tube chambers (DT) are installed. The chamber segmentation follows that of the iron yoke, consisting in five wheels along the z axis, each one divided into 12 azimuthal sectors. Each chamber has a resolution of about $100\,\mu\text{m}$ in $r\phi$ and 1 mrad in ϕ.

In the endcaps ($0.8 < |\eta| < 2.4$), four disks (*stations*) of cathode strip chambers (CSC) are located, being this detector technology more indicated in a region suffering high particle rates and large residual magnetic field between the plates of the yoke. The innermost station consists of three concentric rings: the first one (ME1/1), being closer to the interaction point, is smaller than the other two. The other stations are composed by two rings only. The rings are formed by 18 or 36 trapezoidal chambers, which, with the exception of the outermost ring of ME1, are staggered with a small overlap in ϕ. These chambers have a spatial resolution of about 200 μm (100 μm for the chambers belonging to the first station) and 10 mrad in $r\phi$.
Redundancy is obtained with a system of resistive plate chambers (RPC), that are installed in both the barrel and the endcaps. RPCs have limited spatial resolution, but fast response and excellent time resolution of few ns, providing unambiguous bunch crossing identification. RPC detectors operate in *avalanche* mode rather than in the more common *streamer* mode, thus allowing the detectors to sustain higher rates. This mode is obtained with a lower electric field, thus the gas multiplication is reduced and an improved electronic amplification is required. In the barrel the RPC chambers follow the segmentation of DT chambers. A total of six layers of RPCs are present: the first four are attached to each side of the MB1 and MB2 DT chambers. The other two are attached to the inner surface of MB3 and MB4. In the endcaps the chambers are trapezoidal distributed on four disks. They are also used to complement DTs and CSCs in the measurement of the p_T. The RPC system covers the region $|\eta| < 2.1$.
The robustness of the spectrometer is also guaranteed by the different sensitivity of DT, RPC and CSC to the background. The main sources of background particles in the LHC environment will be represented by secondary muons produced in pion and kaon decays, from punch-through hadrons and from low energy electrons originating after slow neutron capture by nuclei with subsequent photon emission. This neutron induced background will be the responsible of the major contribution to the occupancy level in the muon detectors. CSC and DT chambers, in contrast with RPC detectors, are characterised by a layer layout which helps in reducing the effect of background hits: the request of correlation between consecutive layers is particularly effective against background hits affecting only a single layer.

2.4 The muon Trigger

The bunch crossing frequency at CMS interaction point is 40 MHz while technical difficulties in handling, storing and processing extremely large amounts of data impose a limit of about 100 Hz on the rate of events that can be written to permanent storage, as the average event size will be of about 1 MB. The goal of the trigger is to perform the required huge on-line

reduction of the data. The trigger must therefore be able to select events on the basis of their physics content, and online selection algorithms must have a level of sophistication comparable to that of offline reconstruction. The time available to accept or reject an event is extremely limited, being the bunch crossing time of 25 ns, a time interval too small even to read out all raw data from the detector. For this reason CMS adopts a multi-level trigger design, where each step of the selection uses only part of the available data. In this way higher trigger levels have to process fewer events and have more time available, so they can analyze the events in full details using more refined algorithms. The CMS trigger design is made of two physical steps, namely the Level-1 (L1) Trigger and the High Level Trigger (HLT).

Level-1 Trigger

The L1 Trigger is built of mostly custom-made hardware and it analyzes the detector information in a fairly coarse-grained scale. In the L1 step, the DT and CSC triggers determine the muon from the difference between segment slopes in successive layers of the muon spectrometer, whereas the RPC trigger compares the observed muon trajectory with predefined hit patterns as a function of p_T. All these triggers assume that muons are produced in a region around the LHC beam spot. The *Global Muon Trigger* system is responsible for matching DT and CSC candidates with RPC candidates, as well as for rejecting unconfirmed candidates of low quality. Up to four muon candidates satisfying some minimal quality criteria and with the highest p_T are forwarded to the HLT for further processing.

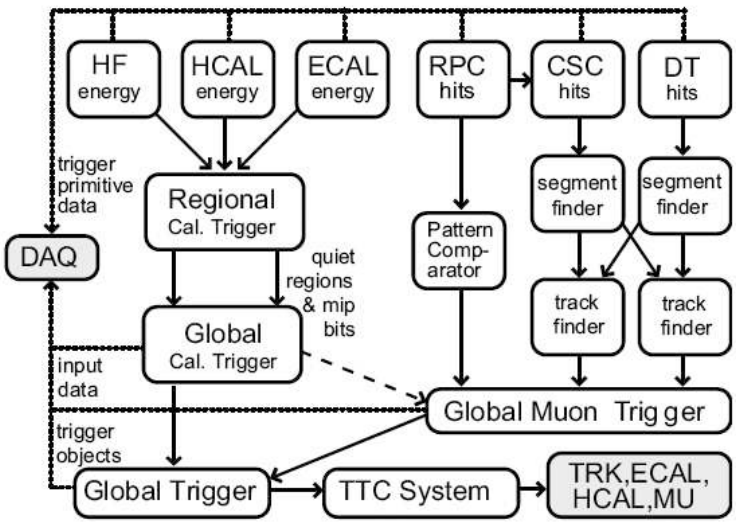

Figure 2.10: *Structure of the Level-1 Trigger system.*

High Level Trigger

The HLT system is software implemented in a single processor farm. In the first step of the HLT muon selection, referred to as Level-2 (L2), the L1 muon candidates are used to seed the reconstruction of tracks in the muon chambers. Unless for the seed, the L2 reconstruction follows the offline standalone reconstruction described in Section 2.5.1. A p_T threshold on the reconstructed L2 muon is applied and then the Level-3 (L3) reconstruction is carried out by combining L2 muons and charged-particle tracks reconstructed in the Tracker. Track parameters of the L2 muon, constrained to the interaction region, define a $\eta - \phi$ region where a seed for the L3 reconstruction is found. A relaxed beam-spot constraint is applied to track candidates above a given transverse momentum threshold to obtain initial trajectory parameters. Trajectories are then reconstructed using Kalman-filter techniques. Isolation criteria, based on the sum of transverse energies in the calorimeter towers (for L2 muons) and of transverse momenta of charged-particle tracks (for L3 muons) found in a cone around the direction of the muon ($\Delta R_{cone} = 0.24$), are finally applied.

2.5 Offline muon reconstruction in CMS

In a hadron collider leptons provide a clear signature for many of the most interesting physics processes, therefore a precise and fast reconstruction of the leptons is mandatory. In this context the muons play a key role as their parameters can be measured with great precision and, at least at high p_T, they can be identified unambiguously. The tracks within the muon system are built using the Kalman filter technique [18], combining the information coming from each muon sub-detector: this step is the so called *stand-alone* muon reconstruction. The following step is the propagation of the muon tracks to the Tracker, using some criteria to match the reconstructed Tracker track (*tracker* muon reconstruction). The information of the muon spectrometer and the Tracker system are combined in the *global* muon reconstruction, giving the final muon track. The reconstruction of the muons is completed by matching the muon track with the energy deposits in the calorimeters.

2.5.1 Track reconstruction in the muon spectrometer alone

The muon reconstruction chain starts with the *local* reconstruction in the muon spectrometer. First, hits in DTs, CSCs and RPCs are reconstructed from digitized electronics signals. Hits within each DT and CSC chamber are then matched to form a *segment* (track stub). The segments reconstructed

in the muon chambers are used to generate *seeds*, consisting of position and direction vectors and an estimate of the muon transverse momentum. The seed trajectory state parameters are propagated to the innermost compatible muon detector layer, by identifying for each point the detectors that most probably contain the next hit to be included in the trajectory (*navigation*). After this, a pre-filter is applied in the inside-out direction. Its main purpose is to refine the seed state before the true filter. The final filter in the outside-in direction is then applied and the trajectory is built
The pre-filter and filter are based on the same iterative algorithm: at each step the track parameters are propagated from one layer to the next. The best measurement is searched on a χ^2 basis. The χ^2 compatibility is examined at the segment level, estimating the incremental χ^2 given by the inclusion in the fit of the track segment. In case no matching hits (or segments) are found, the search continues in the next station (*pattern recognition* phase).
Once the hits are fitted and the fake trajectories removed, the remaining tracks are extrapolated to the point of closest approach to the beam line. In order to improve the p_T resolution a beam-spot constraint is applied. The result is a collection of *stand-alone* muons.

2.5.2 Track reconstruction in the Tracker alone

As in the muon system, the reconstruction process starts locally with the seed finding, but while in the muon system the trajectory is built during the pattern recognition, in the tracker the pattern recognition and the final fit are performed separately.
Three tracking algorithms have been developed: the first two designed for the reconstruction of proton-proton collisions (Combinatorial Kalman Filter, *CKF* and Road Search, *RS*) and one specialized algorithm for the reconstruction of single track cosmic events (Cosmic Track Finder, *CosTF*) [19]. In the following the two most used are examined.

Combinatorial Kalman Filter

The Combinatorial Kalman Filter (CKF) uses the capability of the Kalman Filter for simultaneous pattern recognition and track fitting. Starting from an initial estimate of the track parameters, the algorithm iterates through the layers of the tracker and builds a combinatorial tree of track candidates. The seeds are created in the innermost layers of the tracking system. A seed is made out of a hit pair and a loose beamspot constraint or out of a hit triplet. The starting parameters of the trajectory are calculated from a helix passing through the three points. The selected hits must be pointing towards the interaction point and a minimum transverse momentum cut is

applied. From each seed a propagation to the next surface is attempted. Hits are identified in a window whose width is related to the precision of the track parameters. If a hit is found within the window, it is added to the candidate trajectory and the track parameters are updated.
Candidates are sorted according to quality (based on the χ^2 and the number of hits) and the best ones are retained for further propagation.

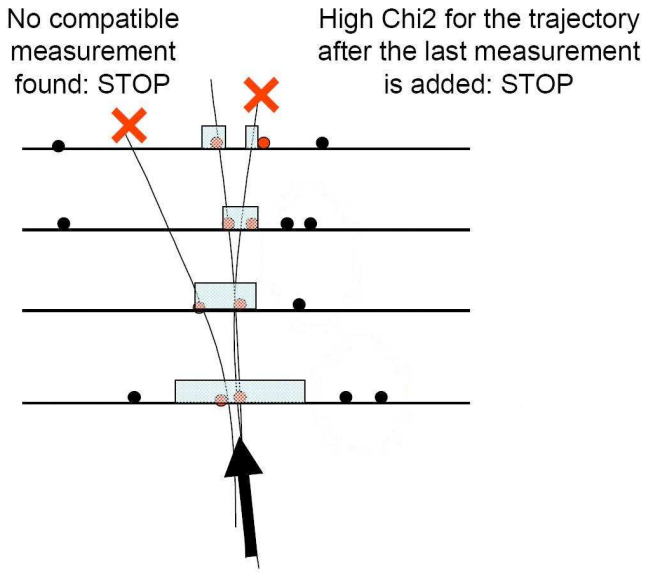

Figure 2.11: *Schematic representation of the Kalman Filter based pattern recognition. The points represent hits, the curved lines track candidates and the shaded boxes the size of the search window.*

Cosmic Track Finder

The Cosmic Track Finder is designed as a simple and robust algorithm, tailored to the specific task of reconstructing single tracks without imposing a region of origin, but assuming a preferred direction. All the hit pairs which are geometrically compatible are considered as potential seeds. During the pattern recognition, for each of the seed, preliminary track parameters are calculated based on the line connecting the two hits. The hit-selecting algorithm is simplified with respect to the CKF. A seed, which comes from the previous step, can be at the top or bottom of the instrumented region of the tracker. If it is at the top (bottom), all the hits with a y coordinate lower (higher) than the hit of the seed are sorted in decreasing (increasing) order with respect to the y axis.

The final fitting procedure is the same as for all the other CMS tracking algorithms and is based on the Kalman Filter approach. The result is a collection of *tracker* tracks.

2.5.3 Track matching: the global muon reconstruction

The track in the muon spectrometer is used to define a region of interest in the tracker. The determination of this region is based on the stand-alone muon with the assumption that the muon originates from the interaction point.
Inside the region of interest candidates for the muon trajectory (regional seeds) are built from pair or triplet of hits reconstructed on different tracker layers. It is possible to use all combinations of compatible pixel and double-sided silicon strip layers in order to achieve high efficiency. In addition, a relaxed beam-spot constraint is applied to track candidates above a given transverse momentum threshold to obtain initial trajectory parameters. Starting from the regional seeds, the standard tracker tracks are used to reconstruct tracks inside the selected region of interest.
The track matching is performed by propagating the muon and the tracker tracks onto the same plane and looking for the best χ^2 value from the comparison of track parameters. If there is a suitable match between tracker track and stand-alone muon track, then the hits from the tracker and the stand-alone muon track are combined in one collection and a final fit is performed over all hits, leading to the *global* muon. The reconstruction of the muons ends with the matching of the global muon track and the energy deposits in the calorimeters, the so called *calo* muon.

Chapter 3

The alignment of CMS Tracker

The *alignment* is the procedure of measuring the deviations of the position of sensitive elements in the real detector from their design value. A big challenge is to obtain alignment corrections to a precision that ensures that the track reconstruction performance is not compromised. Furthermore physics requirements like M_Z or M_W resolution place even more stringent constraints on the alignment precision.
To illustrate the principle behind the alignment, let assume to have an almost straight track, for example a energetic muon with $p > 40$ GeV, passing through a cylindrical detector made of several modules disposed on layer structures, able to provide high granularity and full angular coverage, embedded in a solenoid magnetic field.
In reality displacements of the modules with respect to their design positions are present due to the limited mounting precision or external mechanical effects. The real positions of the modules is not known a-priori and a design geometry is assumed by the track reconstruction algorithm, leading to a wrong determination of track parameters. For example the curvature and consequently the p_T estimate can be strongly biased due to an incorrect geometry assumption, as shown in the left picture of Figure 3.1. The goal of the alignment procedure is to provide the corrections to be applied to the positions of the modules in order to allow a reconstruction of the track as close as possible to the real one, as shown in the right picture of Figure 3.1. Alignment of large detectors in high energy physics often requires the determination of several thousands of alignment parameters, defining the spatial coordinates and orientation of the detector components. In the alignment process, hardware informations, like optical and laser measurements, in addition with the mounting precision informations, are usually combined together with data from particle interactions, like muons from resonance decays or cosmic rays, in order to reduce the module position uncertainty

to the micrometer level. But even if the χ^2 of the track fit is minimized and pattern recognition performs well, it is still possible to end up with biased measurements of track parameters due to remaining misalignment. Correlated displacements of the sensors which introduce a track parameter

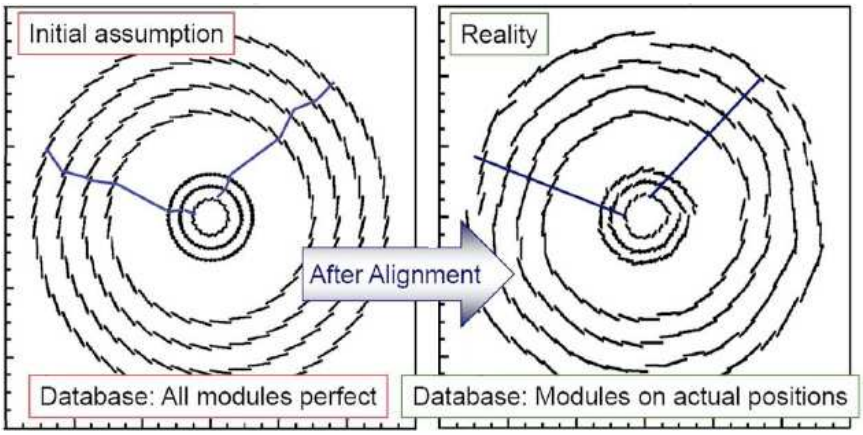

Figure 3.1: *Left picture: geometry in the detector is assumed to be ideal, even if misaligned in the reality, and this causes wrong estimation of particle's momentum. Right picture: module positions are moved according to the corrections found after the alignment procedure, leading to a geometry close to the real one and consequently a correct estimation of track parameters [20].*

bias can be χ^2 invariant, leading to certain coherent transformations of the geometry, the so-called "weak" modes. Therefore it is mandatory to choose a varied track topology, which allows to connect different parts of the detector and effectively reduce the displacements with respect to each other, and properly balance their weights when used in input to the algorithm minimization procedure.
The all-silicon design of the CMS Tracker poses new challenges in aligning a system with more than 15000 independent modules. Given the inaccessibility of the detector volume during collisions, the most accurate way to determine the silicon detector positions is to use the data from the silicon detectors themselves when they are traversed *in-situ* by charged particles. Additional information about the module positions is provided by the optical survey made during the construction phase and by the Laser Alignment System during the detector operation. Due to the complexity of the system, a hierarchical structure of the *alignable* objects and a coordinate system convention, has been defined.

3.1 Alignment hierarchy and coordinate system definition

Figure 3.2 shows a logical hierarchical representation of the CMS Tracker structures as implemented in the CMS software. Not all hierarchy levels shown are mechanically decoupled from its parent and therefore play a role as an independent object in the alignment procedure. For example, the *Layer* in the TOB is a logical structure that is extensively used in the tracking code, whereas it has reduced meaning as a separate alignment object since it is not a single mechanical structure. Therefore, the structure of the *alignables* differs from the logical view in some places. Each element of the hierarchy is free to be *moved* along all its six degrees of freedom and the movement of the parent structure is correctly propagated down to the daughters and vice versa. The lowest object in the hierarchy which can be aligned is the module unit.

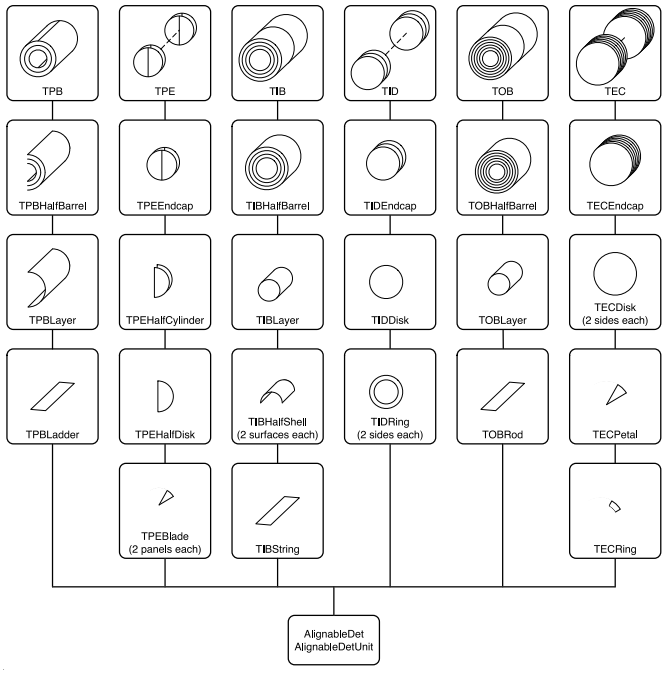

Figure 3.2: *Illustration of the hierarchies implemented inside the CMS alignment software. They closely follow the hierarchies of the mechanical structures.*

The *global* coordinate system in CMS is defined as follows. The origin is centered at the nominal collision point inside the experiment. The y-axis points upwards and the x-axis points inwards to the centre of the collider ring. Consequently the z-axis points along the beam axis. The azimuthal angle ϕ is measured from the x-axis in the x-y plane, while the polar angle θ is measured from the z-axis. In the CMS software the coordinate values are expressed in cm and rad.
The *local* coordinate system of an alignable, is defined instead with respect to the centre of its active area, as described in GEANT4. Modules in CMS are assumed to be rigid bodies and can be well described by the local coordinate system. Three positions and three rotations, as illustrated in Figure 3.3, specify their degrees of freedom. The local positions are called u, v and w, where u is along the sensitive coordinate (i.e. across the strips), v is perpendicular to u in the sensor plane and w is perpendicular to the uv-plane, completing the right-handed coordinate system. The rotations around the u, v and w axes are called α, β and γ, respectively. In the case of alignment of intermediate structures like rods, strings or petals, u and v are assumed to be respectively parallel and perpendicular to the precisely measured coordinate, while for the large structures like layers and disks, the local coordinates coincide with the global ones. In addition, local u' and

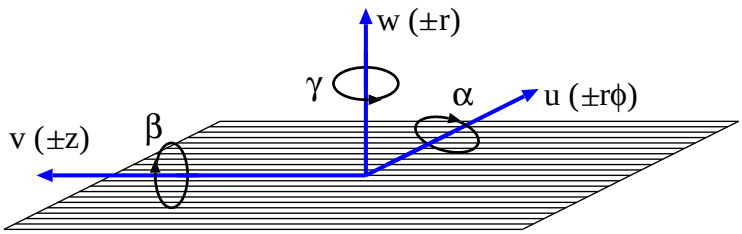

Figure 3.3: *Schematic illustration of the local coordinates of a module as used for alignment. Global parameters (in parentheses) are shown for modules in the barrel detectors (TIB and TOB).*

v' coordinates are defined such that they are parallel to u and v, but the direction is always chosen to be in positive ϕ, z, or r directions, irrespective of the orientation of the local coordinate system. For the TID and TEC wedge-shaped sensors, where the topology of the strips is radial, the u' and v'-axes change direction across the sensor such that v' is always directed along the strips and therefore u' corresponds to the global $r\phi$-coordinate.

3.2 The survey measurements

Information about the relative position of modules within detector components and of the larger-level structures within the Tracker is available from the optical survey analysis prior to or during the Tracker integration.
This includes Coordinate Measuring Machine (CMM) data and photogrammetry, the former usually used for the measurement of the position of active elements and the latter for the larger object measurements. For TIB, survey measurements are available for the module positions with respect to half shells, and of Layers with respect to the Tracker Support Tube. Similarly, for TID, survey measurements were done for modules with respect to the rings, rings with respect to the disks and disks with respect to the Tracker Support Tube. For TOB, the cylinders were measured with respect to the Tracker Support Tube. For TEC, measurements are stored at the level of disks with respect to the endcaps and endcaps with respect to the Tracker Support Tube. Figure 3.4 illustrates the relative positions of the CMS tracker modules with respect to the design geometry as measured in optical survey: as can be seen, differences from the design geometry as large as several millimeters are present. Since hierarchical survey measurements were performed and TOB and TEC have only large-structure information, the corresponding modules appear to be coherently displaced in the plot. An overview of the mounting precision of the strip Tracker elements is given in Table 3.1.

TIB		TID		TOB		TEC	
Sensor		Sensor		Sensor		Sensor	
	10		10		10		10
Module		Module		Module		Module	
	180		54		30		20
Shell		Ring		Rod		Petal	
	450		185		100		70
Cylinder		Disc		Wheel		Disc	
	750		350		140 ($r\phi$), 500(z)		150
Tube		Cylinder		Tube		TEC	
			450		1000		600
		Tube		CMS		Tube	

Table 3.1: *Estimated assembly precision (RMS, in μm) of tracker components. Values are given in between the mechanical hierarchy levels they are valid for, e.g. the position accuracy of sensors in modules is* $10\,\mu$m

Concerning the pixel detectors, detailed optical surveys of both barrel and endcaps were performed as part of the construction process. In the endcap region, first module positions were measured within a panel, which contains

three or four modules. Then the position of modules were measured on a half-disk, where 12 panels are placed on each side. Finally, half-disks were placed in the half cylinders, which were then inserted in the pixel detector volume. Half-disk and half cylinder positions were measured, with photogrammetry and were related to the active element position through photo targets, which had been previously measured with CMMs. In the barrel pixel detector, only two-dimensional measurements of the module positions within a ladder were performed.

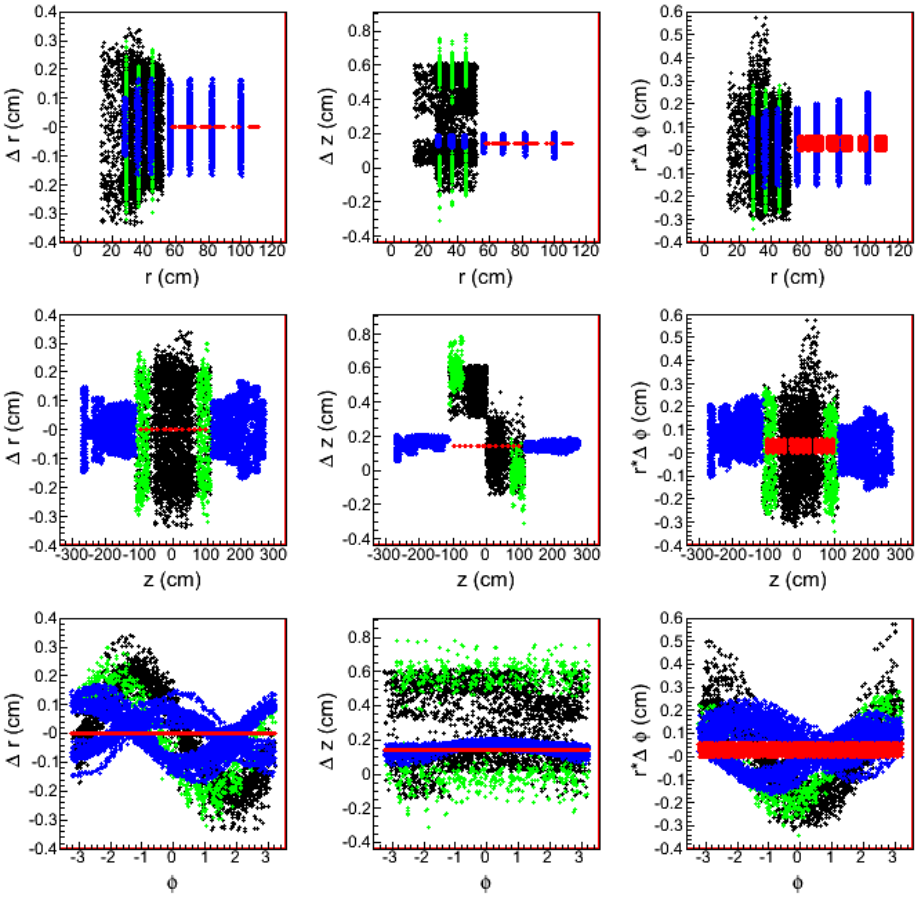

Figure 3.4: *Displacement of modules in CMS global cylindrical coordinates as measured in survey with respect to design geometry. A colour code is used: black for TIB, green for TID, red for TOB, and blue for TEC [29].*

3.3 Monitoring of the geometry using Laser system

The Laser Alignment System (LAS, see Figure 3.5) [15] uses infrared laser beams with a wavelength of $\lambda = 1075\,\text{nm}$ to monitor the possible movements of Tracker structures. It operates globally on Tracker substructures (TIB, TOB and TEC disks) and cannot determine the position of individual modules. The goal of the system is to provide continuously information that can be used for alignment, providing geometry information on the position of the Tracker substructures at the level of $100\,\mu\text{m}$. In addition, possible movements of Tracker structure can be monitored at the level of 10 μm, providing additional input for the track based alignment.
In each TEC, laser beams cross all nine TEC disks in ring 6 and ring 4 on the back petals, equally distributed in ϕ. Here, special silicon sensors with a 10 mm hole in the backside metallisation and covered by an anti-reflective coating are mounted. The beams are used for the internal alignment of the TEC disks. The other eight beams, distributed in ϕ, are foreseen to align TIB, TOB, and both TECs with respect to each other. Finally, there is a link to the muon system, which is established by 12 laser beams (six on each side) with precise position and orientation in the Tracker coordinate system. The connection with the muon system is established by Alignment Rings, which are connected with the back part of TEC disks.

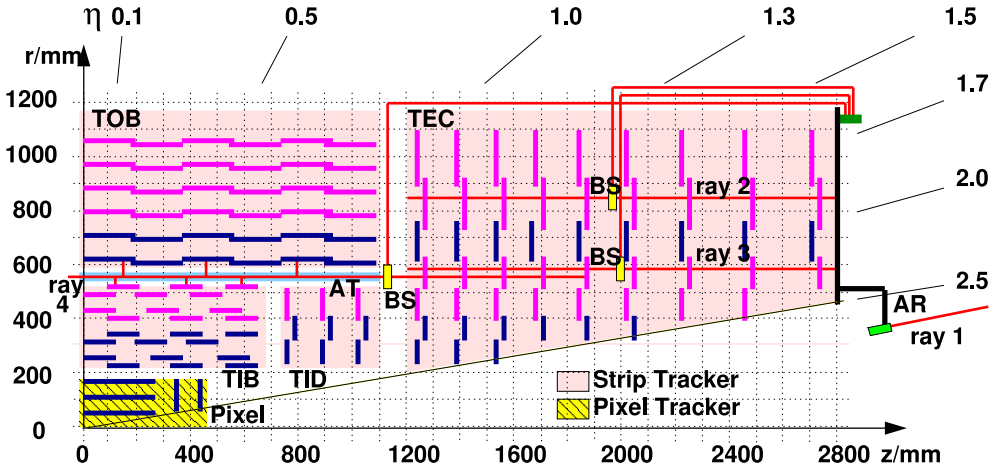

Figure 3.5: *Overview of the CMS Laser Alignment System. Alignment Tubes (AT), ranging from endcap to endcap, together with Alignment Ring (AR) for the Endcap monitoring, distribute the light via optical fibers through the Beam Splitter (BS).*

The signal induced by the laser beams on the silicon sensors decreases in height as the beams penetrate through subsequent silicon layers in the TEC and through beam splitters in the alignment tubes that partly deflect the

beams onto TIB and TOB sensors. To obtain optimal signals on all sensors, a sequence of laser pulses with increasing intensities, optimised for each position, is generated. Several triggers per each intensity step are taken, and the signals are averaged. In total, a few hundred triggers are needed to get a full picture of the alignment of the Tracker structure. Since the trigger rate for the alignment system is around 100 Hz, this takes only a few seconds.

3.4 The track based alignment

The goal of the track based alignment procedures is to determine the module positions from a large sample of reconstructed charged particle trajectories. The alignment using tracks is what allows to reduce the module position uncertainty to the level of few microns.
During nominal LHC operations the ideal datasets for alignment are tracks from $W^{\pm} \to \mu^{\pm}\nu$ and $Z \to \mu^{+}\mu^{-}$. Furthermore the Z mass constraint can be exploited not only to correlate the detector parts that are not crossed by a single collision track, e.g. the two endcaps, but also to tightly constrain the momentum scale of muon tracks. The invariant mass constraint could also be applied to any quarkonia resonance, like $J/\psi \to \mu^{+}\mu^{-}$ process, but in this case the muons have low momentum, and this requires, due to multiple scattering effects, a special selection in order to exploit them as input for alignment. Apart from isolated muon tracks, it is foreseen to use well-measured tracks from minimum bias events, especially during first data-taking period when the machine luminosity is expected to be very low, as this might be the only source of tracks for alignment. Finally, muons from cosmic rays represent a valuable input for alignment, especially during the commissioning phase, and the strategy and the level of precision that can be obtained from this topology of track will be widely studied in the Chapter 4. Moreover all beam halo muons and cosmic ray tracks collected during collisions can become useful in the reduction of weak modes.

Track based alignment is based on a simple principle: minimization of track residual. Assuming a perfectly aligned detector, each trajectory is built from charge deposits on individual detectors, the *hit*, and assuming a helical track model which incorporates effects from multiple scattering and energy loss. Five track parameters describe the helical trajectory of a track at the point closest to the nominal interaction point: distance of closest approach in the transverse d_{xy} and longitudinal d_z directions, track azimuthal angle ϕ, track polar angle θ and q/p_T. Recorded measurements $\mathbf{m_{ij}}$ of the i-hit can be compared to the prediction, denoted with $\mathbf{f_{ij}}$, of the point where the j-track crosses the module, according the track model. The difference, expressed in local coordinates, between these two quantities are the track-hit residuals $\mathbf{r}_{ij}$, which are 1 or 2-dimensional vectors according to the kind

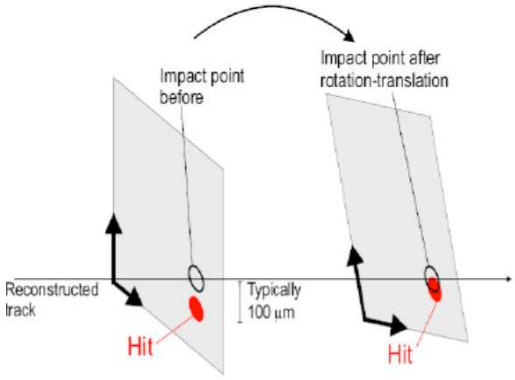

Figure 3.6: *Track impact point and hit position on module surface before and after alignment*

of module (e.g. pixel modules are bi-dimensional). The predicted impact point measurement $\mathbf{f_{ij}}(\mathbf{p}, \mathbf{q_j})$ of the j-track depends on the track parameter $\mathbf{q_j}$ and module position corrections or alignment parameters $\mathbf{p}$. Ideally all measured points of this trajectory have normal distributed residuals within a width of the nominal detector resolution. Therefore the normalized residual $\mathbf{s_{ij}}$ between the predicted hit position and the recorded measurement of i-hit can be written as:

$$\mathbf{s_{ij}} = \frac{\mathbf{r_{ij}}}{\sigma_\mathbf{i}} = \frac{\mathbf{m_{ij}} - \mathbf{f_{ij}}(\mathbf{p}, \mathbf{q_j})}{\sigma_\mathbf{i}} \tag{3.1}$$

where $\sigma_\mathbf{i}$ are the uncertainty of the mesurements. Since a real detector has a finite resolution defined by properties of the sensing device itself and by physical effects, like multiple scattering of particles crossing the matter, the values of $\sigma_\mathbf{i}$ are non-zero and therefore calculable.
In the reality the detector is misaligned: the measured point along a trajectory differs by how much the position of the module is shifted away from its ideal position. The residual will be higher than in the ideal case, while detector resolution does not change. The basic idea is to re-adjust the positions of all the modules, by minimizing the sum of the normalized residuals of Equation 3.1. This sum is called *objective* function:

$$\sum_{j}^{\text{tracks}} \sum_{i}^{\text{hits}} \mathbf{s_{ij}^2}(\mathbf{p}, \mathbf{q_j}) = \sum_{j}^{\text{tracks}} \sum_{i}^{\text{hits}} \frac{(\mathbf{m_{ij}} - \mathbf{f_{ij}}(\mathbf{p}, \mathbf{q}_j))^2}{{\sigma_\mathbf{ij}}^2} = \chi^2(\mathbf{p}, \mathbf{q}) \tag{3.2}$$

and is expressed as the sum over all hits i on all tracks j and track parameters $\mathbf{q}_j$, assuming negligible correlations between hits. As this sum is weighted by the errors, it assumes the properties of a χ^2 variable, under the assumption that residuals are gaussian distributed.

3.5 Alignment algorithms

Three different approaches are implemented in CMS software to solve the minimization problem of Equation 3.2. All of them were tested and widely employed for the Tracker alignment during the stand-alone commissioning at the Integration Facility described in Section 3.7. Since angular corrections are small, the linearization in the alignment parameters ($\delta\mathbf{p} = \mathbf{p} - \mathbf{p_0}$) of the Equation 3.2 is a good approximation and will be used by algorithms as a starting approach for solving large system of equations.

3.5.1 The Millepede algorithm

The algorithm and its features are described in detail in [21]. Its principle is a global fit to minimise the χ^2 function, simultaneously taking into account track $\mathbf{q}$, and alignment $\mathbf{p}$, parameters [1]. Given reasonable starting values $\mathbf{p}_0$ and $\mathbf{q}_{j0}$, the track model prediction $\mathbf{f_{ij}}(\mathbf{p}, \mathbf{q}_j)$ in Equation 3.2 can be written, with the linear approximation, as:

$$\chi^2(\mathbf{p},\mathbf{q}) = \sum_{j}^{\text{tracks}} \sum_{i}^{\text{hits}} \frac{1}{\sigma^{\mathbf{2}}_{\mathbf{ij}}} (\mathbf{m_{ij}} - \mathbf{f_{ij}}(\mathbf{p_0}, \mathbf{q}_{j\,0}) + \frac{\partial \mathbf{f}}{\partial \mathbf{p}} \delta\mathbf{p} + \frac{\partial \mathbf{f}}{\partial \mathbf{q_j}} \delta\mathbf{q_j})^{\mathbf{2}} \qquad (3.3)$$

Applying the least squares method to minimize the χ^2 results in a large linear system with one equation for each alignment parameter and all the track parameters of each track. After having defined:

$$(\Gamma_j)_{kl} = \sum_i \left(\frac{\partial \mathbf{f_{ij}}}{\partial \mathbf{q_{jk}}}\right)\left(\frac{\partial \mathbf{f_{ij}}}{\partial \mathbf{q_{jl}}}\right)\frac{1}{\sigma^2_{ij}} \qquad (G_j)_{kl} = \sum_i \left(\frac{\partial \mathbf{f_{ij}}}{\partial \mathbf{q_{jl}}}\right)\left(\frac{\partial \mathbf{f_{ij}}}{\partial \mathbf{p_{jk}}}\right)\frac{1}{\sigma^2_{ij}}$$

$$(C_j)_{kl} = \sum_i \left(\frac{\partial \mathbf{f_{ij}}}{\partial \mathbf{p_{jk}}}\right)\left(\frac{\partial \mathbf{f_{ij}}}{\partial \mathbf{p_{jl}}}\right)\frac{1}{\sigma^2_{ij}} \qquad (\beta_j)_k = \sum_i \left(\frac{\partial \mathbf{f_{ij}}}{\partial \mathbf{q_{jk}}}\right)\frac{\mathbf{s_{ij}}}{\sigma^2_{ij}}$$

$$(b_j)_k = \sum_i \left(\frac{\partial \mathbf{f_{ij}}}{\partial \mathbf{p_{jk}}}\right)\frac{\mathbf{s_{ij}}}{\sigma^2_{ij}}$$

the matrix structure solving the system of Equation 3.3 appears the following:

$$\begin{pmatrix} \sum \mathbf{C_j} & \cdots & \mathbf{G_j} & \cdots \\ \vdots & \ddots & 0 & 0 \\ \mathbf{G_j^T} & 0 & \mathbf{\Gamma_j} & 0 \\ \vdots & 0 & 0 & \ddots \end{pmatrix} \cdot \begin{pmatrix} \delta\mathbf{p} \\ \vdots \\ \delta q_j \\ \vdots \end{pmatrix} = \begin{pmatrix} \sum \mathbf{b_j} \\ \vdots \\ \beta_j \\ \vdots \end{pmatrix} \qquad (3.4)$$

The sub-matrices $\mathbf{\Gamma_j}$ include only derivatives with respect to $\mathbf{q}$ parameters. The matrices $\mathbf{G_j}$ include derivatives with respect to both $\mathbf{p}$ and $\mathbf{q}$

[1] In the Millepede language these are called *local* ($\mathbf{q}$) and *global* ($\mathbf{p}$) parameters

parameters. Only derivatives with respect to **p** parameters are found in the matrices $\mathbf{C_j}$. Matrix **b** includes products of global derivatives and the normalized residuals. The particular structure of the system of equations allows a reduction of its size, leading to the matrix equation:

$$\mathbf{C}'\,\delta\mathbf{p} = \mathbf{b}' \tag{3.5}$$

after defining $\mathbf{C}'$ and $\mathbf{b}'$ as follows:

$$\mathbf{C}' = \sum_i \mathbf{C_i'} - \sum_i \mathbf{G_i}\mathbf{\Gamma_i^{-1}}\mathbf{G_i^T} \qquad \mathbf{b}' = \sum_i \mathbf{b_i'} - \sum_i \mathbf{G_i}(\mathbf{\Gamma_i^{-1}}\beta_\mathbf{i}) \tag{3.6}$$

Being interested only in the n alignment parameters, the problem is reduced to the solution of a matrix equation of size n in order to extract the vector elements δp without loss of information. Depending on the size and the sparseness of the matrix, there are several methods implemented in Millepede for solving Equation 3.5:

- *Inversion.* The CPU time needed for inverting a $n \times n$ matrix scales with n^3 and the memory needed to store the matrix with n^2. Therefore is not applicable in case of very large systems.

- *Diagonalization.* The computing requirements even exceed the inversion method. However the eigenvectors and eigenvalues which are determined can be physically interpreted and used for diagnostic of alignment problem.

- *Variable Band Cholesky.* This method can be used to solve a system of linear equations which can be represented by a symmetric matrix. Only the matrix elements within the band need to be stored. However, the matrix which is built in the course of the χ^2 minimization is not a band matrix. The solution obtained via the band Cholesky method ignores some correlations and is therfore only an approximate solution, hence iterations are required.

- *GMRES.* If the matrix $\mathbf{C}'$ is sparse (contains many zero elements) the memory demand can be reduced by storing only non-zero elements. It is a more generically applicable version of the MINRES algorithm [22], which can only be applied to positive definite matrices. The speed of convergence and precision can be improved if the matrix equation is multiplied by an approximated solution of the inverse of the matrix, called preconditioning.

In addition, rejection and down-weighting of other hits as well as constraints to fix the global degrees of freedom turn out to be important.
Furthermore, the Millepede algorithm foresees the possibility to assign χ^2 penalties, the so called *presigma*s, which are initial uncertainties σ_p given

to individual alignment parameters. For each alignment parameter, $1/\sigma_p$ is added to the diagonal matrix entry of the parameter. The χ^2 penalties are defined with respect to the alignment parameters of the previous iteration within Millepede. This means that alignment corrections that are significantly larger than the corresponding presigma are allowed after several iterations. Iterations are needed for outlier rejection in any case. Assigning presigmas does improve the stability of the solution of the matrix equation, thereby avoiding numerical problems.

The software version of `Millepede II` [23] is an upgraded version of the `Millepede` program, written in FORTRAN language. The implementation of the algorithm consits of two parts: `Mille` is a data collecting subroutine which prepares the data files for the second part, `Pede`. In particular data on the measurements of the track model predictions and on derivatives with respect to track and alignment parameters are written to binary files which are the input to `Pede`. This part of the program performs the calculation and dumps the values of parameters $\delta\mathbf{p}$ found into text and sqlite files, via an interface with CMS software.
Millepede was successfully used in the first full CMS Tracker alignment study on simulated data [24]. The algorithm will be denoted in the following as *global* method, to characterize its mathematical approach to the alignment problem solution.

3.5.2 The Hit and Impact Point algorithm

The HIP (Hits and Impact Points) algorithm is described in detail in [25]. Neglecting the track parameters in Equation 3.2, the alignment parameters $\mathbf{p_m}$ of each module can be found independently from each other. The general formalism of the χ^2 minimisation in the linear approximation leads to:

$$\mathbf{p}_m = \left[\sum_i^{\text{hits}} \mathbf{J}_i^T \mathbf{V}_i^{-1} \mathbf{J}_i\right]^{-1} \left[\sum_i^{\text{hits}} \mathbf{J}_i^T \mathbf{V}_i^{-1} \mathbf{r}_i\right] \tag{3.7}$$

where the Jacobian $\mathbf{J}_i$ is defined as the derivative of the residual with respect to the sensor position parameters and can be found analytically in the small angle approximation, used by the other algorithms as well. Correlations between different modules and effects on the track parameters are accounted for by iterating the minimisation process and by refitting the tracks with new alignment constants after each iteration.
The HIP algorithm permits also the inclusion of the survey measurements in the formalism of Equation 3.2, as described in [26]. This leads to an additional term in the objective function to be minimized independently for

each module m in a given iteration:

$$\chi^2_m(\mathbf{p}) = \sum_i^{\text{hits}} \mathbf{r}_i^T(\mathbf{p})\mathbf{V}_i^{-1}\mathbf{r}_i(\mathbf{p}) + \sum_j^{\text{survey}} \mathbf{r}_{*j}^T(\mathbf{p})\mathbf{V}_{*j}^{-1}\mathbf{r}_{*j}(\mathbf{p})\,, \tag{3.8}$$

This allows to include survey information from the hierarchial levels for each sub-detector. In the HIP approach the track residuals $\mathbf{r}_i(\mathbf{p})$ do not have explicit dependence on track parameters and enter the sum over hits in a given module m. The six-dimensional survey residuals $\mathbf{r}_{*j}$ are defined as the difference between the reference and the current sensor position. The survey measurement covariance matrix $\mathbf{V}_{*j}$ reflects both the survey precision and additional uncertainties due to changes in the detector. These errors can be configured differently for different hierarchy levels and for the degrees of freedom that should be stable, such as the longitudinal direction in a barrel ladder, and those which may change more frequently. The HIP algorithm will be denoted in the following as *local* method.

3.5.3 The Kalman Filter algorithm

The Kalman alignment algorithm [27] is a sequential method, derived using the Kalman filter formalism. It is sequential in the sense that the alignment parameters are updated after each processed track. The algorithm is based on the track model $\mathbf{m} = \mathbf{f}(\mathbf{q_t}, \mathbf{p_t}) + \epsilon$. This model relates the observations $\mathbf{m}$ to the true track parameters $\mathbf{q_t}$ and the true alignment constants $\mathbf{p_t}$ via the deterministic function $\mathbf{f}$. Energy loss is considered to be deterministic and is dealt with in the track model. The stochastic vector ϵ as well as its variance-covariance matrix $\mathbf{V}$ contain the effects of the observation error and of multiple scattering. Therefore the matrix $\mathbf{V}$ contains correlations between hits such that Equation 3.2 is a sum over tracks, with residuals being of higher dimension according to the number of hits along the track trajectory. Linearised around an expansion point $(\mathbf{q_0}, \mathbf{p_0})$, the track model reads:

$$\mathbf{m} = \mathbf{c} + \mathbf{D_q}\mathbf{q_t} + \mathbf{D_p}\mathbf{p_t} + \epsilon,$$
$$\mathbf{D_q} = \partial\mathbf{f}/\partial\mathbf{q_t}|_{\mathbf{q_0}}, \mathbf{D_p} = \partial\mathbf{f}/\partial\mathbf{p_t}|_{\mathbf{p_0}}, \mathbf{c} = \mathbf{f}(\mathbf{q_0}, \mathbf{p_0}) - \mathbf{D_q}\mathbf{q_0} - \mathbf{D_p}\mathbf{p_0}$$

By applying the Kalman filter formalism to this relation, updated equations for the alignment parameters $\mathbf{p}$ and their variance-covariance matrix $\mathbf{C}_p$ can be extracted. The Kalman filter algorithm will be denoted in the following as *sequential* method.

3.6 The CMS alignment workflow

The CMS alignment workflow has to ensure that the prompt event reconstruction can apply alignment constants that are already updated for possi-

ble rapidly changing data taking conditions. Figure 3.7 shows the alignment data flow from its origin (CMS pit) to its end (final reconstruction at Tier-0). Part of the data recorded by CMS and selected by the High Level Trigger described in Section 2.4 are used for alignment purposes. This includes data from special calibration and alignment runs as it is the case for the Laser Alignment System, and collision events that are of interest both for alignment and physics analysis. These events are reconstructed with low latency at the CMS Tier-0, and this step is called *express* reconstruction.
A special reduced event format denoted as *AlCaReco* is written to the CMS Analysis Facility (CAF), while all physics events are being stored in a large buffer for 24 hours. This format contains only the skimmed type of collections needed for alignment and calibration processes. In addition some quality cuts to the track collection are included, in order to select, already at this level, good quality input for the alignment algorithms. Examples of these cuts for three different streams, cosmics, minimum bias and $Z \rightarrow \mu\mu$ events, is given in the Table 3.2. At the CAF, the reduced event data are

stream	η	p **or** p_T (GeV)	**nr. hits**	**others**
ALCARECOTkAlCosmics0T	$[-99; 99]$	no cut	≥ 7	# hit2D ≥ 2
ALCARECOTkAlMinBias	$[-3.5; 3.5]$	$p \geq 1.5$	≥ 5	none
ALCARECOTkAlZMuMu	$[-3.5; 3.5]$	$p_T \geq 15$	no cut	$70 < M_Z < 110$ GeV && μ iso

Table 3.2: *Main cuts applied for the different selection of AlCaReco streams of data*

input to the alignment procedure (LAS and track based alignment). Alignment parameters are determined, validated and uploaded to the database (ORCON and ORCOFF). The alignment procedure needs to be ready before 24 hours have passed, in order to be used for the *prompt* reconstruction and production of the RECO or AOD format of all physics events. A succesful test of this workflow has been performed during the CMS Software and Analysis Challenge in 2008 [28].

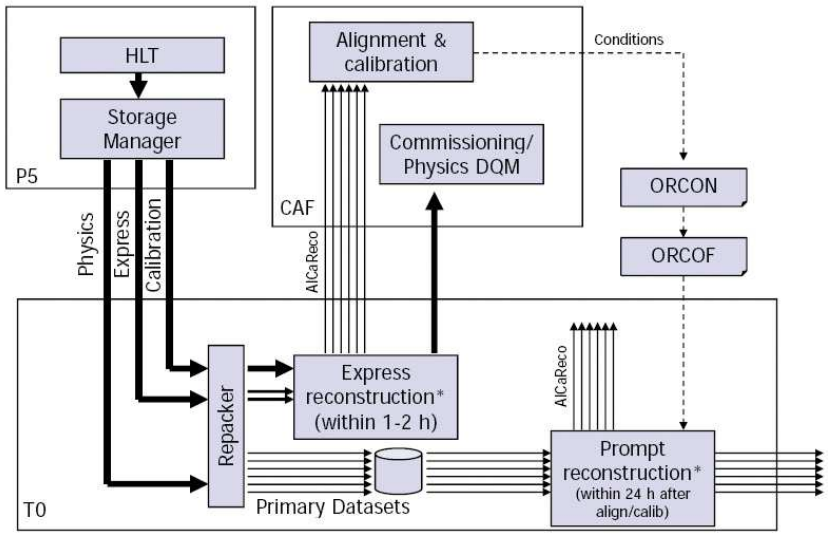

Figure 3.7: *CMS Alignment data flow.*

3.7 First experience of Tracker alignment using cosmic ray particles

A unique opportunity to gain experience in alignment of the CMS silicon strip Tracker ahead of the installation in the underground cavern came from tests performed at the Tracker Integration Facility (TIF) [29].
During several months of operation in the Spring and Summer of 2007, about five million cosmic track events were collected. The Tracker was operated with different coolant temperatures ranging from $+15°C$ to $-15°C$. About 15% of the Strip Tracker was powered and read-out simultaneously. An external trigger system was used to trigger on cosmic track events. The Pixel Tracker was only trial-inserted at TIF and was not involved in data taking. The soft cosmic muon spectrum and the absence of any magnetic field however limited the precision that could be achieved from alignment procedure. In fact, the momentum distribution of the cosmic muons was expected to have a mean value of a few GeV. Given the large material budget of the Tracker (at vertical incident angle about 50% of a radiation length), the alignment resulted in being limited by the multiple scattering. Moreover, the absence of the magnetic field did not allow the momentum to be determined. As explained in the following sections, an average momentum for track reconstruction was used and therefore any residual between the tracks and the measured hits could not be properly accounted to come either from a genuine misalignment or due to a multiple scattering effect.

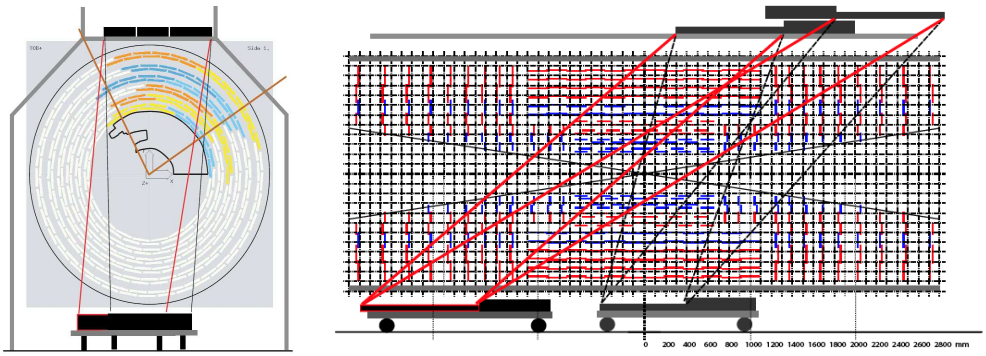

Figure 3.8: *Layout of the Strip Tracker and of the trigger scintillators at TIF, front (left) and side view (right). The acceptance region is indicated by the straight lines connecting the active areas of the scintillators above and below the Tracker. On the right, configuration A corresponds approximately to the acceptance region defined by the right bottom scintillator; configuration B corresponds to the left bottom scintillator; and configuration C combines both.*

3.7.1 Setup at the Tracker Integration Facility

Three trigger configurations were used in TIF data-taking, called A, B and C and shown in Fig. 3.8. The total number of detector modules powered and read-out includes 444 modules in TIB (16%), 720 modules in TOB (14%), 204 modules in TID (25%), and 800 modules in TEC (13%), all located at $z > 0$. Lead plates were included above the lower trigger scintillators, which enforced a minimum energy of the cosmic rays of 200 MeV to be triggered. The data were collected in trigger configuration A at room temperature (+15°C), both before and after insertion of the TEC at $z < 0$. All other configurations (B and C) had all strip detector components integrated. In addition to room temperature, configuration C was operated at +10 °C, -1 °C, -10 °C, and -15 °C. Due to cooling limitations, a large number of modules had to be turned off at -15 °C. The variety of different configurations allowed to study alignment stability with different stress and temperature conditions. Table 3.3 gives an overview of the different datasets. Alignment performance were also evaluated using simulated datasets: a sample of approximately three million cosmic events was simulated using the CMSCGEN simulator [30]. To extend CMSCGEN's energy range, events at low muon energy have been re-weighted to adjust the energy spectrum to the CAPRICE data [31]. Only muons inside specific geometrical ranges were selected to simulate the scintillator trigger configuration C.

Label	Trigger Position	Temperature	N_{trig}	Comments
A_1	A	15°C	665 409	before TEC- insertion
A_2	A	15°C	189 925	after TEC- insertion
B	B	15°C	177 768	
C_{15}	C	15°C	129 378	
C_{10}	C	10°C	534 759	
C_0	C	-1°C	886 801	
C_{-10}	C	-10°C	902 881	
C_{-15}	C	-15°C	655 301	less modules read out
C_{14}	C	14.5°C	112 134	
MC	C	–	3 091 306	simulation

Table 3.3: *Overview of different datasets, ordered in time, and their number of triggered events N_{trig} taking into account only good running conditions.*

3.7.2 Track reconstruction and selection

As mentioned in Section 2.5 charged track reconstruction includes three essential steps: seed finding, pattern recognition, and track fitting. The CTF algorithm, thought for collision track topology, was used in this study after the appropriate modifications. Furthermore, in order to recover tracking efficiency which is otherwise lost in the pattern recognition phase because hits are moved outside the standard search window defined by the detector resolution, alignment position error APE were introduced. They are added quadratically to the hit resolution, and the combined value is subsequently used as a search window in the pattern recognition step. The APE used for the TIF data modeled the assembly tolerances [15].
There are several important aspects of the TIF configuration which require special handling with respect to normal data-taking. First of all, no magnetic field was present. Therefore, the momentum of the tracks could not be measured and an estimate of the energy loss and multiple scattering could be done only approximately. A track momentum of 1 GeV was assumed in the estimates, which was close to the average cosmic track momentum obtained in simulated spectra. Other TIF-specific features were due to the fact that the cosmic muons do not originate from the interaction region. Therefore the standard seeding mechanism was extended to use also hits in the TOB and TEC, and no beam spot constraint, obviously, was applied.
Reconstruction of exactly one cosmic muon track in the event was required. A number of selection criteria was applied on the hits, tracks, and detector components subject to alignment, to ensure good quality data. This was done based on trajectory estimates and the fiducial tracking geometry. In addition, hits from noisy clusters or from combinatorial background tracks were suppressed by quality cuts on the clusters. A hit is kept for the track

fit:

- if it passes a cluster charge cut (at least 50 ADC counts[2]). If the hit is bi-dimensional, both components must satisfy this requirement.
- if it is isolated, i.e. if any other reconstructed hit is found on the same module within 8.0 mm, the whole track is rejected. This cut helps in rejecting fake clusters generated by noisy strips and modules.
- if it is not discarded by the outlier rejection step during the refit as explained below.

The detailed track selection was as follows:

- the direction of the track trajectory satisfies the requirements: $-1.5 < \eta < 0.6$ and $-103^\circ < \phi < -69^\circ$ rad, according to the fiducial scintillator positions.
- the χ^2 value of the track fit, normalised to the number of degrees of freedom, fulfils $\chi^2/\mathrm{ndf} < 4$.
- the track has at least 5 hits associated and among those at least 2 bi-dimensional hits in double-sided modules.

The remaining tracks and their associated hits were refit in every iteration of the alignment algorithms. An outlier rejection technique was applied during the refit: its principle is to iterate the final track fit until no outliers are found. An outlier is defined as an hit whose trajectory estimate is larger than a given cut value ($e_{cut} = 5$). The trajectory estimate of an hit is the quantity: $e = \mathbf{r}^T \cdot \mathbf{V}^{-1} \cdot \mathbf{r}$, where $\mathbf{r}$ is the 1- or 2-dimensional local residual vector and $\mathbf{V}$ is the associated covariance matrix. If one or more outliers are found in the first track fit, they are removed from the hit collection and the fit is repeated. This procedure is iterated until there are no more outliers or the number of surviving hits is less than 4.
These cuts listed above were common to all alignment algorithms. The combined efficiency for all the cuts above was estimated to be 8.3% on TIF data (the C_{-10} sample is used in this estimate) and 20.5% in the TIF simulation sample, mainly coming from track selection, rather than from hit one.

3.7.3 Alignment strategy

Accurate studies were performed with all three algorithms in order to determine the maximal set of detectors that can be aligned and the aligned coordinates that were sensitive to the peculiar track pattern and limited

[2]The average value of the noise at TIF was about 3 ADC counts

statistics of TIF cosmic track events.
For the subdetectors of the Tracker barrel (TIB and TOB), the collected statistics was sufficient to align down at the level of single modules if restricting to a geometrical volume corresponding to the positions of the scintillators used for triggering. The detectors aligned are those whose centres lie inside the geometrical ranges $z > 0$ cm, $x < 75$ cm and $0.5 < \phi < 1.7$ rad where all the coordinates are in the global CMS frame. The degrees of freedom aligned for each module are

- u, v, γ for TOB double-sided modules,
- u, γ for TOB single-sided modules,
- u, v, w, γ for TIB double-sided modules and
- u, w, γ for TIB single-sided modules.

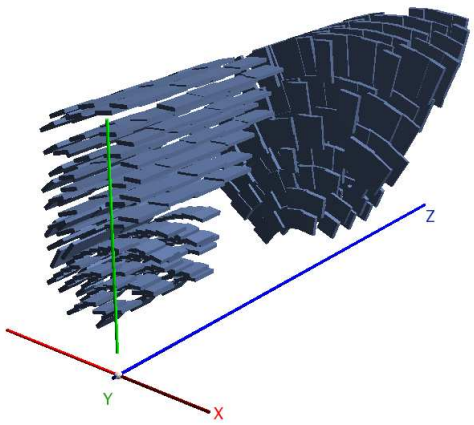

Figure 3.9: *Sketch of the modules used in the track-based alignment procedure at TIF. Selected modules were based on the common geometrical and track-based selection for the algorithms.*

Due to the rapidly decreasing cosmic track rate $\sim \cos^2 \psi$ (with ψ measured from zenith) only a small fraction of tracks crosses the endcap detector modules at an angle suitable for alignment. Therefore, the TEC at $z > 0$ cm could be aligned only at the level of disks. All nine disks are considered in TEC alignment, and the only aligned coordinate is the rotation $\Delta\phi$ around the CMS z-axis. Because there are only data in two sectors of the TEC, the track-based alignment is not sensitive to the x and y coordinates of the disks. The Tracker Inner Disks (TID) are not aligned due to lack of statistics. Figure 3.9 shows a 3D view of the modules selected for the track-based alignment procedure.

Global method approach

Alignment with global method was performed at module level in both TIB and TOB, and at disk level in the TEC, in a single step only, and starting from design geometry. To fix the six degrees of freedom from global translation and rotation, equality constraints were used on the parameters in the TOB: these fix overall shifts and rotations of the TOB, while the TIB parameters were free to adjust to the fixed TOB position. In addition, TEC disk one, which is the closest to the TOB, was kept as fixed. All the criteria described in Section 3.7.2 were applied to select tracks, except hit outlier rejection since outliers down-weighting is already applied within the minimization process inside the `Pede` program. Since global method internally refits the tracks, it was additionally required that a track hit at least five of those modules included in the alignment procedure. Multiple scattering and energy loss effects were treated, as for the sequential method, by increasing and correlating the hit uncertainties, assuming a track momentum of 1.5 GeV, larger than the one used in standard reconstruction. This limits the accuracy of the assumption of uncorrelated measured hit positions in Equation 3.2.
The alignment parameters were calculated for all modules using the common selection of alignables described above. Due to the fact that barrel and endcap were aligned together in one step, no request on the minimum number of hits in individual subdetectors for a selected track is done. The minimum number of hits required for a module to be aligned is set to 50.

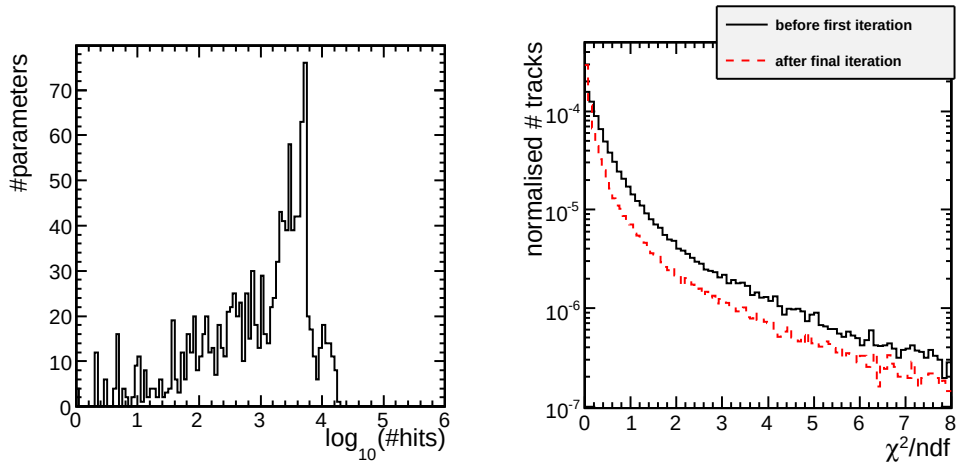

Figure 3.10: *Number of hits for the parameters aligned with global method (left) and improvement of the normalised χ^2 distribution as seen by global method algorithm (right).*

Due to the modest number of parameters, the matrix Equation 3.5 was solved by inversion with five iterations. In each iteration, the track fits were

repeated four times with alignment parameters updated from the previous one. Except for the first track fit iteration, down-weighting factors are assigned for each hit depending on its normalized residuum of the previous fit. About 0.5% of the tracks with an average hit weight below 0.8 are rejected completely.
Figure 3.10 shows, on the left, the number of hits per alignment parameter used for the global minimisation: 58 modules fail the cut of 50 hits. On the right, the normalised χ^2 distributions of the global method internal track fits before and after minimisation are shown. The distributions do not have a peak close to unity, indicating that the hit uncertainties are overestimated. Nevertheless the effect of minimisation can clearly be seen.

Other algorithms approaches

The overall alignment result with local method was obtained in three steps starting from design geometry, first excluding TIB hits from the track fit and aligning only TOB modules. During the second step TOB modules were kept fixed (global reference frame) to the found positions, while the TIB modules were aligned exploiting the hits on them. A third step was performed in order to align TEC disks starting from the previously aligned barrel geometry. In this approach local method made use of APE set to expected positioning uncertainties after assembly at the first step and then decreasing values linearly with the iteration number.
Alignment with sequential method in the barrel region was carried out starting from the module survey geometry. Then the alignment parameters were calculated for all modules in TIB and TOB at once, using the common selection described in Section 3.7.2. The tracking was adapted to the needs of the algorithm, especially to include the current estimate of the alignment parameters. No APE were used, since for every module the position error can be calculated from the up-to-date parameter errors. TEC alignment was determined on disk level, using disk 1 as a reference and the error on the calculated parameters was increased from disk one to disk nine, since the total number of hits per disk decreases moving far from the barrel.

3.7.4 Results and validation

Despite the limited precision of the alignment, that prevents detailed studies of systematic distortions, the results obtained provide an important validation of Tracker alignment for the set of active modules at TIF. The validation of the alignment parameters found and the correspondent module positions was carried out using two different approaches. The former made use of tracks, by refitting the trajectory with the aligned geometry and looking at the track χ^2 and residuals performance. It should be noticed as the sample of tracks used for the validation is a subsample of the one used in the align-

ment procedure, making the validation not statistically independent. This choice was imposed by the lack of further cosmic muon events collected in the same TIF configuration. The latter was performed directly comparing geometries coming from different sets of alignment constants.
In the following sections, the evolution of the module positions is shown starting from the design geometry, moving to survey measurements, and finally comparing to the results from the track-based algorithms: both the overall track quality and individual hit residuals improve in the three stages. Furthermore, is shown as all three track-based algorithms produce similar results when the same input and similar approaches are taken. Finally, an attempt to estimate the residual misalignment using Monte Carlo simulation has been performed.

Validation of survey precision and track-based alignment result

The position of modules recorded during the Tracker assembling and mounting phase and those predicted after the alignment algorithm procedure were the input of a track based validation, performed by refitting tracks passing some loose selection cuts, like at least 6 hits, where more than one to be two-dimensional, with all APE values set to 0.
Improvements of the track χ^2 can be observed when design geometry, survey measurements, and track-based alignment results are compared, as shown in Figure 3.11. As the logarithmic scale plot shows, the main differences are found to be in the tails of the distributions.

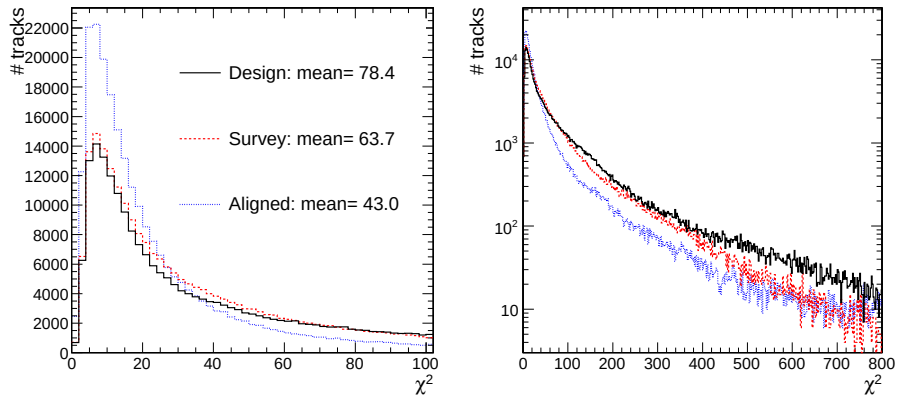

Figure 3.11: *Distributions of the absolute χ^2-values of the track fits for the design and survey geometries as well as the one from track-based alignment. APE values are set to zero.*

A further validation of survey geometry is also visible in the hit residuals shown in Figure 3.12. Residuals distribution, shown as the difference be-

tween the measured hit position and the track position on the module plane, using survey and aligned geometry have mean values closer to zero and the standard deviation smaller than using the design geometry. To avoid a bias, track position is predicted without using the information of the considered hit (*unbiased residual*). In addition to misalignment, hit residual distributions depend on the intrinsic hit resolution and on the track prediction uncertainty. For low-momentum tracks, as expected to dominate the TIF data, the latter is large. For a momentum of 1 GeV and an extrapolation between hits in two adjacent TOB layers, the average multiple scattering displacement is about 250 μm. So even with perfect alignment one expects a width of the residual distribution that is significantly larger than the intrinsic hit resolution of $23 - 53$ μm in the barrel [15]. In the Chapter 4, a way to disentangle these random effects from the real remaining statistical misalignment will be presented.

Validation of the results obtained from the three algorithms

The three geometries found by the alignment algorithms used at TIF were also compared in order to check the consistency of the methods, given the different statistical approaches they used in the minimization procedure. Figure 3.13 shows similar distributions of the track χ^2: local method gives the smallest mean value, whereas sequential method and global method have more tracks at low χ^2 values as can be seen in the logarithmic scale plot. Global method lead to a larger tail, but more tracks are present at low χ^2 than using the local method.
The three algorithms also have consistent residuals in all Tracker sub-detectors as shown in Figure 3.14, though the most relevant comparison is in the barrel region (TIB and TOB) since the endcaps were not aligned at the module level. For both Figures 3.13 and 3.14, only modules selected for alignment have been taken into account in the refit and in the residual distributions.
Another way of validating alignment results is the comparison, module by module, of the obtained positions from the three statistical approaches. This is done by showing differences between the same module coordinate in two geometries (e.g. ideal and aligned) with respect to their geometrical position (e.g. r, ϕ or z) or correlating these differences as seen by two different methods.
The results of comparison of different geometries are shown in Figure 3.15 and the numerical values are reported in Table 3.4. The horizontal global coordinate x is chosen in comparison because among the three global coordinates it is the closest to the most sensitive coordinate measured with vertical cosmic tracks. The two geometries under consideration, which are either one of the three alignment algorithm results or the design geometry, have been adjusted in space globally to match their coordinate system for each sub-detector. The agreement in global x coordinate is about 60

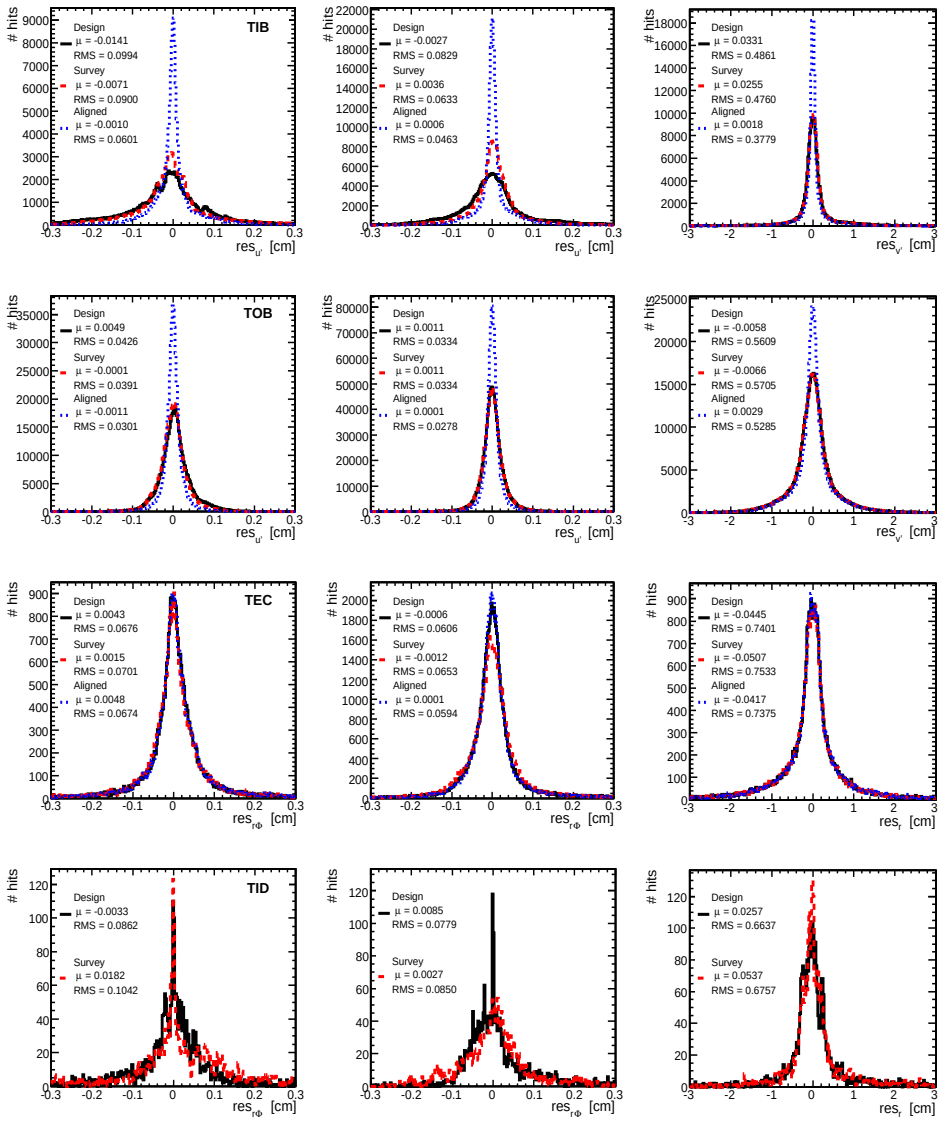

Figure 3.12: *Hit residuals for different geometries: ideal (solid/black), survey (dashed/red), and track-based alignment (dotted/blue). Four Tracker subdetectors are shown in the top row (TIB), second row (TOB), third row (TEC), and bottom row (TID). The absolute local u'-residuals are shown for single-sided modules (left) and double-sided modules (middle), while local v'-residuals are shown for the double-sided modules only (right). For the endcap modules (in TEC and TID) transformation to the $r\phi$ and r residuals is made.*

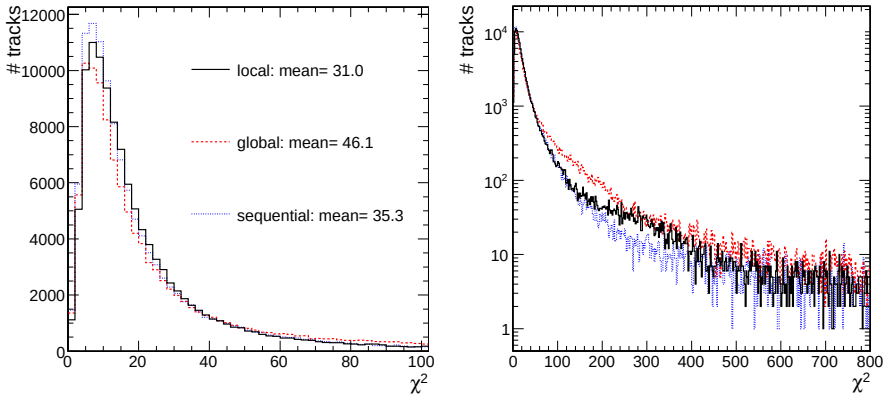

Figure 3.13: *Distributions of the χ^2-values of the track fits for the geometries resulting from local method, sequential method, and global method alignment. The track fit is restricted to modules aligned by all three algorithms.*

Geom 1	Geom 2	TIB	TIB (SS)	TIB (DS)	TOB	TOB (SS)	TOB (DS)
local m.	design	507	420	527	124	96	142
glob. m.	design	512	369	452	116	98	133
seq. m.	design	503	440	477	107	91	140
seq. m.	local m.	119	89	168	70	51	54
glob. m.	local m.	127	111	156	80	62	70
seq. m.	glob. m.	146	115	181	65	45	54

Table 3.4: *Comparison of the RMS in global x difference (in μm) of module positions in TIB and TOB between different geometries indicated in the first two columns. Single-sided (SS) and double-sided (DS) modules are shown together and separately.*

μm in TOB and somewhat above 100 μm in TIB. However, these numbers cannot be interpreted as precision of the module positions with respect to the charged particle track and are expected to be worse because for some modules the most sensitive coordinate is not coincident with the global x coordinate.

Estimation of achieved alignment precision

An alignment on the simulated Monte Carlo sample, reconstructed with a randomly misaligned geometry, has been performed with the global method with the same settings as for the data, i.e. alignment of a subset of the barrel part at module level and of the TEC at disk level. The resulting distribution of the residuals in TIB, TOB and TEC are shown in Figure 3.16

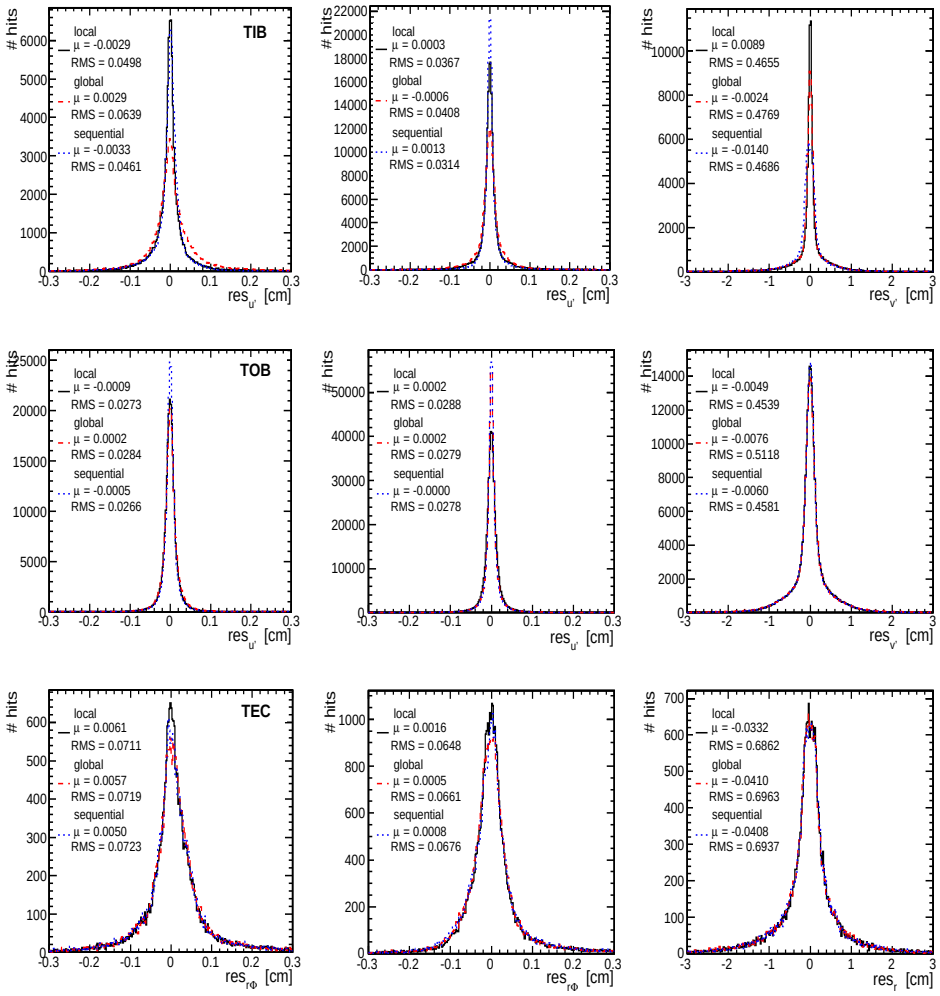

Figure 3.14: *Hit residuals for different geometries from three track-based algorithms: local method (solid/black), global method (dashed/red), and sequential method (dotted/blue) based alignment. Three Tracker sub-detectors are shown in the top row (TIB), second row (TOB), and bottom row (TEC). The absolute local u'-residuals are shown for single-sided modules (left) and double-sided modules (middle), while local v'-residuals are shown for the double-sided modules only (right). For the endcap modules (TEC) transformation to the $r\phi$ and r residuals is made. The track fit is restricted to modules aligned by all three algorithms.*

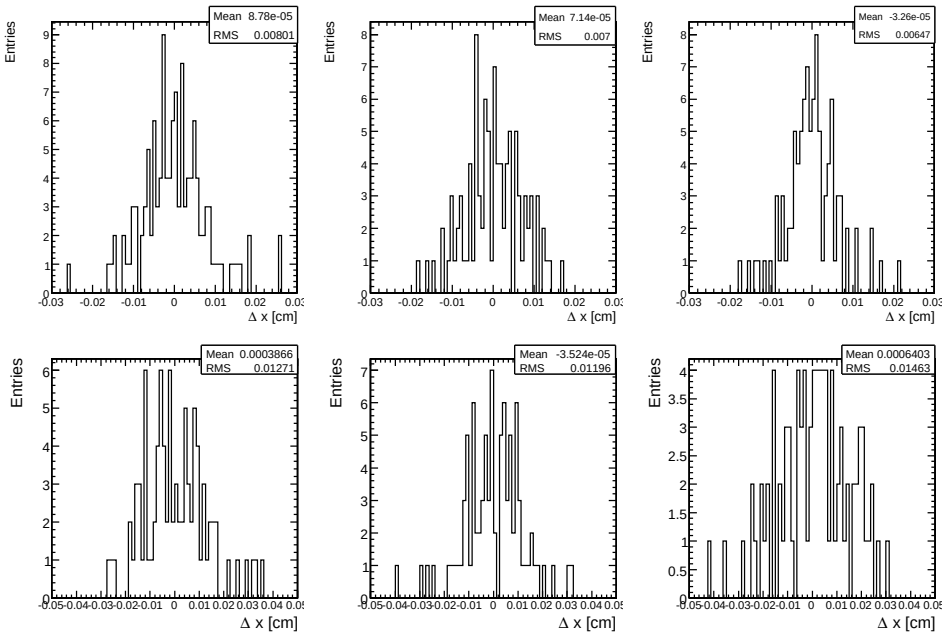

Figure 3.15: *Differences in horizontal position (Δx) of TOB modules used in alignment (top) and TIB modules in the fiducial region* $0.70 < \phi < 1.35$ *(bottom) between global and local method (left), sequential and local method (middle), and sequential and global method (right).*

and compared with the initial *startup* misalignment scenario[3] and design geometry. In this misalignment scenario applied here, modules are randomly shifted according to the estimated level of knowledge of Tracker after input from assembly measurements, survey, Laser Alignment System and cosmic muons [32]. Comparison with the distributions obtained from data using the design geometry, shown in Figure 3.14, reveals that in TIB and TOB the starting misalignment is overestimated while in TEC it is slightly underestimated. The widths of residuals after alignment are generally much smaller than those obtained from the aligned data, especially in the TIB. This could be due to the larger statistics of the simulation data sample, but also due to effects not properly simulated, e.g. relative misalignment of the two components of a double-sided module or possible differences in the momentum spectrum of Monte Carlo.
Using simulated data sample and results obtained after alignment on data, a trial and error procedure has been performed in order to provide an estimation of the remaining random misalignment of the modules. The procedure consists of the following steps:

- Modules not selected for alignment are excluded from the residual distribution and from track refits.
- Truncated mean and RMS values are calculated from the central 98.76% interval of each distribution, corresponding to $2.5\,\sigma$ for a Gaussian-distributed variable for each layerwise residual distribution (TIB and TOB) after alignment on data.
- Residuals from the first and the last hit of the track are not considered, since track prediction is an extrapolation to the first and last hit of a track, leading to large track pointing uncertainties.
- The modules in TIB and TOB have been randomly shifted in three dimension according to Gaussian distributions: different misalignment scenarios have been applied to the design ("true") Tracker geometry used in reconstructing the simulated data.
- Several scenarios are applied until truncated RMS of their layerwise residual distributions are found to be similar to those in data in all layers.

Figure 3.17 shows the results from the simulation when reconstructed with the design geometry and with a random gaussian misalignment with RMS of 50 μm and 80 μm in the TOB and the TIB, respectively. In addition also the truncated mean and RMS values from data before and after alignment are reported. It can be clearly seen that the simulation with the ideal, i.e.

[3]See Section 5.1 for the definition of *scenario*. This *startup* scenario differs from the one described in Section 5.1.

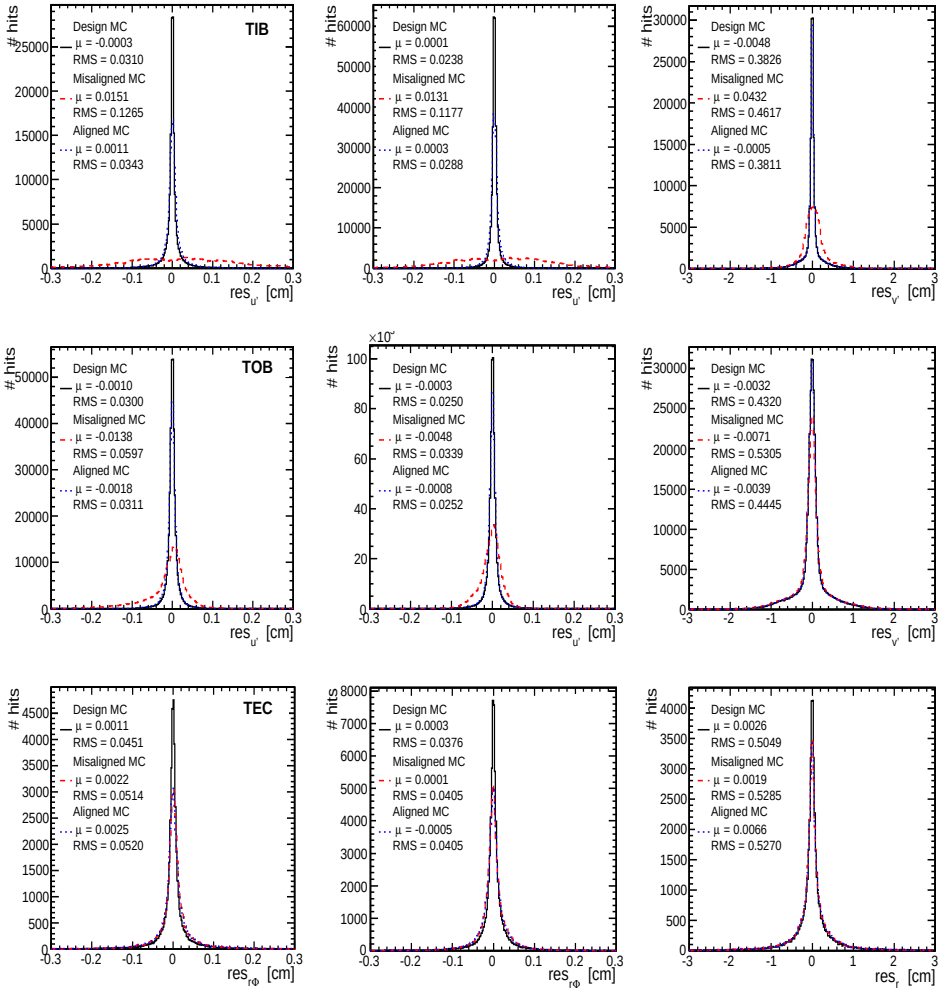

Figure 3.16: *Hit residuals for different geometries in different conditions for the simulated data sample: ideal geometry (solid/black), misaligned geometry according to expected starting misalignment (dashed/red), and geometry after alignment (dotted/blue). Three Tracker sub-detectors are shown in the top row (TIB), second row (TOB), and bottom row (TEC). The absolute u'-residuals are shown for single-sided modules (left) and double-sided modules (middle), while v'-residuals are shown for the double-sided modules only (right). For the endcap modules (TEC) transformation to the $r\phi$ and r residuals is made.*

true, geometry has smaller widths than the data, especially in the TIB. On the other hand, the geometry with a simulated misalignment of 50 μm and 80 μm RMS, respectively, matches rather well the data after alignment, such that these numbers can be taken as an estimate of the size of the remaining misalignment.

Beside the validation of the results and the estimation of the statistical precision achieved at TIF, important checks regarding the stability of Tracker geometry with respect to the cooling temperature and stress due the TEC insertion were performed, in order to guarantee the stability of the whole system and check the response to a thermal gradient. All the geometry deviations found at different temperatures appeared to be within the statistical scatter of 100 μm, and there is no evidence of any coherent movements. Some small layer-wise shifts were visible in the barrel region using datasets before and after TEC insertion. It was also possible that these effects were artificial, due to the lack of information to constraint the weak degrees of freedom of the system or to the different track sample used for the alignment in different configurations.

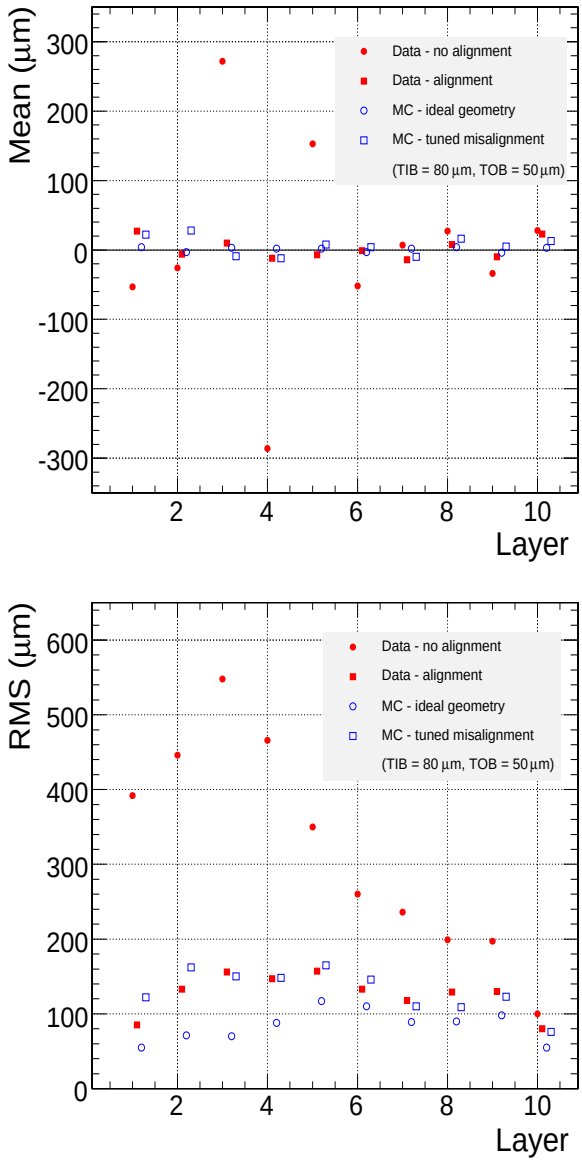

Figure 3.17: *Hit residual means in u' coordinate (top) and RMS (bottom) in ten layers of the barrel Tracker, i.e. four layers of TIB and six layers of TOB, shown in data before track based alignment (red full circles), after track based alignment (red full squares), in simulation with ideal geometry (blue open circles) and in simulation after tuning of misalignment according to data (blue open squares).*

Chapter 4

Full scale alignment of the Tracker with cosmics ray particles

During Fall 2008 the CMS collaboration conducted a long-month data taking exercise known as the Cosmic Run at Four Tesla (CRAFT) with the goal of commissioning the detector before entering in the *pp* collision phase. This was a unique opportunity for testing the CMS performance with all installed detector systems partecipating, with the goal of commissioning the solenoid magnet at its operating field, gaining experience operating CMS continuously for a month and finally checking the offline workflows stream and storage of the data. During this phase almost 270 million cosmic triggers were collected with all detector systems operating in the 3.8 T magnetic field with a L1 trigger rate of 600 Hz. Recorded events were processed by the offline data handling system, and then analyzed by teams dedicated to the calibration, alignment, and characterization of the detector subsystems. As shown in Figure 4.1, most of the detector systems partecipated with more than 95% of their components switched on and the detected inefficiency of read-out channels was mainly due to electronic failures or cabling issues which have been recovered during the subsequent shutdown period following the CRAFT operations. As CMS is located 100 m below the surface of the Earth, the cosmic muon rate relative to that at the surface is suppressed by approximately two orders of magnitude. The typical L1 trigger rate was 600 Hz, composed of about 300 Hz of cosmic triggers using all three muon systems, 200 Hz of low threshold triggers from the calorimeters, and 100 Hz of calibration triggers used to pulse the front-electronics. This rate is well below the 100 kHz design limit for the central data acquisition system. Therefore, the cosmic muon triggers were more relaxed than those designed for collisions, with only loose requirements for the muon to point to the interaction region of the experiment.

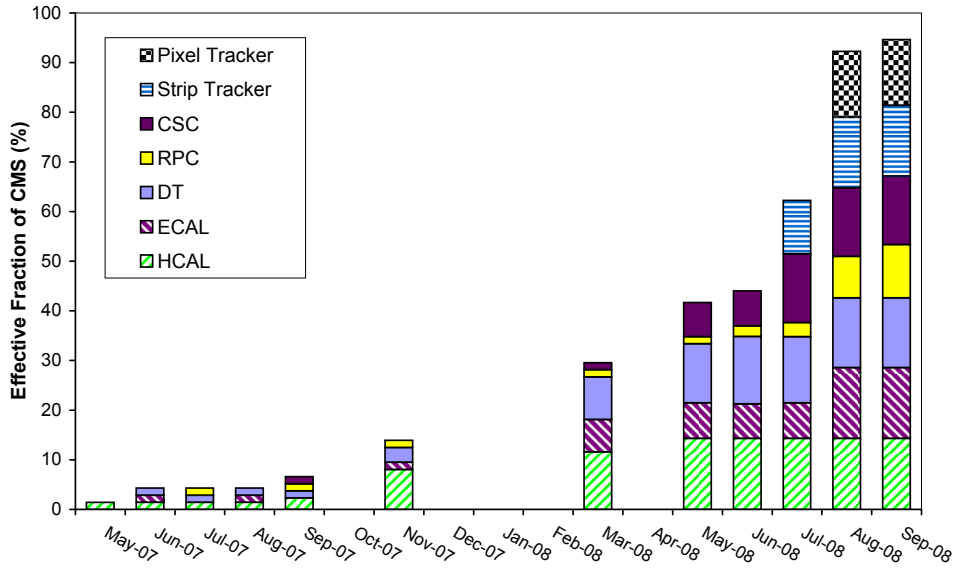

Figure 4.1: *Effective fraction of the CMS experiment participating in the 2007 and 2008 global run campaigns as a function of time. The fraction of each of the seven major detector systems is represented by a bar. Only one RPC endcap was missing by September 2008 [34].*

The rate of triggered cosmic muons crossing the Tracker region was about 6 Hz. The time-of-flight of cosmic muons to cross from the top to the bottom of the experiment was accounted for by introducing coarse delays of the muon trigger signals in the top half such that they are in rough coincidence with the bottom half: a two bunch crossing difference for the barrel, and one for the endcaps, where one bunch crossing corresponds to 25 ns.
A reconstructed event, a cosmic muon traversing the detector from top to bottom in the bending plane, detected by CMS is shown in Figure 4.2: muon chambers provide the trigger and particle identification while reconstruction and track parameters measurement are completed by adding the information of Tracker inner region and minimum ionizing deposits in the calorimeters.

4.1 Tracker setup and performance during CRAFT

The Tracker was active 95% of the running time during CRAFT, with 98% of the channels active [36]. Due to the small cosmic muon rate, events with more than one track are rare. Since data were zero suppressed during the

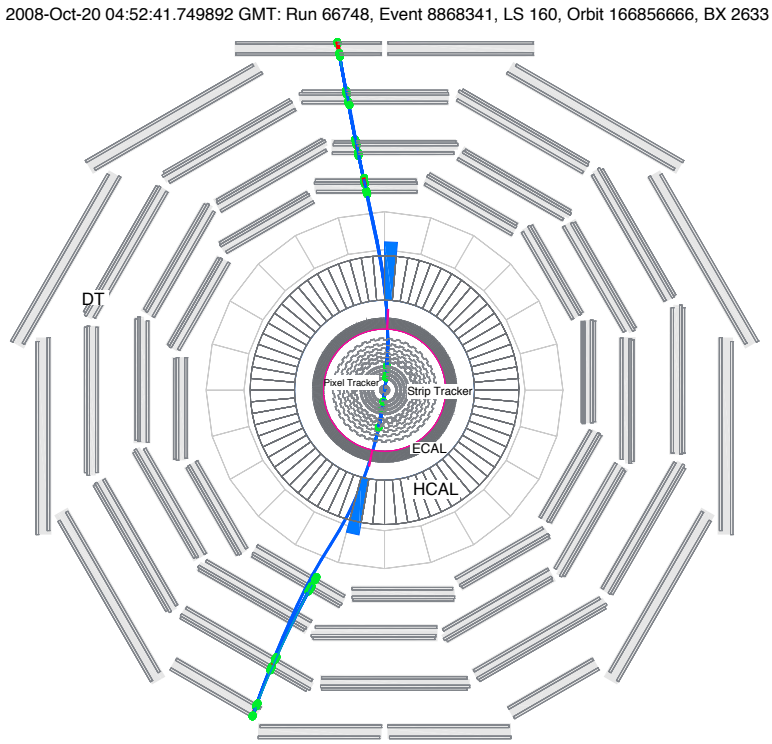

Figure 4.2: *Display of a cosmic muon recorded during CRAFT which enters and exits through the DT muon system, leaves measurable minimum ionizing deposits in the HCAL and ECAL, and crosses the silicon strip and pixel tracking systems. Reconstruction of the trajectory is also indicated [34].*

entire exercise, only a tiny fraction of the Tracker channels are read out, leading to an average occupancy of 4×10^{-4}. The sensor signals were read out in *peak mode*, and the readout was synchronized to triggers delivered by the muon detectors. A few issues not identified during the previous commissioning of the detector, such as some swapped cables and incorrect fibre length assumptions used in the latency calculations, were quickly identified by offline analysis of the cosmic data and corrected either during operation or the subsequent shutdown. The signal-to-noise ratio, which is a benchmark for the performance of the Tracker, was found to be in the range 25-30 for thin modules and 31-36 for thick ones, and within 5% from the expected values. The probability to find a cluster in a given silicon sensor that has been traversed by a charged particle (hit efficiency) has been measured as well, leading to values greater than 99% for most layers/disks. For the Pixel Tracker, the detector intrinsic position resolution is measured using tracks that traverse overlapping sensors and results are shown in Figure 4.3.

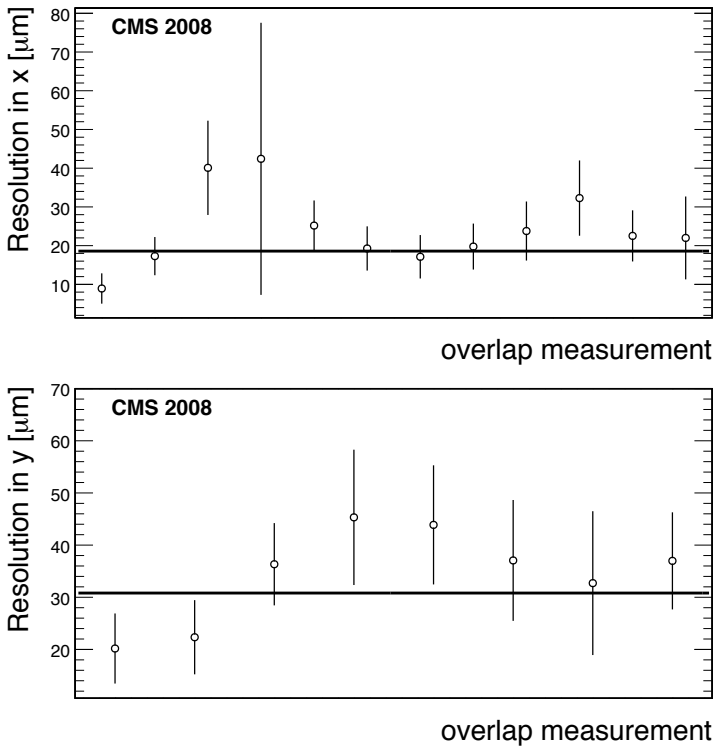

Figure 4.3: *Hit position resolution of the barrel pixel detector along the local transverse (top) and longitudinal (bottom) coordinates measured using overlapping sensors within a layer. Each measurement point corresponds to a different pair of overlapping modules in z for the top plot and in r-ϕ for the bottom one with at least 30 crossing tracks. The circles show the measurement while the solid line represents the error-weighted mean of the measurements [35].*

The performance of the track reconstruction using the full Tracker, including the pixel detector, were checked in detail using the two main algorithms CTF and CosmicTF (see Section 2.5.2). As Figure 4.4 shows, by design the CosmicTF reconstructs only one track, while CTF is capable of reconstructing more than one track per event, but as it has not been optimised to reconstruct showers, multi-track events tend to contain a number of fake or badly reconstructed tracks. For this reason only single track events are used in the comparison of right plot in Figure 4.4 where there is a significant number of tracks with a high number of hits, indicating that tracks can be followed through the whole Tracker and be reconstructed with hits in both the upper and lower hemispheres.

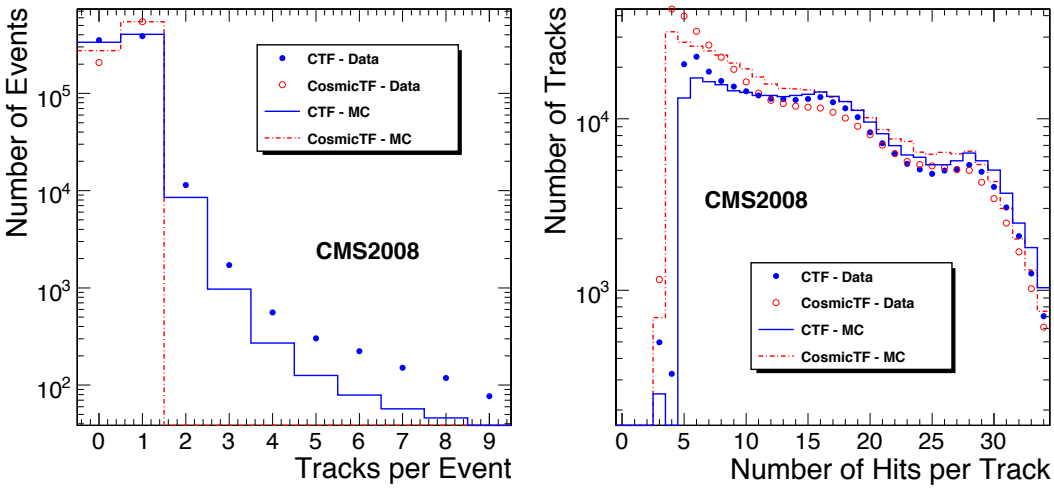

Figure 4.4: *Left. Distribution of the number of tracks reconstructed per event with the CTF and CosmicTF algorithms. For each algorithm, the total number of simulated Monte Carlo tracks are normalised to the number of observed tracks. Right. Distribution of the number of hits per track in single track events [36].*

4.2 Alignment strategy

A set of almost 4.5 million AlCaReco events from the *TkAlCosmics* stream (Section 3.6) have been used for the track based alignment of the Tracker [33]. On this available data set quality cuts both on hits and on tracks, were applied in order to get a clean sample of tracks which can be directly used as input for alignment algorithm minimization process (Table 4.1). The APE used for the initial track reconstruction were large as they had to account for possible large displacements of the entire sub-detectors while still guaranteeing an efficient track-hit association. The CTF algorithm was used to reconstruct the cosmic muon trajectory. In total, about 3.2 million tracks were selected for alignment, out of which about 110 000 had at least one pixel hit ($\sim 3.5\,\%$).
According to the description of track model used in the reconstruction, the track assumes an helicoidal parametrization for its trajectory, characterized by a set of five parameters to be determined at the point of closest approach (PCA). Two of them, the momentum and azimuthal angle spectra of cosmic muons, have been validated by a comparison with a Monte Carlo simulation, requiring the same quality cuts: as shown in Figure 4.5, a very good agreement is observed.

In this context, a different alignment strategy with respect to the one

Track quality cuts	**value**
momentum p	> 4 GeV/c
number of hits	≥ 8
number of 2-d hits (on Pixel or DS modules)	≥ 2
χ^2/ndf of the track fit	< 6.0
Hit quality cuts	**value**
S/N (Strip modules)	> 12
pixel hit prob. matching template shape in u (v) dir.	> 0.001 (> 0.01)
track angle relative to the local uv plane	$< 20°$
square pull of the hit residual	< 15

Table 4.1: *Quality cuts applied to hits and tracks used in the alignment at CRAFT.*

adopted during TIF alignment was used, due to several factors present now: the larger statistics available for the alignment; the presence of a magnetic field which allowed for a measurement of the transverse momentum; the presence of all the modules activated, which allowed the reconstruction of tracks crossing the entire Tracker volume.
Two statistical methods, local (HIP) and global (Millepede), were run independently to solve the alignment problem, but the best results were obtained by applying the two algorithms in sequence in order to take advantage of their complementary strength. This approach will be referred to as *combined* method in the following.
The large statistics allows for a separate alignment of the *stereo* and $r\phi$ component of the double-sided modules, leading to a dramatic improvement in track residuals. Single-sided silicon strip modules can provide only a one-dimensional measurement in the module plane, along the local u-coordinate: the v-coordinate is only known to be within the module boundaries, with precision not sufficient for track reconstruction requirements. On the other hand, the information from the $r\phi$ and *stereo* modules in a double-sided module is combined into a two-dimensional measurement in the combined module plane in both u and v for the pattern recognition phase. Due to the 100 mrad stereo angle between the $r\phi$ and stereo modules (see Figure 4.6), a small displacement in u is equivalent to a ten times larger displacement in v. Given comparable mounting precision of modules in u and v, it was found from the data after several attempts of alignment of double-sided modules in v, that parameters obtained were much larger than the known assembly accuracy. Figure 4.7 reports the shifts, calculated from design geometry in TIB, of the modules inside the supporting frame: after an alignment with global method along the both u and v of double-sided modules, the values found were compared with the survey measurements. It should be noticed as in $r\Delta\phi$ coordinate the agreement between what is recorded by survey

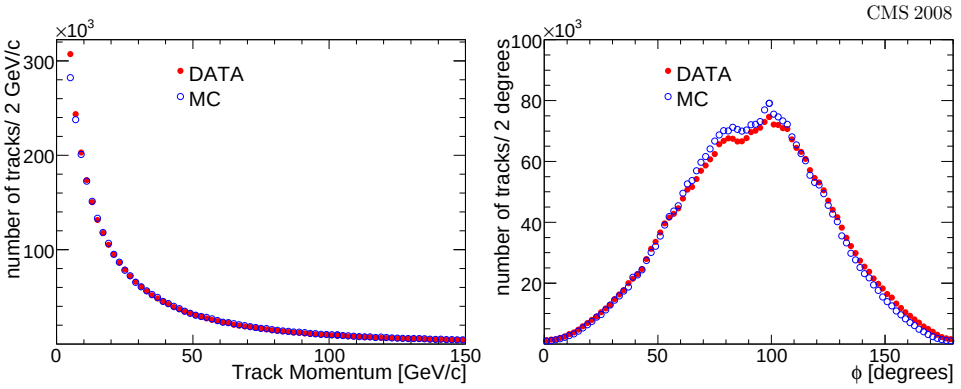

Figure 4.5: *Momentum (left) and azimuthal angle (right) spectra of cosmic muons reconstructed in the CMS tracker volume based on the selection criteria described in the text. The solid (red) circles represent the cosmic ray data whereas the open (blue) circles come from a MC simulation.* $\phi =$ $90°$ *corresponds to vertical cosmic tracks.*

and the shifts found by the algorithm are comparable, while along the longitudinal v they are one order of magnitude larger than known assembly accuracy. This was interpreted as unphysical corrections found by the algorithm. Following this test, the two single-sided modules of a double-sided one were aligned separately, but only in the most precise coordinates (u).

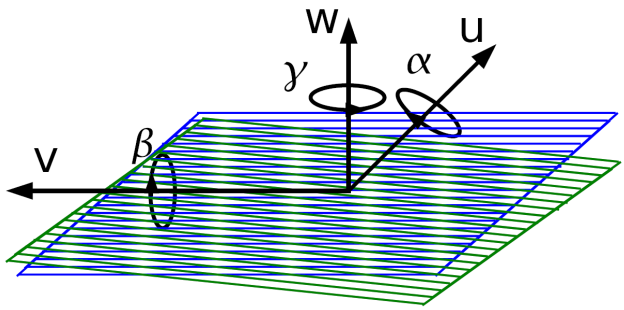

Figure 4.6: *Sketch of Tracker DS module: stereo module (green) is tilted of 100 mrad with respect to the* $r\phi$ *component (blue).*

These consistency checks are extremely important for the alignment procedure: a tight control of the aligned degrees of freedom should be performed, and, in case some final values are found to be not physically acceptable, keep

them as fixed. An internal constraint would be the inclusion of survey measurements in the alignment procedure itself, but currently this feature has been implemented and used for the local algorithm only. Furthermore, the

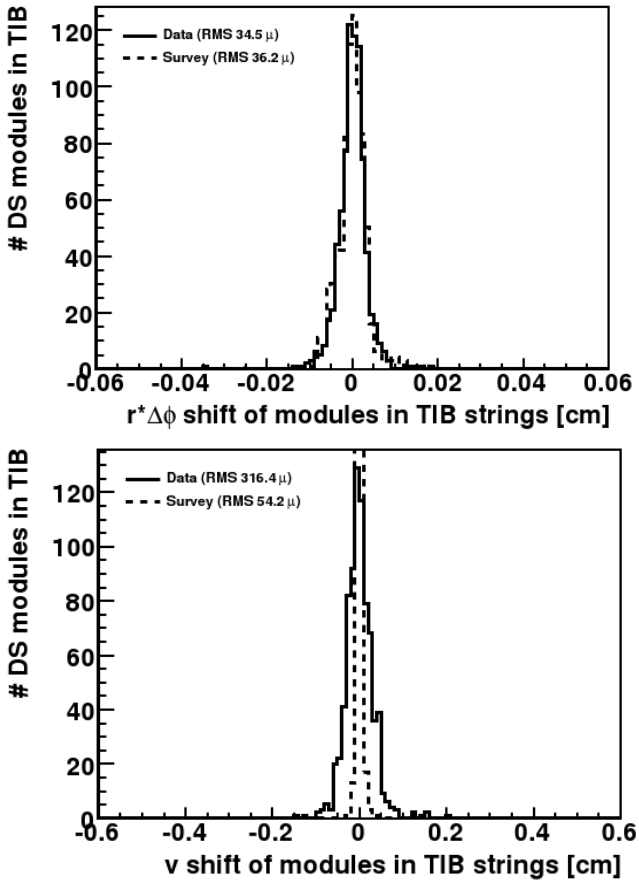

Figure 4.7: *Shifts of the modules inside supporting frame (string) in $r\phi$ (top) and v (bottom) direction with respect to design geometry for TIB double-sided modules: black dashed line is obtained using survey measurements of the module within a string, while black solid line using alignment parameters obtained with global method after the alignment of double-sided modules along v.*

requirement of aligning the full Tracker needs a correct handling of the hierarchical structures when they are aligned together. These two requirements (separate alignment of $r\phi$ and stereo component of double sided modules and description of highly correlated displacements of all modules in a higher level structure) led to multi-step strategies for both alignment methods, as

presented in the following sections.

4.2.1 Alignment with global method

The optimal alignment procedure using the global method was found to consist of three steps. The detector design geometry was chosen as a starting point. One of the feature implemented Millepede algorithm consists in the possibility of assigning starting χ^2 penalties (the so-called presigmas) to the individual alignment parameters, as described in Section 3.5.1. This, beside improving the stability of the matrix equation avoiding numerical problem, provides also an internal reference for the parameter values. Optimal values of the presigmas of the alignment parameters of the modules were found to be a factor of ten smaller than the initial position uncertainties with respect to the next supporting structure. A set of calibrated values of presigmas has been used for the strategy for each of the parameters aligned in the following presented steps (Appendix A).
In the first step the highest level structures (half-barrels, endcaps) with all six degrees of freedom together with all module units, including $r\phi$ and *stereo* strip modules in a double-sided module, with the most sensitive degrees of freedom each (u, w, γ, and for pixel modules also v) were aligned. A limitation of 46 340 parameters in the program used led to selection criteria for modules to be aligned of more than 25 hits per pixel module and more than 425 hits per strip module. This resulted in the alignment of about 90% of all modules. The alignment of the bigger structures is essential to easily spot possible large movement of the whole structure due to some mechanical stresses or thermal effects. It was also observed that the highest level structures alignment, half barrels, together with the lowest ones, module units, introduced a strong internal correlation between structures, preventing systematic expansions and distorsions to occur which, otherwise, would appear in the geometry, particularly in the endcap region.
In the second step all modules, all double-sided or single-sided strip modules with more than 150 hits and all pixel modules with more than 25 hits, were aligned in the TIB in $u, w, \alpha, \beta, \gamma$; in the pixel system in u, v, w, γ; and in u, w, γ elsewhere. Compared to the previous step, this recovered the remaining 10% of the modules and allowed more degrees of freedom for the TIB, which had larger assembly tolerance, but did not allow independent alignment of the $r\phi$ and stereo modules. No alignment of α and β was performed in the TOB thanks to its higher mounting accuracy, and in the TID and TEC, since they were less often traversed by cosmic tracks due to their vertical orientation.
The third step was designed to recover lost correlations between the first two steps and had the same configuration as the first step, but the minimum number of hits in the strip modules was increased to 450 with respect to 425 used in the first step. This decision is driven by the fact that starting

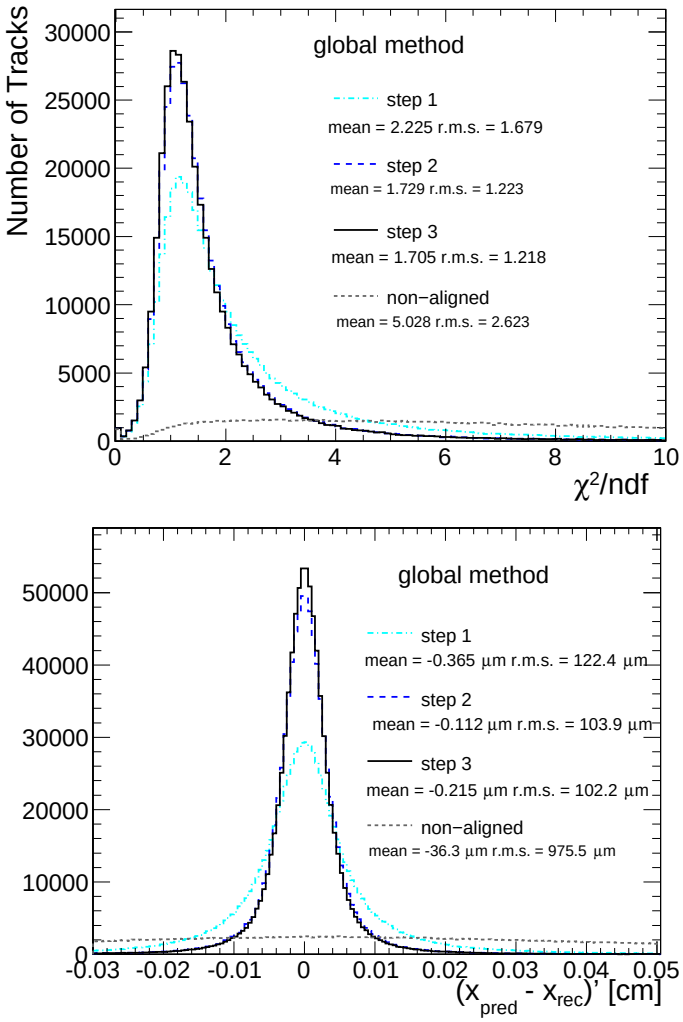

Figure 4.8: *Improvement due to multi-step alignment procedure using global method shown for track χ^2 and TIB residuals distribution. APE values are set to zero.*

geometry for the third step is of better quality with respect to the one at the first step: consequently the failures in the track refitter are less, since now modules are closer to their real position in the geometry and they become more populated. The increase in the requirement on the minimum number of hits allows to keep the number of parameter to be aligned in a single step below the maximum threshold of 46 340.
The quality of the alignment after each step is well visible in the track χ^2 and TIB residuals evolution reported in Figure 4.8: the main improvement

occurs between the first and the second step, while the third one is performed mainly to check the correct positioning along u of the individual components of the double-sided modules, after the alignment of the whole double-sided structure along its local v, performed in the second step.

4.2.2 Alignment with local method

Module positions as determined from optical surveys were used as the starting point in the local method. The alignment with the local algorithm started with the large structures and then proceeded in order of increasing granularity down to the module units in order to speed up convergence. Also, the small fraction (4%) of tracks passing through the pixel detector suggested a modified approach in which the silicon strip modules were first aligned without pixel information. The hits from the structures not yet aligned were excluded from the track fit. The APE values were set high at the beginning of the alignment process (several hundreds of microns depending on the sub-detector), and were progressively reduced to a few tens of microns in subsequent alignment steps.
In the first step (15 iterations), the half-barrels of BPIX, TIB, and TOB were aligned in four degrees of freedom (u,v,w,γ). In order to have a better sensitivity along the global z-direction, only tracks passing through the pixel barrel system were used. In the second step (15 iterations), the endcaps of FPIX, TID, and TEC were aligned in the same four degrees of freedom. The third alignment step (30 iterations) moved the strip modules (treating double-sided modules as rigid bodies) in all six degrees of freedom. The information on the module positions within a higher hierarchy structure, for example within a string of TIB, coming from the optical survey measurements, or design geometry if no survey information was available, was used in the χ^2 minimization, as shown in Equation (3.8). This proved to be useful for both limiting the movement of modules in poorly constrained degrees of freedom and aligning modules that had fewer than the required number of hits. In the fourth step (30 iterations), the strip module units (treating $r\phi$ and *stereo* strip modules in a double-sided module independently) with at least 50 hits were aligned in three degrees of freedom (u, w, γ). In step five (15 iterations), the ladders of the pixel detector were aligned in six degrees of freedom. Finally in the sixth step (15 iterations), the pixel modules with at least 30 hits were aligned in all six degrees of freedom.

4.2.3 Alignment with the combined method

The final alignment parameters were determined starting from the output of the global method analysis, then further aligning the tracker with the local method strategy. This combination was found to provide the best resultsin terms of minimization of residuals: the main effect of global method is

to solve the global correlations, while local method makes use of the same track fit used in the standard CMS reconstruction and exploit the additional informations coming from survey, which can be easily incorporated, allowing for alignment with more degrees of freedom.
The alignment strategy adopted by the local algorithm was modified to exploit the already good starting position of the modules provided by the global method. In the first step of the local method (30 iterations), all strip modules, treating double-sided modules as rigid bodies, were aligned in six degrees of freedom using track and survey information. In the second step (20 iterations), the strip module units, treating $r\phi$ and *stereo* strip modules in a double-sided module independently, were aligned in three degrees of freedom (u,w,γ). Pixel modules were not aligned in the first two steps, although pixel hits were included in the track fit. Finally in the last step (20 iterations), the pixel modules were aligned in six degrees of freedom. Modules for which the fit did not converge were left at the position found by the global algorithm.

4.3 Results and validation

Several approaches were used to validate the alignment results. The quantities that were used in the χ^2 minimization, such as residuals and the χ^2/ndf of the tracks, were monitored. This validation provides a reliable check whether the minimization process has properly worked, but it is not sensitive enough to quote the remaining misalignment of the modules, since many other effects determine the spread of the residual distribution. Another method, consisting in extracting the median value of the residual distribution on each module, was used to quantify the precision achieved in the alignment. Furthermore, the monitoring of the track parameter resolution and the comparison of the positions of modules within differently derived geometries, allowed a better understanding of the alignment accuracy.

4.3.1 Monitoring of track fit quality and hit residuals

The resulting geometry after the alignment procedure was applied in the track reconstruction, using the selection of tracks described in Section 4.2. Due to the limited statistics the same track sample was used both for alignment and validation. All the tracks were refitted with APE calibrated by tuning procedure using the parameters obtained after alignment with combined method. Essentially, they are assumed to be spherical in the space, having the same value for the three spatial directions. The radius of this sphere is assumed to scale as $r_0/\sqrt{N}$. N is the number of hits per module, therefore assigning different weights to APE computed for each module. The r_0 value is set differently for each subdetector, to have the gaussian standard deviation of the distribution of the residuals normalized to their

error, is approximately equal to one. The track χ^2/ndf distribution is shown

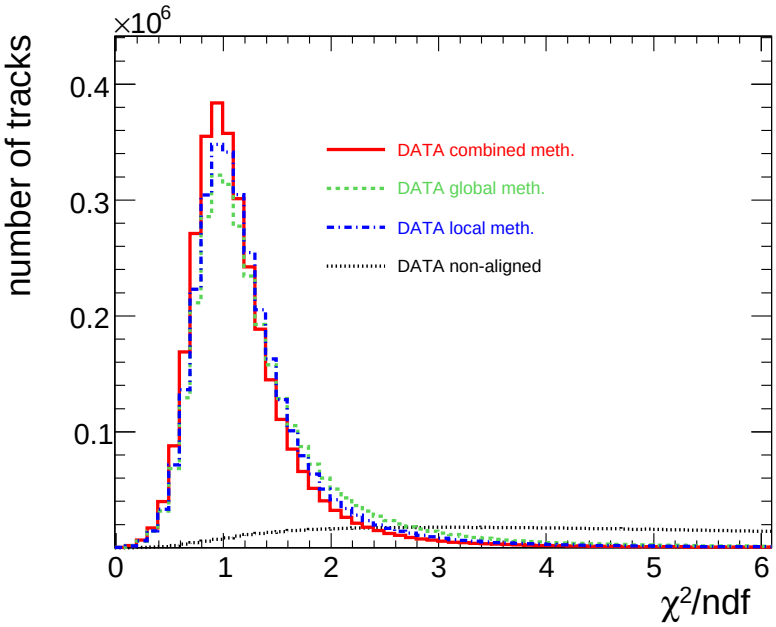

Figure 4.9: *Track χ^2/ndf distributions for non-aligned (dotted line), local method (dashed-dotted line), global method (dashed line), and combined method (solid line) geometries.*

in Figure 4.9, while the hit residuals in the u' and v' directions are shown in Figure 4.10 for the subdetectors in the barrel region. The improvement after alignment is quite evident if compared with non-aligned geometry. The local and global algorithms provide similar results in each subdetector, with the best performance in terms of residual minimization given by the combined method.

4.3.2 Measurement of the alignment precision

The width of the residuals is dominated by two effects other than alignment: track extrapolation uncertainties due to multiple scattering and hit position reconstruction uncertainties. Both of these effects are random, while remaining misalignment produces systematic shifts. For this reason the residual width value can not be taken as an indication of the remaining misalignment of the modules. If the alignment procedure works properly, the distribution of the residuals in each module should be centered at zero after alignment. This was verified inspecting the distribution of the median of the residuals of each module. The median was chosen as estimator of the position of the

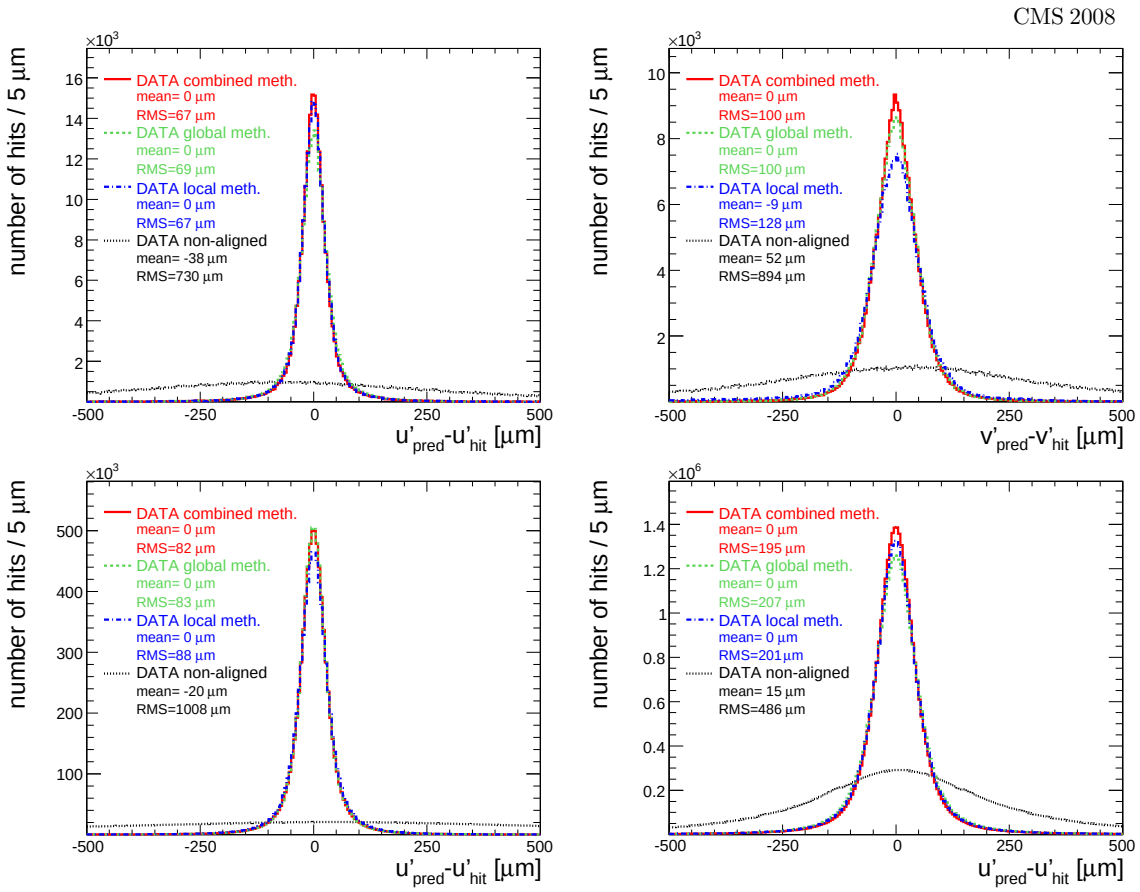

Figure 4.10: *Track residuals, shown for PXB (top left u', top right v'), TIB (bottom left), and TOB (bottom right). The four lines correspond to before alignment (dotted lines) and alignment with the global (dashed lines), local (dot-dashed lines) and, combined methods (solid lines).*

peak of the residuals as less sensitive to the outliers with respect to the mean and more robust than a gaussian fit when used on about 16 000 distributions. Therefore, the RMS value of the median distribution is taken as most appropriate measurement of remaining misalignment in each subdetector. Median distributions are shown in Figure 4.11 and the corresponding RMS values of these distributions are given in Table 4.2. Beside this, a Monte Carlo simulation is performed in order to disentangle the statistical precision of track based alignment from other random effects which can occur. The generation of a 3.5 million events has been done using ideal geometry and then reconstructed applying the module positions from combined

	non-aligned [μm]	global [μm]	local [μm]	combined [μm]	combined MC [μm]	ideal MC [μm]
PXB (u')	328.7	7.5	3.0	2.6	2.1	2.1
PXB (v')	274.1	6.9	13.4	4.0	2.5	2.4
PXE (u')	389.0	23.5	26.5	13.1	12.0	9.4
PXE (v')	385.8	20.0	23.9	13.9	11.6	9.3
TIB (u')	712.2	4.9	7.1	2.5	1.2	1.1
TOB (u')	168.6	5.7	3.5	2.6	1.4	1.1
TID (u')	295.0	7.0	6.9	3.3	2.4	1.6
TEC (u')	216.9	25.0	10.4	7.4	4.6	2.5

Table 4.2: *The RMS of the distribution of the median of the residuals (DMR) in the u' and v' local coordinates for modules with more than 30 hits. Four geometries are considered: those obtained with the three methods discussed in the text and the non-aligned geometry. Results from simulations based on the combined alignment and ideal geometries are shown for comparison.*

method, and survey values only for degrees of freedom not aligned in data. This procedure effectively models the situation of no alignment in data. On this scenario an alignment using the same combined method strategy used in data is performed, providing indication of the remaining statistical uncertainties left by the alignment procedure. The resulting DMRs are also shown in Figure 4.11 and the RMS values listed in Table 4.2. Also, for comparison, the distributions obtained from the ideal Monte Carlo simulation are presented in Figure 4.11.

Overall, there is significant improvement in the track reconstruction going from the geometry without any alignment, to the alignment using tracks with the local and the global method, and finally to the combined result. With respect to cosmic ray trajectories the module positions were determined to a precision of 3-4 μm RMS in the barrel and 3-14 μm RMS in the endcaps in the most sensitive coordinate. These values are in agreement with the expected statistical precision as determined using simulated events. They are also comparable to values obtained from a MC simulation based on the ideal detector geometry which is an indication that alignment precision is approaching to statistical limit.

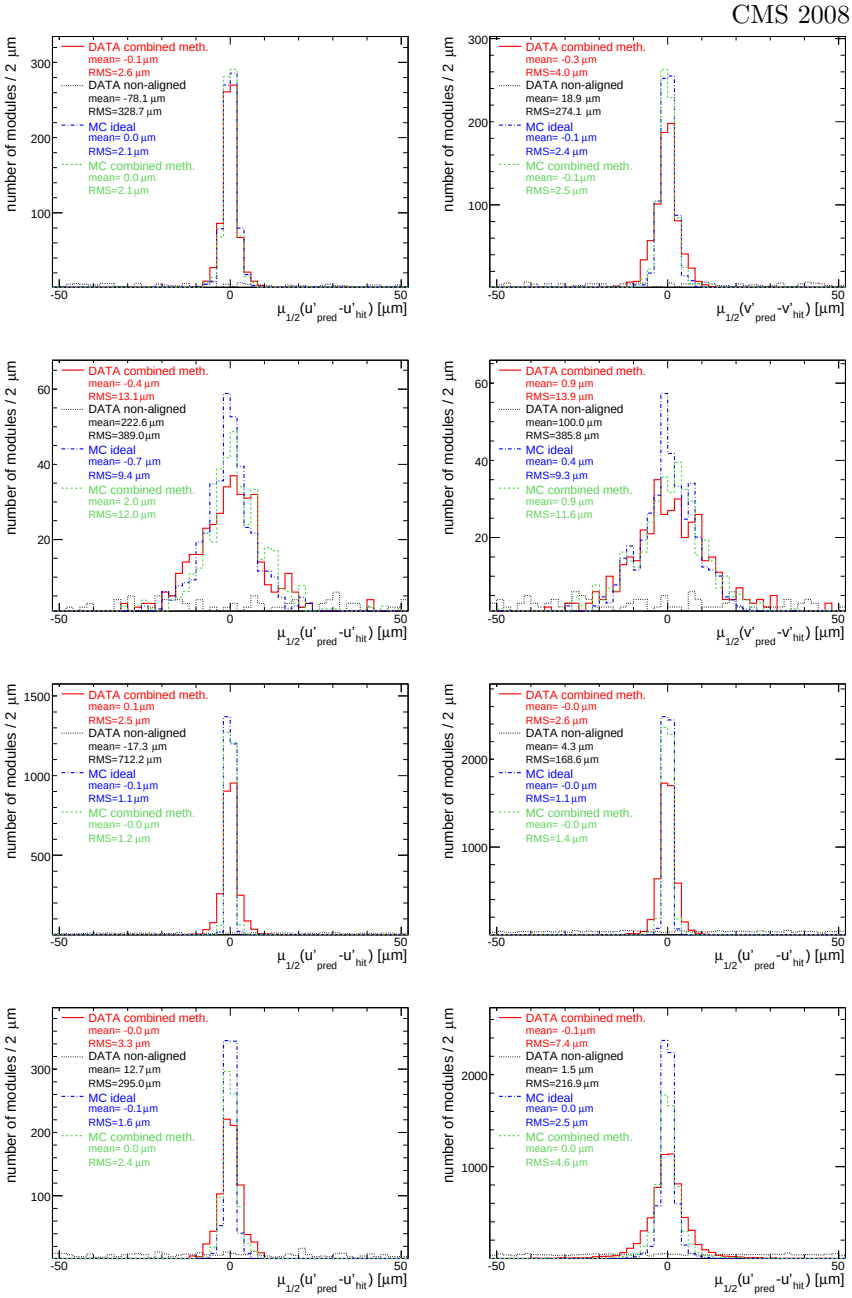

Figure 4.11: *Distribution of the median of the residuals for modules with more than 30 hits, shown for PXB (top left u', top right v'), PXE (second row left u', second row right v'), TIB (third row left), TOB (third row right), TID (bottom left), and TEC (bottom right). Curves are distributions before alignment (black dotted), after alignment with the combined method (red solid), combined method MC (green dashed), and ideal MC (blue dash-dotted).*

4.3.3 Monitoring of the geometry

Once the results from the alignment procedure have been tested on the tracking and reconstruction, a detailed analysis of the position of the modules inside the Tracker geometry is needed in order to spot evidence of internal shifts and rotation which can affect the reconstruction of physics observables. To test the consistency of the two methods, a comparison between the geometries from the local and the global methods module by module have been done, after correcting for an overall shift and rotation of the whole detector or sub-detector with respect to its center-of-gravity. For the BPIX modules, this test indicates an agreement between the two geometries of the order of 12 μm in the $r\phi$ plane.
Furthermore a comparison between the geometry obtained with the combined method, assumed to be the best geometry describing the Tracker, with respect to the design one was performed. This study indicates that the two BPIX half-barrels are shifted along the vertical axis by about 0.4 mm and the two half-barrels of the TIB have an extra separation along the$z$ axis of about 5 mm as visible in Figure 4.12. Both displacements are mechanically allowed and the large displacement of the TIB half-barrels is supported by the optical survey measurements described in [29].

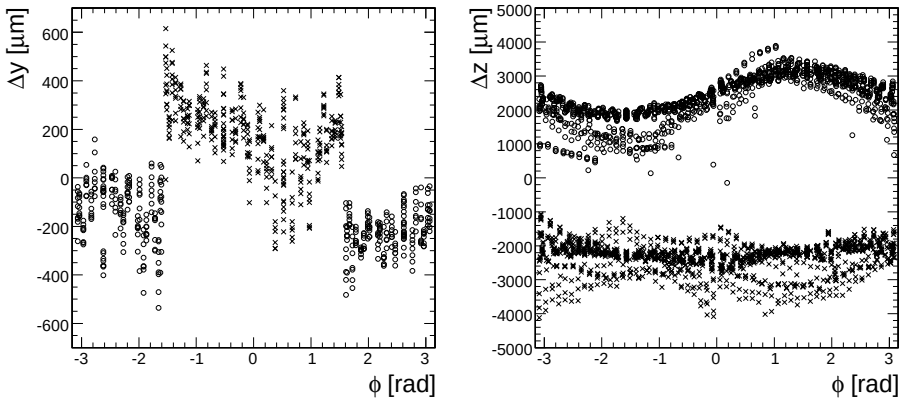

Figure 4.12: *Comparison of the positions of the modules in the combined method geometry with respect to the design one:* $(y_{design} - y_{comb})$ *for the BPIX modules (left) and* $(z_{design} - z_{comb})$ *for the TIB modules (right) as a function of* ϕ*. On the left crosses (circles) represent modules of the positive (negative)* x *BPIX half barrel, on the rigth positive (negative)* z *TIB half barrel.*

4.3.4 Monitoring of tracking performance

A check of the track parameter resolution after the alignment is done by mimicking the topology of collision tracks. A cosmic track traversing the detector close to the impact point is splitted at the point of closest approach to the nominal beamline in two halves which were independently reconstructed and refitted (Figure 4.13). Both the upper and lower legs were required to

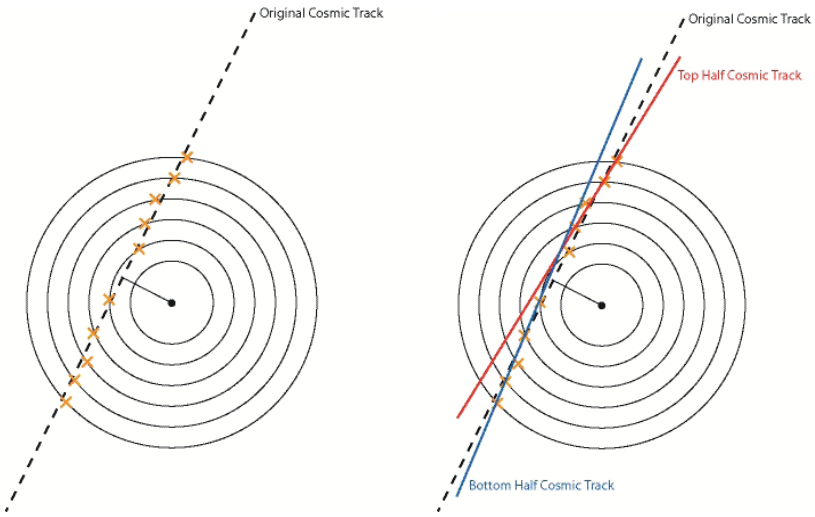

Figure 4.13: *Track splitted at its point of closest approach to the nominal beamline. The two halves belonging to the same one were independently reconstructed and refitted.*

have at least 3 pixel hits. Figure 4.14 shows the difference between upper and lower portions of tracks for the track distance of closest approach in the transverse direction d_{xy} and track curvature $1/p_T$: there is significant improvement due to Tracker alignment with good agreement between data and simulations. The results of the combined method are approaching those of a MC simulation with ideal detector geometry. The two track parameter shown are an example of the different dependences from the Tracker region: d_{xy} is more sensitive to the alignment of the pixel detector, while the p_T measurement is most sensitive to the strip part of the Tracker.

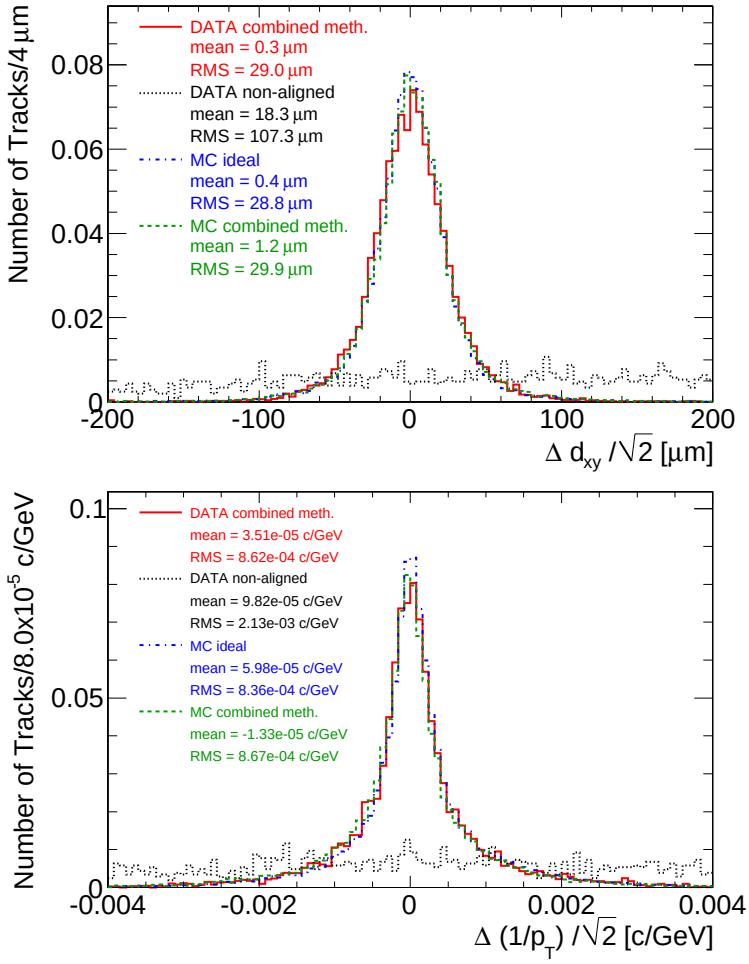

Figure 4.14: *Differences between the track parameters measured at the point of closest approach to the nominal beam-line, in the two halves of a cosmic track and scaled by $1/\sqrt{2}$. The distance of closest approach in the transverse direction d_{xy} (top) and $1/p_T$ (bottom) are shown. Four resulting geometries are reported: data non-aligned (black dotted lines), ideal Monte Carlo (blue dash-dot-dashed), and alignment result with cosmic ray data using combined method (red solid) and Monte Carlo (green dashed).*

4.4 Systematic misalignment studies using cosmic rays

A global translation and rotation of the whole Tracker is the simplest example of a transformation of the geometry that is χ^2-invariant. This transformation has no effects on the internal alignment and is easily resolved by imposing the center-of-gravity of all the modules to be coincident with the design position. In the reality there are several non-trivial transformations (weak modes) which can affect the geometry of the Tracker, and can survive even after the track based alignment, if not adequately constrained. If uncorrected, they would produce unacceptable systematic biases in physics measurements. For instance, an uncorrected systematic rotation of the layers of the Tracker would introduce an artificial charge-dependent momentum asymmetry to reconstructed tracks, given the use of magnetic bending to define the charge and transverse momentum of a track. Likewise, a radial expansion or compression or z-scale distortion would systematically change the measured distance scale of the detector, distorting lifetime measurements.
During CRAFT, only cosmic tracks were available for alignment: only with collision tracks, most of these systematic deformations will be eventually recovered, imposing vertex constraints or using correlation between different part of the detector.
Following the analysis described in [26], nine systematic distorsions, modeled for a cylindrical geometry, have been considered, in Δr, $\Delta\phi$, and Δz as a function of r, ϕ, and z. The introduction of these deformations on top of an aligned geometry and the consequent re-alignment allows to spot the presence of possible weak modes in the geometry which was not possible to solve with the current alignment procedure and track samples available. For this study the geometry obtained with the global method was assumed as starting point, since it is the method most sensitive to the global deformations. Compatible results have been obtained using the local method strategy. Due to the large computational time needed, was not possible to perform the study with the strategy of the combined method, which in the end was found to be the best way to perform alignment using cosmic rays.
The study consisted of the following steps:

- the position of each module of the geometry obtained with global method was changed according to the nine modes reported in Table 4.3. Figure 4.15 gives a synoptical view of each module position after applying the nine distorsions with respect to the starting aligned geometry. In order to provide a sensible comparison, the centre of both geometries is the Tracker centre of gravity, meaning that only overall translations and rotations were subtracted from both objects.

- the systematically misaligned geometries were used as a starting point

and the alignment procedure described in Section 4.2.1 was repeated using the same 3.2 million of cosmic tracks used for the alignment. All the three steps of the alignment strategy were applied, even if the main correction to the distorsion is expected to come from the first step. In fact this step computes the position of the highest level structures and modules together, correlating local movements with the global ones.

- the nine geometries obtained after the alignments were then compared, module by module, to the original aligned geometry, in order to verify if the distortions were recovered by the alignment procedure.

	Δr	Δz	$r\Delta\phi$
vs. r formula max value (mm)	radial $\Delta r = c_1 r$ 0.6	telescope $\Delta z = c_1 r$ 0.3	curl $\Delta\phi = c_1 + c_2 r$ 0.3
vs. z formula max value (mm)	bowing $\Delta r = c_1 + c_2 z$ 0.6	z-deformation $\Delta z = c_1 z$ 3	twist $\Delta\phi = c_1 z$ 1.5
vs. ϕ formula max value (mm)	elliptical $\Delta r = r(1 - c_1 \cos 2\phi)$ 0.6	skew $\Delta z = c_1 \cos\phi$ 6	sagitta $r\Delta\phi = c_1 \cos\phi$ 0.15

Table 4.3: *Definition, formula and size of the nine systematic distorsions (modes) used for study the impact on the geometry obtained using CRAFT cosmic tracks.*

The results were analyzed separately for the pixels (BPIX and FPIX), barrel strip (TIB and TOB), and forward strip (TID and TEC) sub-detectors. Different results are found, also due to the non-uniform modules illumination provided by cosmic tracks, which is maximal in the barrel region.

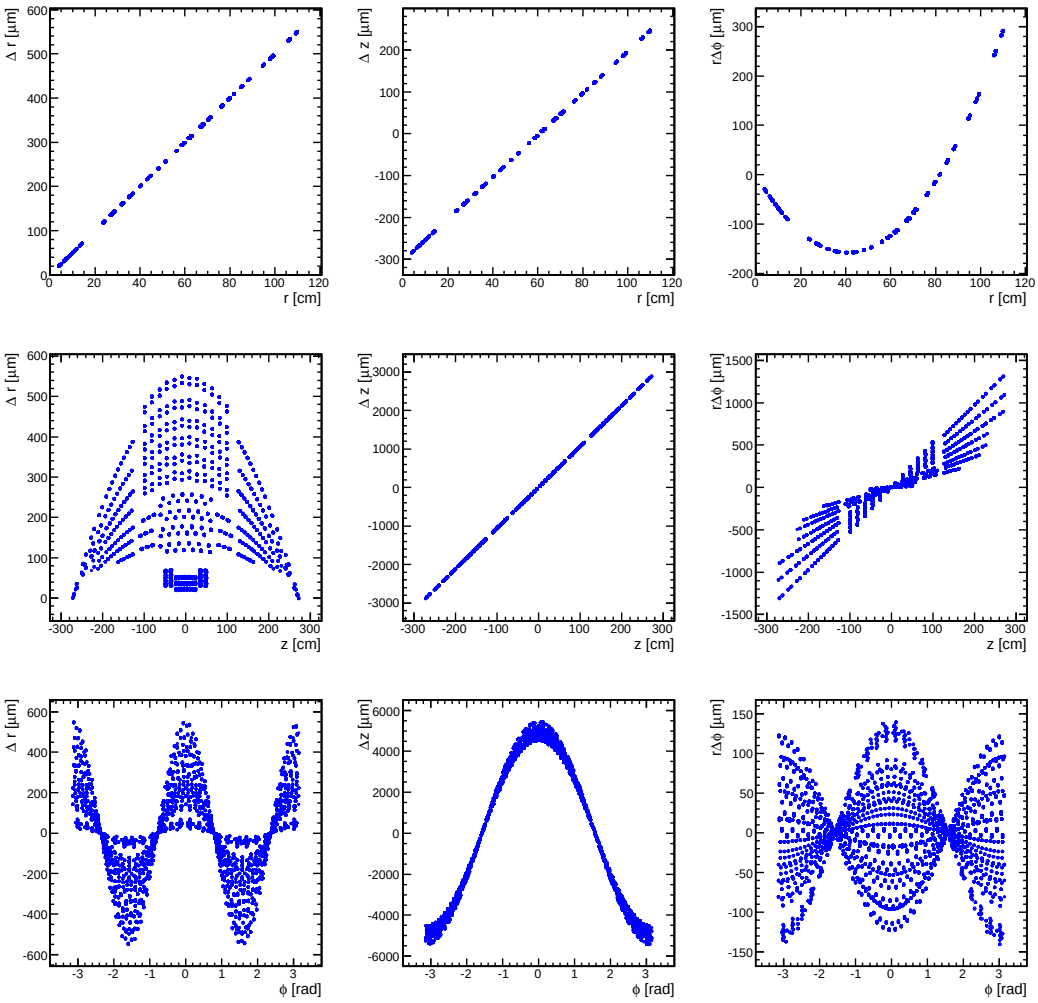

Figure 4.15: *Visualization of the nine investigated systematic distorsion for Tracker modules. On the vertical, deviations of the modules with respect to the aligned geometry with global method along r (first column), z (second column) and $r\Delta\phi$ (third column). On the horizontal, the position of the modules in cylindrical coordinates r (first row), z (second row) and ϕ (third row).*

As illustration, the elliptical mode is shown in Figure 4.16: the radial shifts of the modules with respect to the starting geometry are shown once the systematic distorsion was applied and after the re-alignment procedure. For distorsion perfectly recovered, the figure should appear as a flat band of point around zero, indicating that the deviations are null. In the barrel region the modules are not exactly shifted back to their original position, but the entity of the deformation is noticeably reduced, although a final modulation in the structure is still present. The situation is completely different for the endcap region where cosmic rays impact almost parallel to the modules surface and alignment procedure is almost unsensitive to the global deformation of the structure.

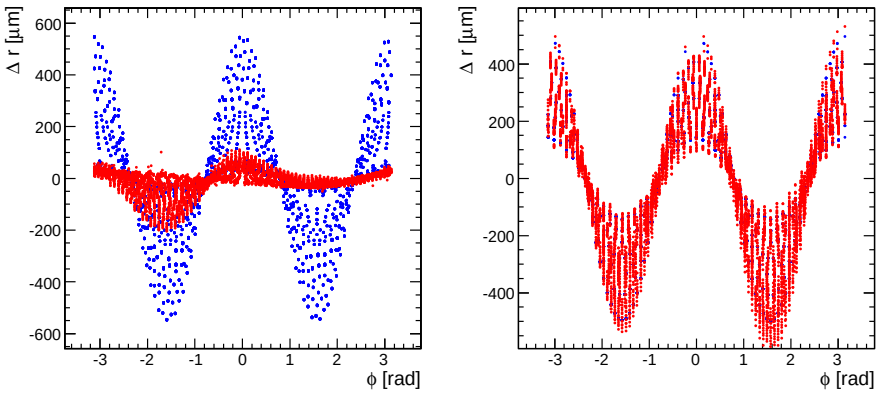

Figure 4.16: *Systematic elliptical distorsion of the Tracker volume applied in the barrel (TIB and TOB, left plot) and in the Endcap (TEC and TID, right plot) region. Blue points are the modules position after the applied systematic misalignment, red points are the situation after the re-alignment. Both sets represent the deviations with respect to the starting geometry.*

Therefore, in the following figures only modules belonging TIB and TOB have been considered.
An overview of four out of the nine systematic distorsions and of their remaining impact on the Tracker geometry after re-alignment is given in Figure 4.17. These four modes are representative of the detecting power of the possible hidden systematic distorsions given the available track topology and the adopted alignment strategy. Beside the geometry comparison illustrating the modules shift with respect to starting geometry, a clear effect deriving from the application of a misalignment and of a potential recovery, is given by the χ^2/ndf behavior of the reconstructed tracks.

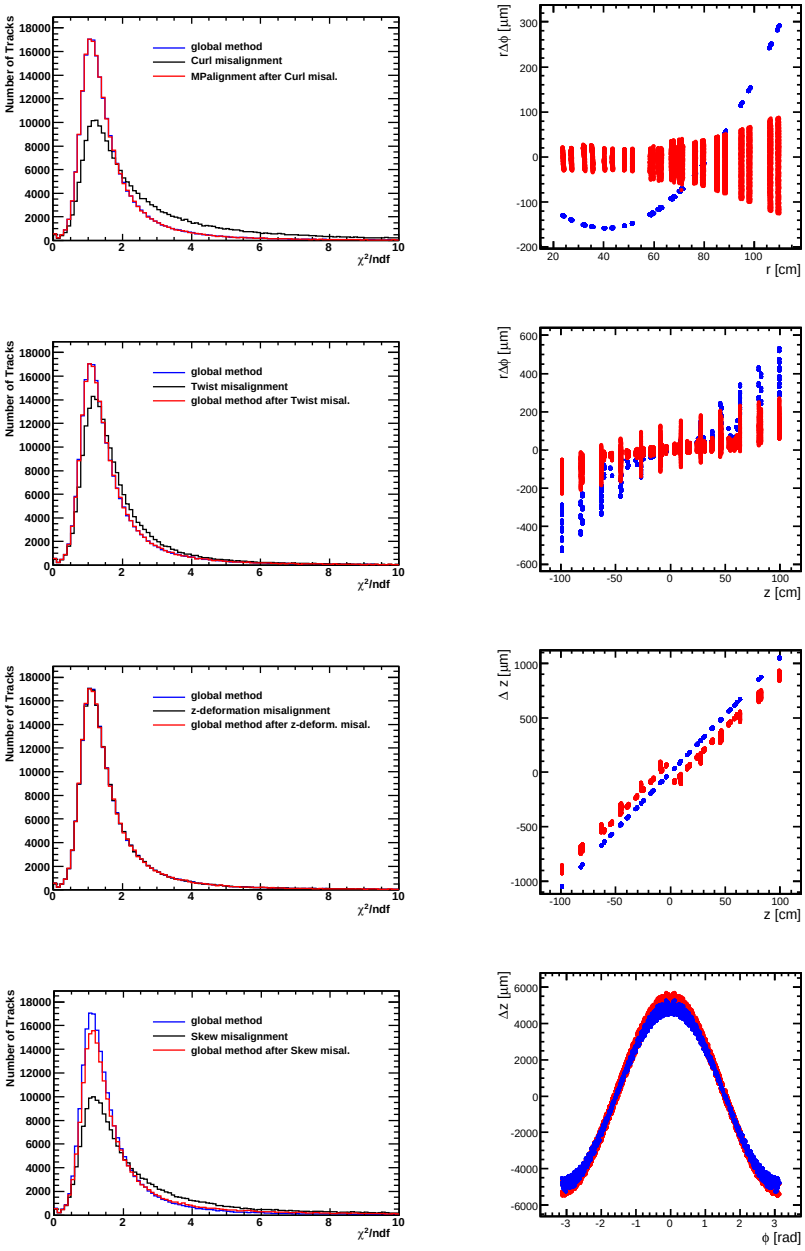

Figure 4.17: *Left column.* χ^2/ndf *of the reconstructed tracks with different geometries, aligned with global method (blue line), misaligned with the systematic mode (black line), re-aligned with the global method on top of the misalignment (red line). Right column. Deviations of the modules with respect to the starting aligned geometry after the applied systematic misalignment (blue points) and after the alignment on top of it (red points). From top to bottom, four different modes are reported: curl, twist, z-deformation and skew.*

It is evident that the curl ($\Delta\phi = c_1 + c_2 r$) can be recovered through alignment with cosmic ray tracks. This is confirmed by the χ^2/ndf trend, being sensible to misalignment along the $r\phi$ direction. It is visible how from the initial aligned geometry the performance become worse after the introduction of the curl distorsion, but are promptly recovered after the re-alignment. The twist deformation ($\Delta\phi = c_1 z$) is partially recovered in TIB and not in TOB. The χ^2/ndf is mainly dominated by alignment quality in TIB rather than in TOB and this partially explains how performance are recovered after re-alignment.
Conversely, the two deformations affecting Δz, z-deformation ($\Delta z = c_1 z$), and skew ($\Delta z = c_1 \cos\phi$) are almost not recovered. For z-deformation is well visible how the movement of the modules along global z direction applied with the systematic misalignment do not affect the χ^2 distribution. This is somehow expected, since the residuals are computed in the transverse $r\phi$ plane which is the sensitive coordinate for the measurement, leading z-deformation to be really a "weak" mode for alignment.
In general, it should be noticed that the capability to recover the systematic misalignment is also dependent by the entity of the deformation applied: for the skew mode the deformation is pretty huge, up to 6 mm. A study aimed at the tuning of values on a more realistic scale according to the effects observed on the data, would give more precise results. Therefore results obtained here should be considered mainly as qualitative.
Figure 4.18 shows as the application of subsequent steps of the global method alignment procedure solve the four considered modes. For the curl and the twist the first step is the most relevant in recovering most of the deformation. Here highest level structures (half-barrels, endcaps, layers and disks) in all six degrees of freedom together with all module units were aligned: this was found to give a consistent contribution in preventing global structure deformation, and thus, for this case, in correcting them. The second step minimizes the module spread in the case of twist, while it increases for the curl mode especially at small radius (TIB): here TIB modules were left free to move in more degrees of freedom (rotations included) and the type of $r\Delta\phi$ deformation introduced by the curl could drive the minimization process towards other solutions. With the third step situation is re-established. For the two deformations affecting z coordinate it is evident that, at any step of the alignment, the positions of the modules are not varying with the iterations: for the z-deformation there is also a separation of the two half barrels along z, which is propagated until last step.
Finally, even for systematic distorsions which are recovered, a non zero spread of the modules with respect the starting geometry is observed anyway. Part of this is due to the remaining global movement of the highest level structures (like layers and half-barrels), which are not subtracted in the geometry comparison plots shown. The other part has to be assigned to the intrinsic spread of the alignment procedure itself plus some not corrected

misalignment effects. In order to disentangle the two contributions, Figure 4.19 shows the comparison of the TIB and TOB module positions, along $r\phi$ direction, between the initial global method geometry, used as starting point for the systematic misalignment studies and three different geometries:

- the first is the geometry after introducing the systematic distorsion, which is, as expected, quite spread according to the scale of misalignment applied.
- the second is the geometry after the re-alignment, with all the three steps of the global method without any global movement subtraction, but the overall Tracker rotations and translations. The remaining distribution is less spread and it is peaked at zero, as expected after alignment procedure.
- the third one is the same as the second geometry, but with the subtraction of coherent movements of the highest level structures, which leads to a visible narrowing of the distribution. This last remaining spread gives an indication of the intrinsic spread to the alignment procedure itself in addition to other possible remaining effects that the algorithm has not been able to correct.

Further studies regarding other systematic misalignment Tracker modes are reported in Appendix B, but in general subtle deformations, including those discussed above, may be difficult to recover with cosmic tracks alone.
Only tracks from LHC beam interactions, which should be uniform in ϕ, and with additional constraints such as on a vertex or the mass of a resonance, will provide better sensitivity to those systematic deformations.

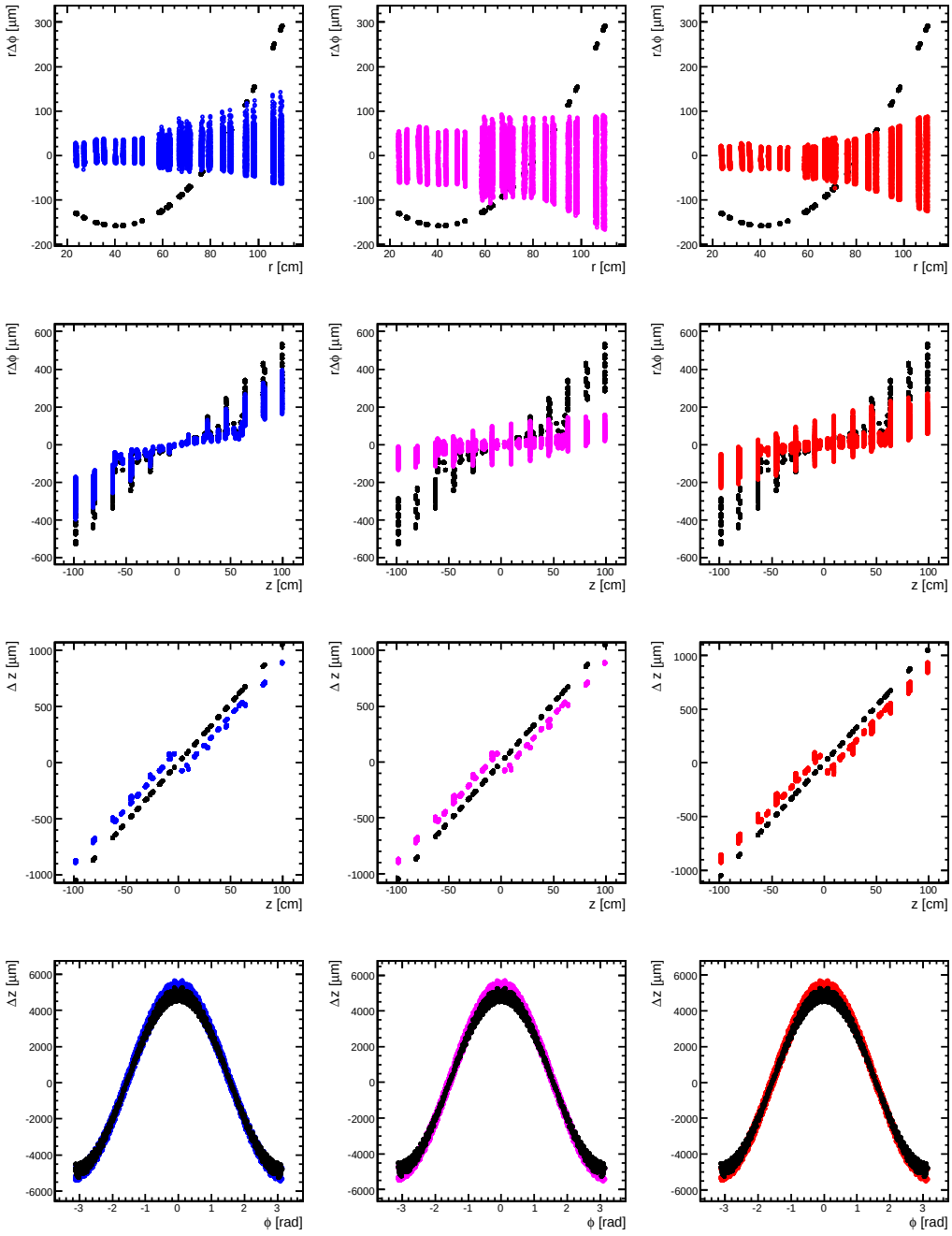

Figure 4.18: *From top to bottom curl, twist, z-deformation and skew mode. Deviations of the modules with respect to the initial global method geometry after the applied systematic misalignment (black points) are reported in each of the plot, for reference. In addition, first , second and third column shows the difference in the module positions with respect to initial geometry after the first, second, third step of the global method on top of the misalignment.*

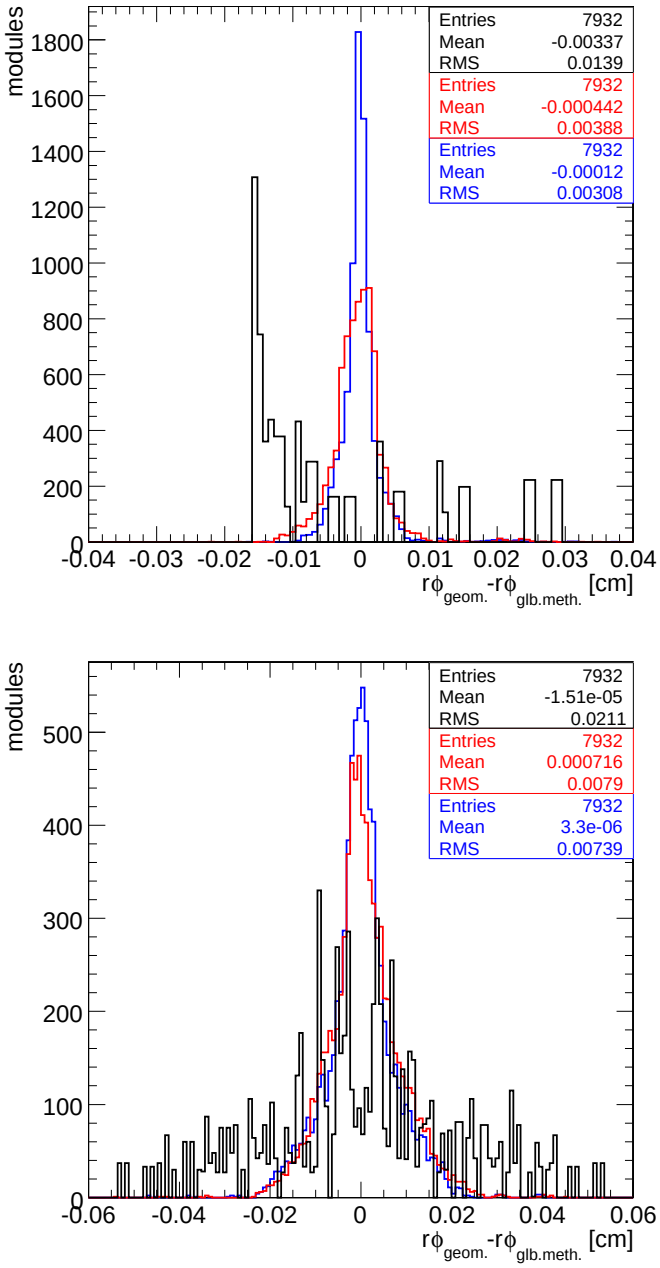

Figure 4.19: *Differences with respect to the initial global method geometry for TIB and TOB modules along the $r\phi$ coordinate. The systematic misaligned geometry is associated to the black line, geometry after the re-alignment to the red line and geometry after the re-alignment, but with the subtraction of coherent movements of the highest level structures, to the blue line. Top plot refers to the curl mode, while in the bottom one the twist mode is shown.*

Chapter 5

Impact of alignment on the momentum scale of muons

A remaining misplacement in the position and orientation of the sensors in a detector has a remarkable impact on the track reconstruction of charged particles and finally in the measurement of the cross section of a physics process. Studies on the systematic uncertainties on the Z boson cross section measurement [39] assess an effect of the 3 % due to the Tracker misalignment. For this reason is important to evaluate the entity of this systematic uncertainty and, if possible, correct for the remaining effects.

5.1 Misalignment scenarios for early physics processes

To study the impact of Tracker misalignment on track and vertex reconstruction in physics analysis, models of misalignment (in the following called *scenario*) have been implemented in the standard CMS reconstruction software. The application of a scenario on top of the detector geometry assumed for the reconstruction allows to determine biases and deterioration of the resolution of the reconstructed physics observables, like invariant mass or transverse momentum. Historically, different misalignment scenarios were produced to model the knowledge of the Tracker geometry at different stages of the data taking. Based on the results obtained with CRAFT data, the so called *Startup* scenario was updated. Rather than implementing the misalignment effects at the generation level in the study of a simulated physics process, the adopted philosophy in CMS is to introduce the displacement of detector modules directly at the reconstruction level. Thus, the usual production chain is to generate with the design geometry the physics events and then apply the shifts of the detector modules during the reconstruction process. Since the shifts expected in the real detector are small, due to the mechanical constraints which do not allow for drastic movements, this is

equivalent to generate the simulated process with the misaligned geometry and then to reconstruct them with the design geometry. This last approach would be less convenient from the computational time point of view, since both generation and reconstruction are required each time a new scenario is applied, instead of reconstruction only.

5.1.1 The CMS official misalignment scenarios

A set of scenarios corresponding to approximately $10\,pb^{-1}$, $100\,pb^{-1}$ and $1000\,pb^{-1}$ of collected luminosity were implemented. Two additional scenarios, the *SurveyLASonly* and the *SurveyLASCosmics*, were developed to estimate alignment status before collisions. These scenarios have been considered to study of early performance of CMS and also for Computing, Software and Analysis Challenge of 2008 [28]. The idea of the scenarios is to reflect the residual misalignment in the following situations:

- input from assembly measurements, survey and Laser Alignment System (*SurveyLASonly* scenario)
- alignment studies with cosmic muons (*SurveyLASCosmics* scenario)
- track based alignment with collision events with high cross section, mainly minimum bias events and low mass resonances ($10\,pb^{-1}$ scenario)
- track based alignment with a limited sample of the most useful collision events, including muons from Z and W ($100\,pb^{-1}$ scenario)
- track based alignment with above mentioned physics events in addition to several kinds of collision events ($1000\,pb^{-1}$ scenario)

Random misalignments of the same size are applied to modules in all the three spatial directions and similarly to the three angles for almost all the hierarchical level of the Tracker substructures (see Figure 3.2). The distribution of the applied smearing can be gaussian or uniform with a spread defined according to the alignment precision reached in the situations listed above. The impact of these misalignment scenarios on physics [32], evaluated in terms of effects on track parameter resolution and on the reconstruction of resonances (like $Z \rightarrow \mu^+ \mu^-$), are shown in Figure 5.1. It should be pointed out that the scenarios presented here do not simulate the χ^2 invariant deformation of the geometry, which will be an important part in the evaluation of residual misalignment.

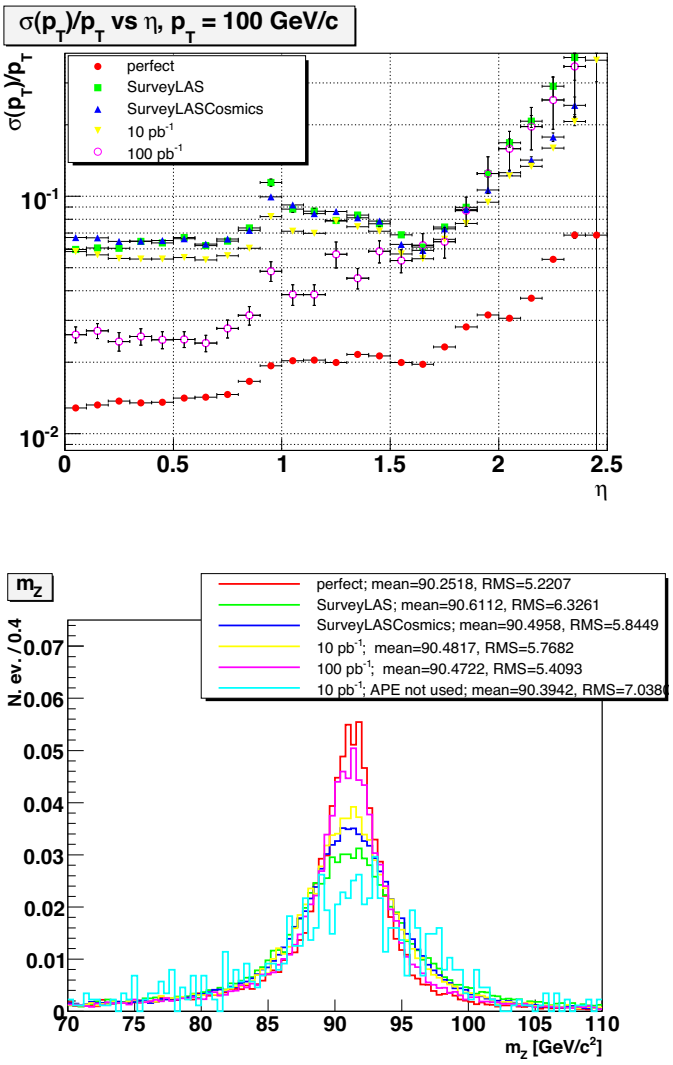

Figure 5.1: *Top figure. Muon p_T resolution as a function of η for the ideal alignment and for the official misalignment scenarios produced using single muon generator ("particle gun") for p_T= 100 GeV muons: in the ideal case resolution is* 1.5-2.0 % *in the barrel region and deteriorates to* 8-10 % *and* 5-8 % *with SurveyLASCosmics and* $10\,pb^{-1}$ *scenario respectively. Bottom figure. Di-muons invariant mass for perfect alignment and for the official misalignment scenarios: the effect of misalignment is to shift the Z peak up to* 12 % *and to worsen resolution up to* 90 % *with respect to the ideal case using the worst case of SurveyLASCosmics [32].*

5.1.2 The CRAFT-based misalignment scenarios

As described in Chapter 4, during the October-November 2008 CRAFT data taking, the alignment of the CMS Tracker and Muon system reached a remarkable level of precision. For the Tracker, the remaining average displacement of the modules with respect to cosmic tracks was estimated to be of the order of 3-4 μm in the central region and 3-14 μm for the modules placed in the endcaps. These results have been translated in terms of misalignment scenarios reflecting the current level of knowledge on the module position inside the geometry, to be used as a starting point for Monte Carlo studies of the early physics processes. Actually two Tracker misalignment scenario have been released after the CRAFT experience, obtained at different stages of the analysis, and reflecting different approaches in the implementation, both describing the remaining misalignment expected at the startup.

The *Startup* scenario

For the Tracker system, this scenario was obtained after the very first analysis of the CRAFT data and was implemented by mixing the *SurveyLASonly*, $10\,pb^{-1}$ and $100\,pb^{-1}$ scenarios. Therefore it is based on diced misalignment of the alignable objects at the different hierarchy levels, driven by the distribution of the residuals observed in the data: a precision level equivalent to what expected after $100\,pb^{-1}$ is used in TIB and TOB, $10\,pb^{-1}$ for the TID and TEC and BPIX, while level of precision of *SurveyLASonly* scenario has been found in the FPIX detector, as the poor statistic collected in this subdetector (due to the distribution of the cosmic rays) did not allow for a better alignment of its modules. Furthermore, a set of consistent APE was associated to the geometry in the Tracker. Values were tuned according residual distribution and were constant for all modules within the same subdetector: 100 μm for the best aligned subdetectors (TIB and TOB), 300 μm for endcap modules (TID and TEC), 200 μm in BPIX and 1 mm in FPIX. Also for the muon system the scenario was based on CRAFT. Positions and orientations of muon chambers were randomly generated from Gaussian distributions whose standard deviations were derived from a combination of data-based validation techniques and an alignment on a cosmic rays Monte Carlo simulation. Chambers that could not be aligned due to poor statistics (such as sectors 1 and 7, and wheels ± 2) were assumed to have the same misalignment distribution as the aligned chambers before their alignment. The endcap misalignment was constructed from uncertainties in hardware alignment and photogrammetry. Simple layer misalignments of the DTs and CSCs were also included, and are all derived from data.

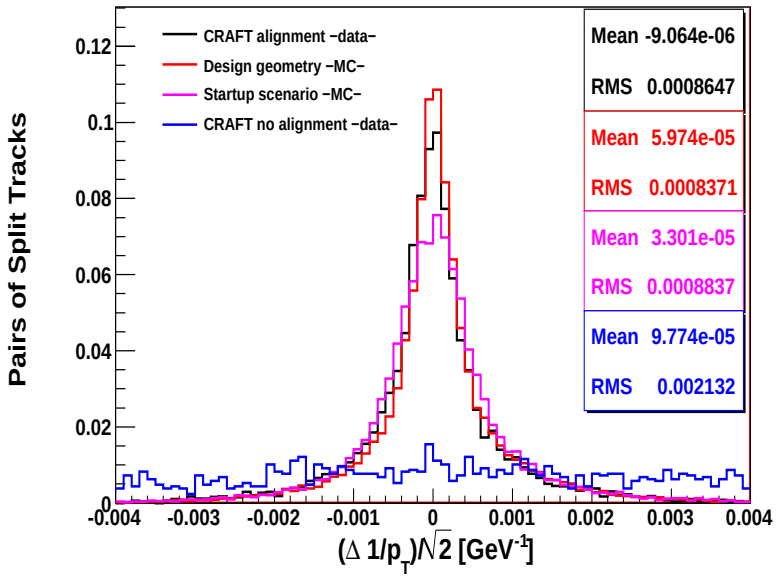

Figure 5.2: *p_T resolution obtained with track splitting method for Startup misalignment scenario (pink line) compared with the resolution obtained on data before (blue line) and after CRAFT alignment (black line). For reference also design geometry (red line) is shown. Startup scenario is still conservative with respect to the performance on data.*

The *Realistic* scenario

For the Tracker, this scenario was obtained by performing an alignment on a Monte Carlo sample of cosmics events generated with design geometry, and using the geometry obtained on CRAFT data as starting point for the reconstruction. The same strategy and track selection applied on the data were used. Therefore no random numbers were introduced for obtaining this scenario. The final geometry is somewhat optimistic since along the degrees of freedom not aligned in data the modules stay in their known design position. On the other hand the geometry could contain global movements and distorsions, inherited from starting CRAFT geometry, which could not be easily detected by using only the cosmic track topology. Therefore this scenario represents in a more realistic way the real displacement of the modules inside the geometry not corrected. The same APE determined on the data were adopted. For the muon system the scenario was kept the same as in the *Startup* case.

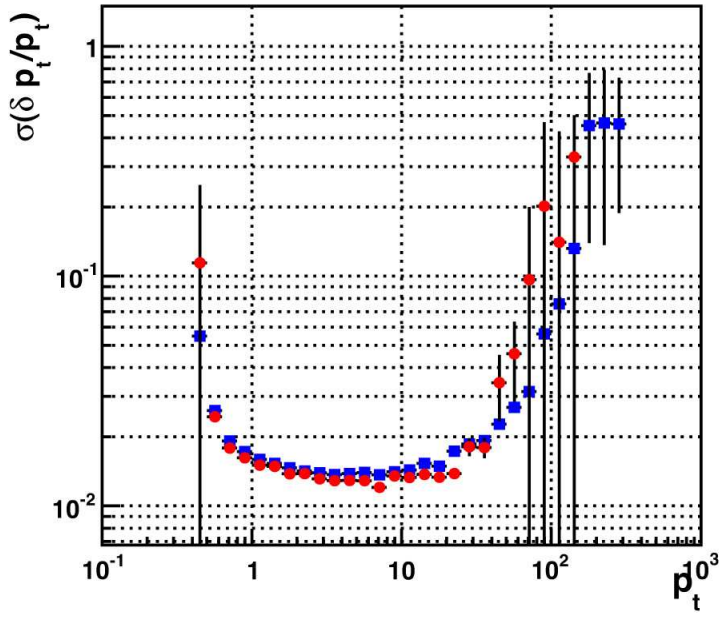

Figure 5.3: *p_T resolution as a function of p_T for Realistic (red points) and Startup (blue points) scenario plotted on a logarithmic scale. Performance are similar, even that Realistic performs a little better until $p_T = 40\,\mathrm{GeV}$.*

5.2 Impact of misalignment on the calibration of muon momentum scale

The CMS detector is designed to provide a reliable identification of tracks from $p\,p$ collisions and a precise measurement of their momentum in the solenoidal magnetic field. The momentum measurement of charged tracks is affected by systematic uncertainties due to the imperfect knowledge and modeling of the magnetic field, the sub-detectors alignment, the detector material, and the reconstruction algorithms used to fit the track trajectory. All these effects, if properly detected and quantified can be absorbed by properly modeling a *scale* factor for the momentum, which should be dependent on the measured muon kinematic variables (η, ϕ and p_T) [37].
An accurate calibration of momentum scale is essential in order to perform first accessible precision measurements, like top quark and W boson masses, B hadron spectroscopy, and a set of other early measurements. This calibration is feasible by the availability of reconstructed resonance decays, typically those involving two-body decays of neutral particles.
All particles with an easy detectable decay to muon pairs were considered:

the J/ψ, the $\psi(2S)$, the three Υ states, and the Z boson[1]. The reference

	Mass	Γ
J/ψ	3096.916 ± 0.011 MeV	93.2 ± 2.1 keV
$\psi(2S)$	3686.09 ± 0.04 MeV	317 ± 9 keV
$\Upsilon(1S)$	9460.30 ± 0.26 MeV	54.02 ± 1.25 keV
$\Upsilon(2S)$	10.02326 ± 0.00031 GeV	31.98 ± 2.63 keV
$\Upsilon(3S)$	10.3552 ± 0.0005 GeV	20.32 ± 1.85 keV
Z	91.188 ± 0.002 GeV	2.495 ± 0.002 GeV

	$\sigma_{pp\to X}(nb)$	$B(X \to \mu^+\mu^-)$	evt /10 pb^{-1}
J/ψ	2145.0	$(5.93 \pm 0.06)\%$	1 272 000
$\psi(2S)$	289.2	$(7.5 \pm 0.8) \times 10^{-3}$	21 690
$\Upsilon(1S)$	560.5	$(2.48 \pm 0.05)\%$	139 000
$\Upsilon(2S)$	328.0	$(1.93 \pm 0.17)\%$	63 300
$\Upsilon(3S)$	81.7	$(2.18 \pm 0.21)\%$	17 800
Z	67.6	$(3.366 \pm 0.007)\%$	22 740

Table 5.1: *Cross sections, branching ratios to muon pairs and dimuon yields per* 10 pb^{-1} *in 10 TeV pp collisions for dimuon resonances (derived from PYTHIA [40]).*

quantity which provides sensitivity on an event-by-event basis to the possible biases on the reconstructed muon track parameters is, of course, the parent's invariant mass. This is not a per-track variable, so a probabilistic approach is necessary in order to relate the difference between expected and observed mass with an hypothetical bias on the measured parameters of either or both daughter tracks. Once a set of functions describing the dependence on track kinematics of the biases and of the measurement resolutions is established, the best estimate of the parameters of those functions can be determined from a likelihood minimization, provided that a sufficient set of homogeneous data is used.
In Sections 5.2.3 and 5.2.4 particular emphasis will be given to the study of the impact of the application of CRAFT based scenarios on the Z and Υ resonances. The misalignment effects introduced are properly detected and momentum scale and resolution are calibrated with the method described in the next Section using simulated statistics collected after $\int \mathcal{L}\, dt = 10\, pb^{-1}$. The study was limited to the evaluation of the impact on the resonance mass resolution of different misalignment scenarios, trying to model the detector conditions in the reality. An extension, after a proper inclusion of the backgrounds, aimed to study the impact on the acceptance of muon selection

[1]Decays to charged hadrons of other narrow resonances (such as $K^\circ_S \to \pi^+\pi^-$, $\Lambda \to p\pi$, $\phi \to K^+K^-$, or even fully-reconstructed B or D hadrons) may also be exploited for the calibration of the track momentum using Tracker only.

could be easily performed, leading also to an evaluation of the systematics effects on the resonances cross section measurement, but this is out of the scope of this work.

5.2.1 The *MuScle fit* algorithm

The algorithm approach is conceived to correct the muon momentum measurement and to determine its resolution, and it is based on a multidimensional likelihood fit that uses as input the decay to muon pairs of Z bosons, as well as J/ψ, $\psi(2S)$, and Υ resonances [38]. The dimuon invariant mass depends linearly on the scale of the momentum of the muons. Therefore it is possible to determine the momentum scale by studying the average difference between the reconstructed dimuon mass and the nominal resonance mass as a function of each muon kinematic variable. These studies may provide evidence for misalignment and other problems in the reconstruction.
An unbinned likelihood technique has been developed which uses ansatz functions for correcting the muon momentum (p'_T) and for the estimation of muon resolution (σ_i):

$$p'_T = F(\vec{\mathbf{x}}; \vec{\mathbf{a}})\, p_T \tag{5.1}$$

$$\sigma_i = G_i(\vec{\mathbf{x}}; \vec{\mathbf{b}}) \tag{5.2}$$

The muon kinematic variables are $\vec{\mathbf{x}} = (p_T, \eta, \phi)$, the elements of the vectors $\vec{\mathbf{a}}$ and $\vec{\mathbf{b}}$ are the parameters to be computed by the likelihood fit, and σ_i are the resolutions of each muon kinematic variables.
The algorithm is based on minimization of a likelihood function where the probability density function (P) describing the resonance is the convolution of a non relativistic Breit-Wigner with a Gaussian, which takes into account the dimuon mass resolution, plus an ansatz function for the background (B):

$$P = \int \frac{1}{\pi} \frac{\Gamma/2}{(M - M_{ref})^2 + (\Gamma/2)^2} \times \frac{1}{\sigma\sqrt{2\pi}} e^{-\frac{(M-M')}{2\sigma^2}} dM + B(\vec{\mathbf{x}}; \vec{\mathbf{c}}) \tag{5.3}$$

The dimuon mass M' is computed event by event using the corrected transverse momentum p'_T of Equation 5.1. The reference parameters for the mass (M_{ref}) and the width (Γ) in the Breit-Wigner are taken from the fit of the MC generated di-muon mass. The Gaussian is centered in M' and the standard deviation σ is the resolution of the di-muon mass and it is computed from the ansatz functions for σ_η, σ_ϕ, and σ_{pT}/p_T of Equation 5.2. The likelihood minimization returns the most likely value of the parameters a_j, b_j and c_j, which describe the muon momentum corrections, the muon momentum resolution and the di-muon background, given the observed distribution of

the reconstructed di-muon mass in the sample. The fit to the parameters can be repeated to check its stability and the algorithm even allows to perform a multi-resonance fitting, taking into account more than one resonance together and the background.

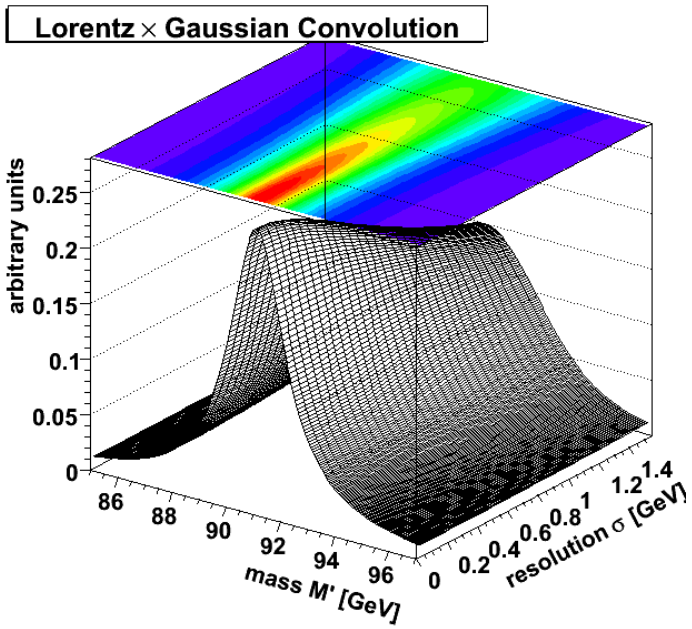

Figure 5.4: Probability density function for Z boson mass.

Meaningful ansatz function (F and G) for the momentum corrections and resolution must be chosen. This can be done on the basis of a preliminary study of the mass values and the muon momentum resolution as a function of the muon kinematic variables $\vec{\mathbf{x}}$. The uncertainty of the fitted parameters, their convergence and stability over several iterations give indications on the correctness of the chosen ansatz functions.

5.2.2 A test of *MuScle fit* using $\Upsilon \to \mu\mu$ decay reconstructed with systematic misalignment

As a check of the algorithm capability of recovering biases, a systematic elliptical distorsion ($\Delta r = r(1 - c_1 \cos 2\phi)$) of the Tracker has been introduced in the reconstruction of a generated 26 000 $\Upsilon \to \mu\mu$ sample. This distorsion was described in the Section 4.4 and leads to a deformation of the Tracker transverse section from a circular to an elliptical shape. This deformation is expected to have a strong impact on the reconstruction momentum of the muons coming from the Υ resonance decay and consequently to produce a worsening of the mass resolution or even a shift of the reconstructed mass peak.

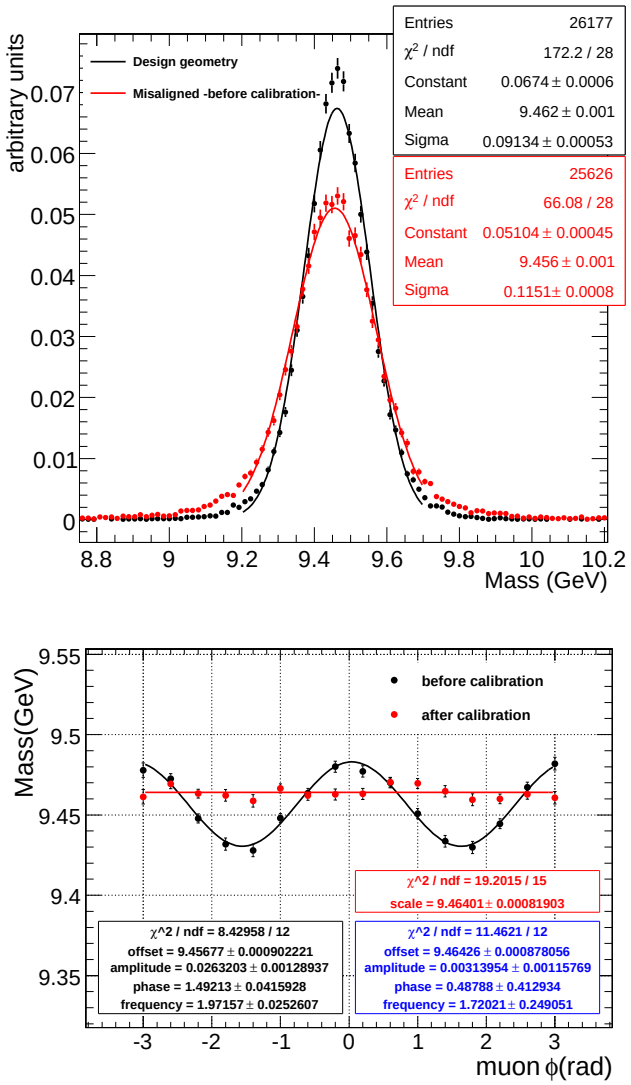

Figure 5.5: *Top plot. Reconstructed* Υ *mass before (black) and after (red) the introduction of a systematic elliptical misalignment for the Tracker modules. The distorted geometry produces a shift of the peak of the reconstructed resonance and a worsening in the resolution. Results of gaussian fits in the range [9.2,9.7] GeV are shown in the plot. Bottom plot. Recovering of a sinusoidal bias in azimuth using* Υ *events: average* Υ *mass as a function of muon* ϕ *(shown only for positive charged muons), computed before (black) and after (red) the muon momentum scale calibration. In the plots the parameters of both a linear (red box) and sinusoidal (blue box) fit after calibration are reported. Only the linear one is drawn.*

The scale of the applied distorsion has been enlarged with respect to the real scale of the misalignment expected in the detector, with the only intent to test the power of the algorithm in correcting such a huge bias. The Figure 5.5 shows the effect of the distorsion on the reconstructed Υ mass: peak of the resonance is shifted and resolution worsens, as expected. After having analyzed the dependence of the reconstructed mass from the muon kinematic variables, an ansatz function for the scale correction is build, containing a dependence from the ϕ of the muon, being the sinusoidal mass dependence quite evident:

$$p'_T = F(\phi, \eta)p_T = (a_0 + a_1 sin(a_2\phi + a_3) + a_4|\eta| + a_5\eta^2)p_T. \qquad (5.4)$$

A profile of the Υ mass before and after the correction as a function of the muon azimuthal angle ϕ is shown in Figure 5.5. The ansatz function provided as input for the fit is able to recover the sinusoidal shape, leading to a correct reconstruction of the final dimuon mass in the different detector regions. In general the exercise shows that even the effect of a huge bias in the muon momentum scale, due to remaining systematic distorsion in the geometry, can be corrected by the fit, provided that a suitable parametrization function is given as input to the algorithm.

5.2.3 Muon momentum scale and resolution calibration at $\int \mathcal{L}\, dt = 10\, pb^{-1}$ using Z resonance

From a generated sample[2], a set of 21 000 Z boson decays to muon pairs, with no background events, are reconstructed using CMS software, leading to 5 000 Z candidates, the expected statistics for the signal after 10 pb^{-1} of integrated luminosity. Both the CRAFT based scenarios were applied for the reconstruction of Z mass: global muon tracks (GLB) are used for muon identification, but only their matching Tracker track (GLBtk) is taken for the reconstruction of the invariant mass. The effects on the invariant mass are visible in the peak position and width of the distibution in Figure 5.6. The di-muon generated mass peak is 300 MeV lower than the nominal mass of the Z because of the QED final state radiation. Furthermore, a comparison between the different kinds of reconstructed muons is shown in the Figure 5.7, assuming an ideal and misaligned geometry (*Startup* misalignment for the muon system and *Realistic* for the Tracker). Even using design geometry, there are biases in the mass shape: they are of the same order for GLB and GLBtk muons, as the Tracker dominates the resolution for muons at the $M_Z/2$ scale. The stand-alone muons (STA), instead, produce a wider spread, as a consequence of the muon system misalignment introduced and also because of the stand-alone reconstruction uses a constraint to the vertex and the precision of the vertex reconstruction is degraded by Tracker

[2]Generated with PYTHIA, at $\sqrt{s} = 10\,\text{TeV}$, including Z and γ production and their decay into muon pair (`MSEL=0, MSUB(1)=1, MSTP(43)=3, MDME(184,1)=1`).

misalignment. Furthermore additional effects are introduced by the worse resolution provided by Muon system (by design construction) with respect to the Tracker one.

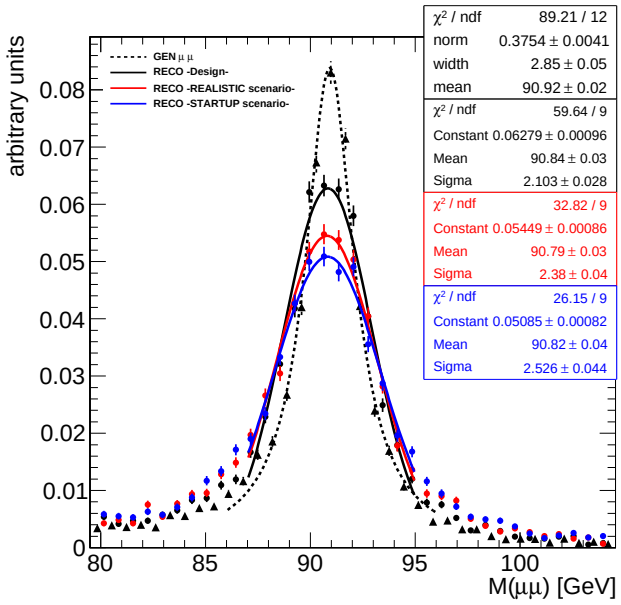

Figure 5.6: *Reconstructed Z mass using inner Tracker tracks of global muon (GLBtk) pairs, using different misalignment conditions. Parameter refers to a gaussian fit in the range [87,95] GeV. For reference, the mass distribution using generated μ fitted with a Breit-Wigner in the range [86,96] GeV is shown. Results are shown for a collected statistics after* $\int \mathcal{L}\, dt = 10\, pb^{-1}$.

Already the reconstruction chain introduces biases, as visible in the mass shape produced using design geometry, but the main effects, consisting in a shift of the peak and a visible worsening of the mass resolution, come from the introduction of the misalignment scenarios. An evidence of the good quality reached in the Tracker alignment, using only cosmic tracks collected during CRAFT, is given by the fact that resolution from the *Realistic* scenario, modeled on CRAFT data, approaches the one obtained using the design geometry.
A calibration of the muon momentum scale and resolution was necessary to remove all the possible shifts and biases surviving in the geometry. As described in the *MuScle* fit approach, a suitable ansatz function to correct the muon momentum is required and this is built after having checked the dependence of the reconstructed mass from the muon kinematic variables.

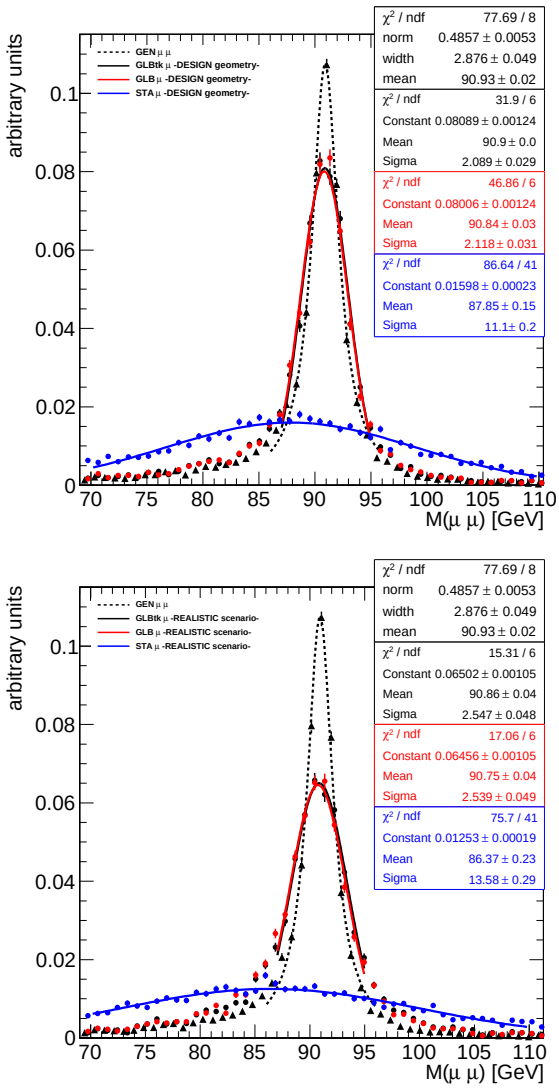

Figure 5.7: *Top plot. Reconstructed Z mass assuming ideal conditions for Muon and Tracker systems using GLBtk muons (black line), GLB muons (red line) and STA muons (blue line). Bottom plot. Distribution of the dimuon mass the condition of Startup misalignment for the muon system and Realistic for the Tracker: using GLBtk muons (black line), GLB muons (red line) and STA muons (blue line). Parameters refer to a Gaussian fit in the range [85,96] GeV. For reference, the mass distribution using generated μ fitted with a Breit-Wigner in the range [86,96] GeV is shown. Results are shown for collected statistics after* $\int \mathcal{L}\, dt = 10\, pb^{-1}$.

For example, the application of the *Startup* scenario in the reconstruction led to a bias in the dependence of the mass versus the transverse momentum, pseudorapidity and the azimuth of the muon. Moreover the azimuthal dependence appears to be different for positive and negative charged muons (Figure 5.10). The charge-dependent momentum asymmetry can be the consequence of possible systematic rotation of the layers introduced by the misaligned geometry. The effects are not symmetrically propagated to the momentum of both muons, being dependent from the inverse of the *sagitta* of the track. Therefore different absolute values of the parameters for positive and negative charged muons can be reasonably found at the end of the calibration procedure. The best choice of the ansatz function correcting the muon momentum scale identified after a trial and error procedure, was found to be:

$$p'_T = F(\phi,\eta)p_T = (a_0 + a_4|\eta| + a_5\eta^2)p_T + \begin{cases} a_1 sin(a_2\phi + a_3)p_T & \text{for } \mu^+ \\ a_6 sin(a_7\phi + a_8)p_T & \text{for } \mu^- \end{cases} \tag{5.5}$$

where the azimuthal dependence is treated differently for positive and negative charge sign, giving in total nine parameters to be determined. Likelihood minimization process of the fit provide a set of parameters with small statistical uncertainty as reported in Table 5.2: absolute values of the parameters are slightly different between negative and positive charged muons.

parameter	**value**
a_0	0.994847 ± 0.00004
a_1	-0.0010 ± 0.0005
a_2	0.75 ± 0.04
a_3	0.0003 ± 0.001
a_4	0.0032 ± 0.0001
a_5	0.0036 ± 0.0001
a_6	-0.0036 ± 0.0006
a_7	1.33 ± 0.01
a_8	0.000003 ± 0.000007

Table 5.2: *Resulting parameters from MuScle fit using the ansatz function of Equation 5.5 for correcting the muon momentum scale, exploiting the Z mass as reference. Values are intended as correction to p_T, expressed in GeV.*

An attempt to measure the resolution on the muon transverse momentum was also performed: the choice of the ansatz function was done on the basis

of a study of resolution obtained comparing the reconstructed muon momentum and the generated one. The resolution estimated via the Monte Carlo truth shows a linear dependence on the tranverse momentum itself, as expected from the description in Section 2.1. Furthermore there is a parabolic dependence on the pseudorapidity, with different parameters in different detector regions. The final choice of the ansatz function for fitting the resolution on the muon transverse momentum is:

$$\frac{\sigma_{p_T}}{p_T} = b_0 + b_1 p_T + \begin{cases} b_2\eta^2 & |\eta| < 1.4 \\ (|\eta| - b_3) + b_4(|\eta| - b_3)^2 & \eta > 1.4 \\ b_5(|\eta| - b_6) + b_7(|\eta| - b_6)^2 & \eta < -1.4 \end{cases} \tag{5.6}$$

leading to small uncertainties on the parameter values found by the algorithtm, as reported in Table 5.3. The calibration of both scale and resolution

parameter	**value**
b_0	0.001 ± 0.001
b_1	0.00024 ± 0.00002
b_2	0.0103 ± 0.0005
b_3	1.48 ± 0.02
b_4	0.123 ± 0.001
b_5	-0.023 ± 0.004
b_6	1.53 ± 0.01
b_7	0.1440 ± 0.0006

Table 5.3: *Resulting parameters from MuScle fit using the ansatz function of Equation 5.6 for measuring the muon momentum resolution, exploiting the Z mass as reference. Values are intended as correction to p_T, expressed in GeV.*

at the same time, allows for a better handling of correlations between parameters and provides the best results in terms of corrections found. In Figure 5.8 is shown the fit capability of recovering scale bias if the correct ansatz function is used. Moreover the resolution parametrization using fitted parameters matches the one observed in the mass distribution after the scale corrections. The dependence of the muon momentum resolution as a function of η is also shown: the parametrization found for the resolution fits very well the trend in the endcap and in the overlap region ($|\eta| > 0.8$) and is very close to the reconstructed one after scale correction in the central region ($|\eta| < 0.8$). The reconstructed mass before and after the scale corrections as a function of muon kinematics variables can be also seen in the Figure 5.10: after the correction the biases in the reconstructed mass as a function of ϕ and η are not significative anymore.

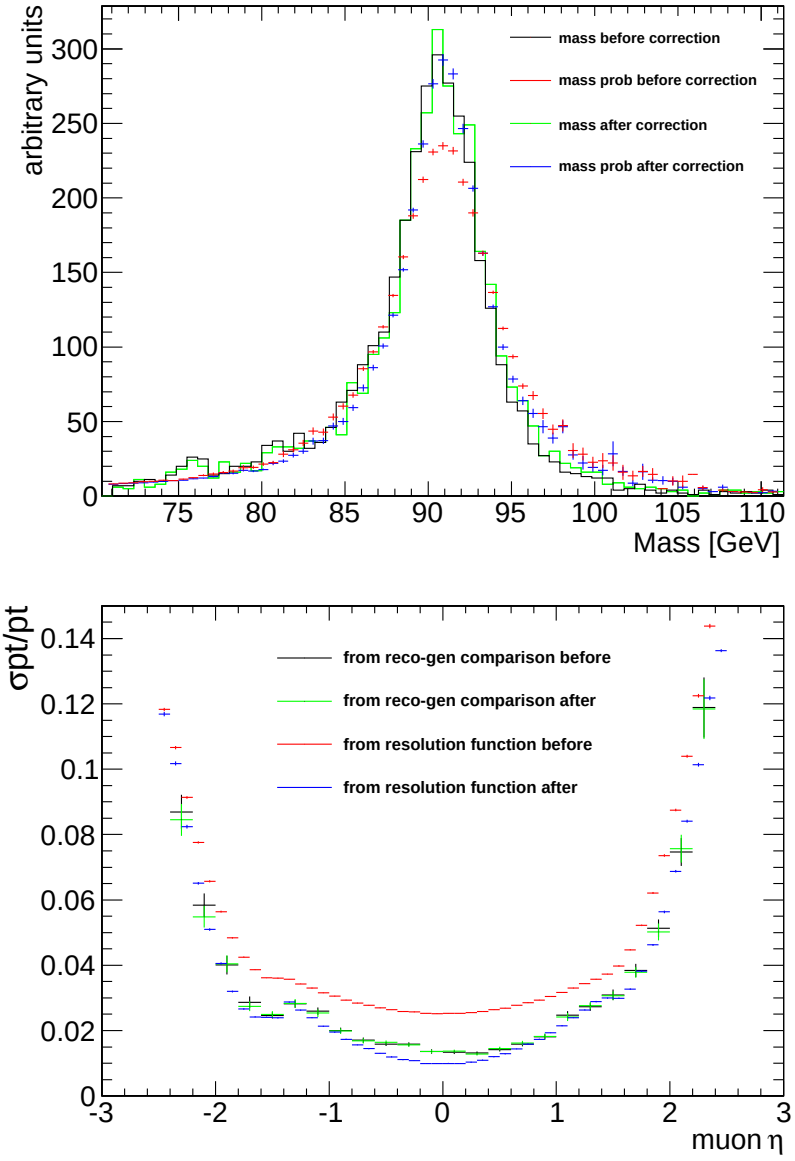

Figure 5.8: *Upper plot. Results of fitting scale and resolution of Z boson in a single MuScle fit pass. Black histogram shows the mass distribution before any corrections and should be compared to the red one showing the likelihood values as a function of mass in the sample. After the fit and correction, mass distribution P becomes the green histogram and matches better with the blue histogram which is the probability function after using final values of the fit parameters. Lower plot. Same color code to illustrate the p_T resolution as a function of muon pseudo-rapidity. Results refer to* $\int \mathcal{L}\, dt = 10\, pb^{-1}$.

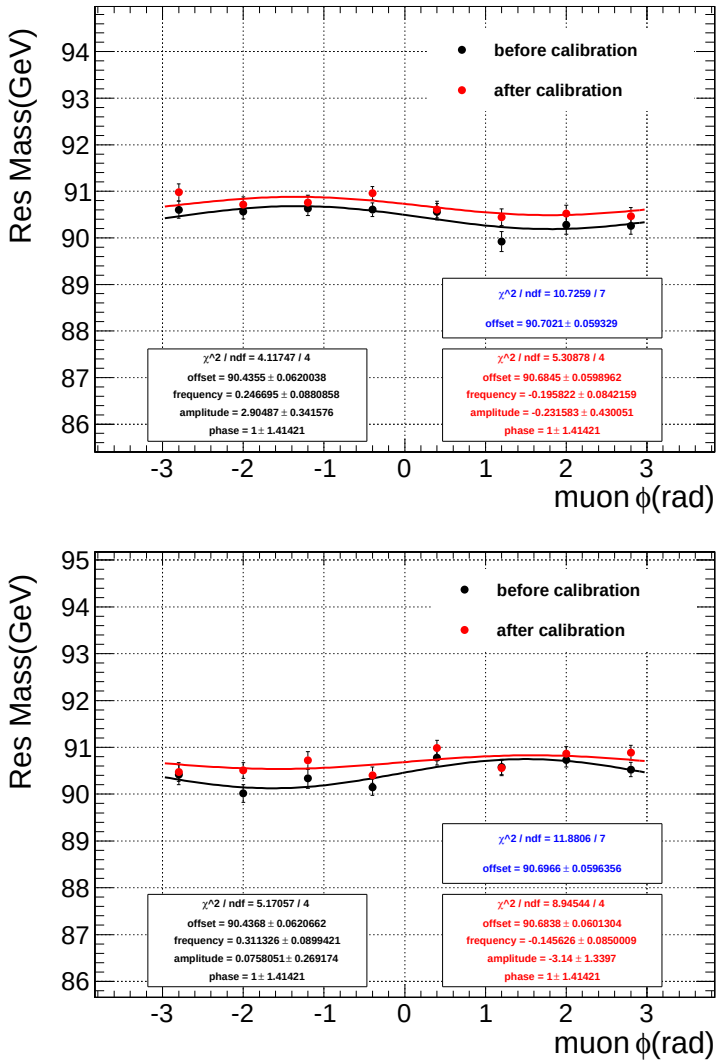

Figure 5.9: *Average Z mass in bins of muon ϕ for positive (top) and negative (bottom) charged muons, computed before (black) and after (red) the muon momentum scale and resolution calibration. In the plots the parameters of both a linear (blue box) and sinusoidal (red box) fit after calibration are reported. Only the sinusoidal one is drawn. Results refer to* $\int \mathcal{L}\, dt = 10\, pb^{-1}$.

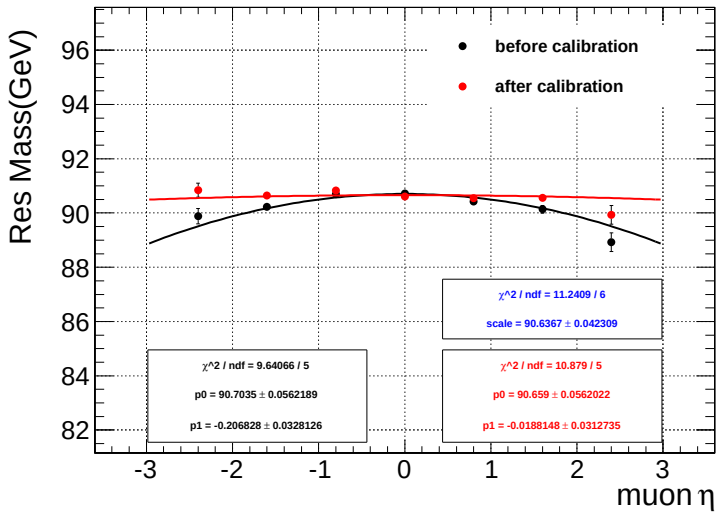

Figure 5.10: *Average Z mass in bins of muon η up, computed before (black) and after (red) the muon momentum scale and resolution calibration. In the plots the parameters of both a linear (blue box) and parabolic (red box) fit after calibration are reported. Only the parabolic one is drawn. Results refer to* $\int \mathcal{L}\, dt = 10\, pb^{-1}$.

5.2.4 Muon momentum scale and resolution calibration at $\int \mathcal{L}\, dt = 10\, pb^{-1}$ using Υ resonance

As for the study with Z boson, a set of generated Υ decays to muon pairs[3], without background events, are reconstructed using CMS software, giving a total of 86 000 events, representing the expected statistics after 10 pb^{-1} of integrated luminosity. For this study the applied scenario is chosen to be the *Realistic* one, which should reflect better the real displacement of the modules inside the Tracker. The tracks from Υ decay are typically softer than those from the Z decay and therefore most of the hits are in the Tracker system. Related to this, the study of the Υ resonance is more sensible to the misalignment of the Tracker, even if the main contribution in the determination of the momentum resolution for low p_T muon comes from the effects of the Tracker material budget. Figure 5.11 illustrates the effect of the introduction of both scenarios on the Υ mass reconstruction.

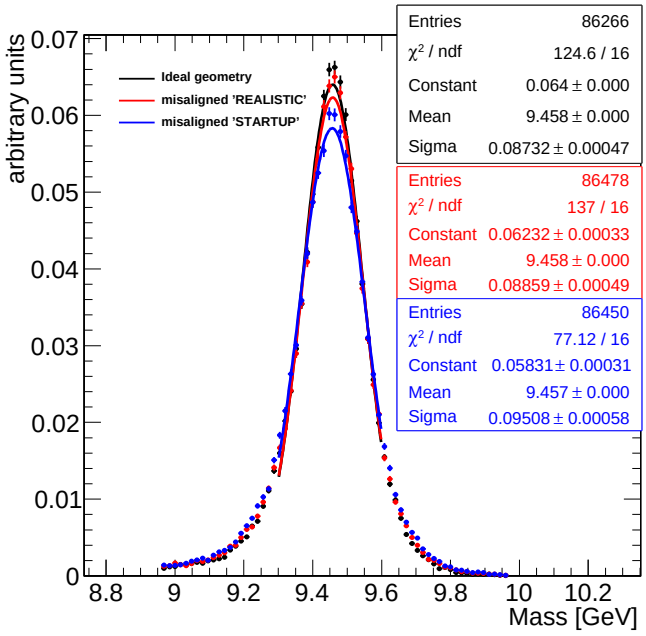

Figure 5.11: *Reconstructed Υ mass using inner Tracker tracks of global muon (GLBtk) pairs, using different misalignment conditions. Parameter reported in the statistics boxes are the outcomes of a gaussian fit in the range [9.3,9.6] GeV. Results are shown for collected statistics after $\int \mathcal{L}\, dt = 10\, pb^{-1}$*

[3] Υ production and its decay into muon pair was generated using PYTHIA at $\sqrt{s}$ = 10 TeV (`MSEL=62, MDME(1035,1)=1`).

The mass resolution using both scenarios is worse than in the ideal case, with the *Realistic* scenario approaching anyway the performance given by the design geometry. Also in this case *MuScle* fit was used to calibrate the scale and resolution of the muon momentum. As already observed, the resolution worsening due to the application of the *Realistic* scenario is small and very close to the ideal scenario. An ansatz function for the resolution has been constructed in order to have a linear dependence in p_T and "point-by-point" values for η. Those values, constant for each bin of η have been extracted from a single muon generator ("particle gun") by comparing the reconstructed values with the Monte Carlo truth, in ideal detector conditions (Figure 5.12).

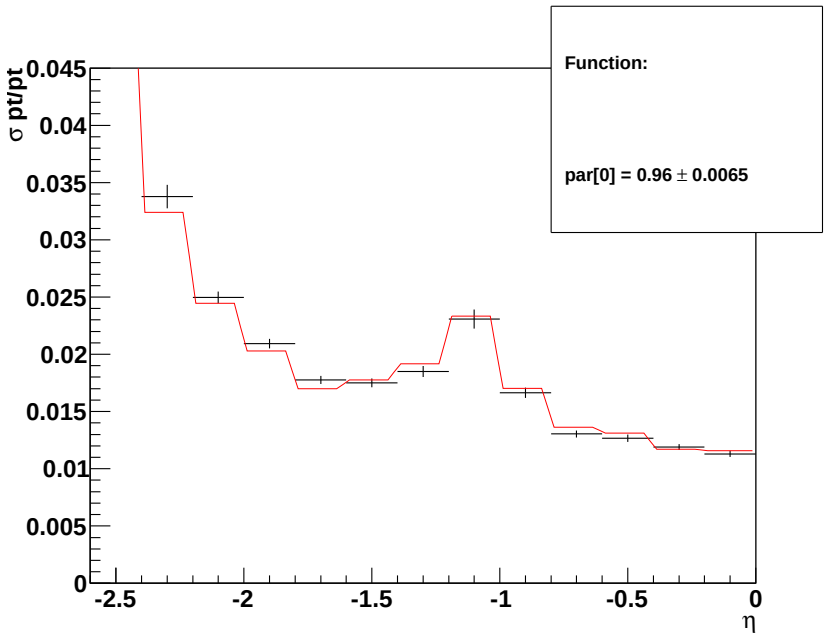

Figure 5.12: *Relative resolution on p_T versus η for global muon, as determined from Gaussian fits to the difference between true and reconstructed values in muon gun simulation. Values are intended as correction to p_T and therefore expressed in GeV.*

In the bottom plot of Figure 5.14 is visible the relative resolution versus transverse momentum dependence: also the non linear trend in the low p_T region is well determined using the probability function after the corrections. According to the mass trend observed as a function of the muon kinematic variables (η, ϕ, p_t), in the second pass a scale correction is performed using the following ansatz function and results are reported in Table 5.4:

$$p'_T = F(\phi,\eta)p_T = (a_0+\frac{a_9}{p_T}+a_4|\eta|+a_5\eta^2)p_T+\begin{cases} a_1 sin(a_2\phi+a_3)p_T & \text{for } \mu^+ \\ a_6 sin(a_7\phi+a_8)p_T & \text{for } \mu^+ \end{cases} \tag{5.7}$$

parameter	**value**
a_0	0.999689 ± 0.000002
a_1	-0.178 ± 0.003
a_2	0.000965 ± 0.000009
a_3	3.126220 ± 0.000005
a_4	0.000140 ± 0.000007
a_5	0.000092 ± 0.000002
a_6	0.0112 ± 0.0009
a_7	-0.036 ± 0.003
a_8	-0.007 ± 0.004
a_9	0.00669 ± 0.00004

Table 5.4: *Resulting parameter from MuScle fit for the ansatz function used for the resolution parametrization. Values are intended as correction to p_T, expressed in GeV.*

Again the azimuthal dependence appears to be charge-dependent: the values of the corrections found for amplitude (a_1 and a_6) and frequency (a_2 and a_7) of the parametrized sinusoidal are significantly different between positive and negative charged muons.
Figure 5.13 shows as the parabolic dependence in η is well replaced by a constant trend after the corrections, while along ϕ the sinusoidal amplitude is only partially reduced, being anyway closer to zero with respect to the situation before the correction. As shown in Figure 5.14, the bias is quite well recovered also versus p_T. In particular in the low transverse momentum region, the hyperbolic dependence on p_T of the function described before allows for a better correction of the mass values, being now closer to the nominal one.

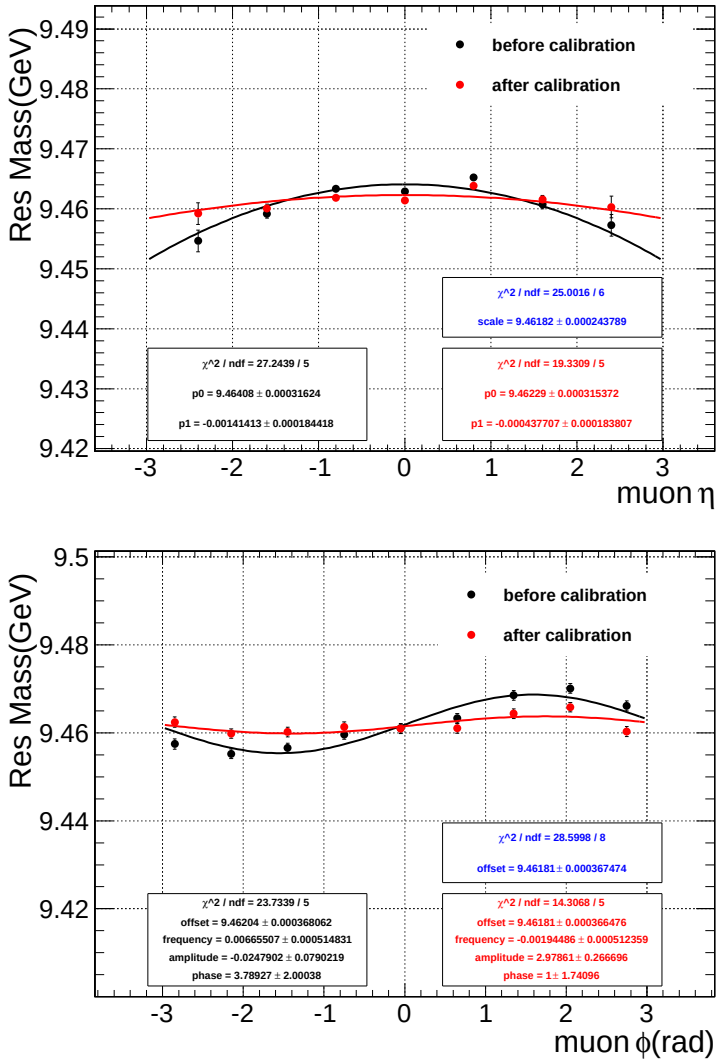

Figure 5.13: *Average* Υ *mass as in bins of muon* η *(up) and* ϕ *(bottom), computed before (black) and after (red) the muon momentum scale and resolution calibration. In the plots, both resulting parameters of linear (blue box) and sinusoidal or parabolic (red box) fit after calibration are reported. Only the sinusoidal/parabolic one is drawn. Results refer to* $\int \mathcal{L}\, dt = 10\, pb^{-1}$.

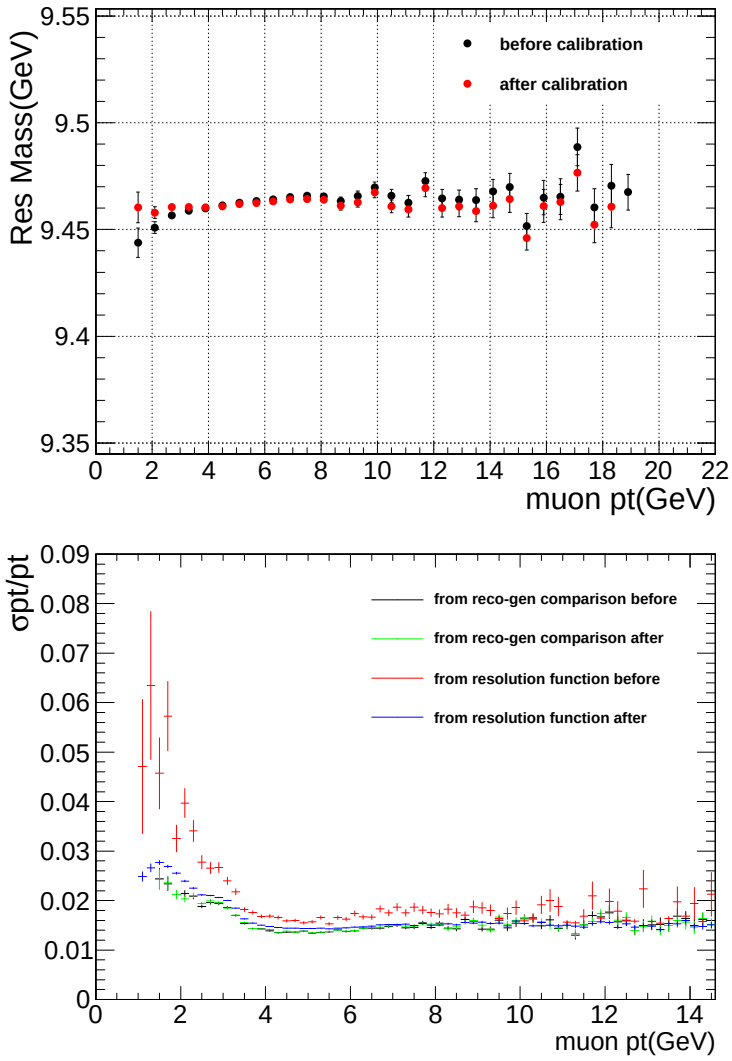

Figure 5.14: *Upper plot: average* Υ *mass as a function of muon* p_T*, computed before (black) and after (red) the muon momentum scale and resolution calibration. Lower plot: relative momentum resolution calculated from resolution function (red and blue corresponding to the results before and after corrections) and from the comparison between reconstructed and generated muons (black and green corresponding to the results before and after corrections). Results refer to* $\int \mathcal{L}\, dt = 10\, pb^{-1}$.

Appendix A

Presigma values used for global method alignment strategy at CRAFT

The Millepede algorithm foresees the possibility to assign χ^2 penalties, the so called *presigma*. By default all *global* parameters (the alignment parameter $\mathbf{p}$ of Equation 3.2) appearing in `Pede` input files with their labels are assumed to be variable parameters with initial value zero, and used in the fit. Initial values different from zero, the presigma σ_p, may be assigned to these parameters and they are internally interpreted as parameter status:

- $\sigma_p > 0$ The parameter is *variable* with the given initial value. A term $1/\sigma_p^2$ is added to the diagonal matrix element of the global parameter to stabilize a perhaps poorly defined parameter. This addition should not bias the fitted parameter value, if a sufficient number of iterations is performed (it may however bias the calculated error of the parameter).
- $\sigma_p = 0$ The parameter is *variable* with the given initial value.
- $\sigma_p < 0$ The parameter is defined as *fixed*: the initial value of the parameter is used in the fits.

Presigma values are defined with respect to last iteration within Millepede, hence also alignment corrections significantly larger than the presigmas of a global parameter can still occur in the final iteration. Assigning presigmas does improve the stability of the solution of the matrix equation, thereby avoiding numerical problems.
Too small presigmas can bias solution towards initial geometry rather than to the χ^2 minimum, while too large ones lead to random pick in the solution space and numerical problems.
In the alignment strategy using cosmic rays adopted at CRAFT several tuning procedure were needed to find the best set. To give an idea of their

magnitude, final values for module and module unit level for the different subdetectors are reported in this Appendix. The `alignParams` string contains the type of alignable and the correspondent parameter (respectively u, v, w, α, β, γ,) activated (1 means active, 0 disactivated) to which `presigma` value is applied. Values for translation are expressed in cm, while rotation in rad. TIB values for modules differ for almost a factor 2 between u and v direction, as expected from the different mounting precision along this two coordinates.

```
PresigmaCRAFT = cms.PSet(
   Presigmas = cms.VPSet(cms.PSet(

 #### Pixel

      presigma = cms.double(0.0050),
       Selector = cms.PSet(
           alignParams = cms.vstring('PixelHalfBarrelDets,111000')
       )
   ),
       cms.PSet(
           presigma = cms.double(0.002),
           Selector = cms.PSet(
               alignParams = cms.vstring('PixelHalfBarrelDets,000111')
           )
       ),
         cms.PSet(
           presigma = cms.double(0.005),
           Selector = cms.PSet(
               alignParams = cms.vstring('PXECDets,111000')
           )
       ),
       cms.PSet(
           presigma = cms.double(0.002),
           Selector = cms.PSet(
               alignParams = cms.vstring('PXECDets,000111')
           )
       ),

 #### TIB

       cms.PSet(
           presigma = cms.double(0.0100),
           Selector = cms.PSet(
               alignParams = cms.vstring('TIBDets,101000')
           )
       ),
       cms.PSet(
           presigma = cms.double(0.0200),
           Selector = cms.PSet(
               alignParams = cms.vstring('TIBDets,010000')
           )
         ),
       cms.PSet(
           presigma = cms.double(5e-04),
           Selector = cms.PSet(
               alignParams = cms.vstring('TIBDets,000010')
           )
       ),
```

```
        cms.PSet(
            presigma = cms.double(2e-04),
            Selector = cms.PSet(
                alignParams = cms.vstring('TIBDets,000101')
            )
        ),

       cms.PSet(
            presigma = cms.double(0.0100),
            Selector = cms.PSet(
                alignParams = cms.vstring('TrackerTIBModuleUnit,101000')
            )
        ),
        cms.PSet(
            presigma = cms.double(0.0200),
            Selector = cms.PSet(
                alignParams = cms.vstring('TrackerTIBModuleUnit,010000')
            )
        ),
         cms.PSet(
            presigma = cms.double(5e-04),
            Selector = cms.PSet(
                alignParams = cms.vstring('TrackerTIBModuleUnit,000010')
            )
        ),
        cms.PSet(
            presigma = cms.double(2e-04),
            Selector = cms.PSet(
                alignParams = cms.vstring('TrackerTIBModuleUnit,000101')
            )
        ),

#### TID

       cms.PSet(
            presigma = cms.double(0.0050),
            Selector = cms.PSet(
                alignParams = cms.vstring('TIDDets,111000')
            )
        ),

        cms.PSet(
            presigma = cms.double(5e-04),
            Selector = cms.PSet(
                alignParams = cms.vstring('TIDDets,000110')
            )
        ),
        cms.PSet(
            presigma = cms.double(2e-03),
            Selector = cms.PSet(
                alignParams = cms.vstring('TIDDets,000001')
            )
        ),

       cms.PSet(
            presigma = cms.double(0.0050),
            Selector = cms.PSet(
                alignParams = cms.vstring('TrackerTIDModuleUnit,111000')
            )
        ),

        cms.PSet(
```

```
            presigma = cms.double(5e-04),
            Selector = cms.PSet(
                alignParams = cms.vstring('TrackerTIDModuleUnit,000110')
            )
        ),
        cms.PSet(
            presigma = cms.double(2e-03),
            Selector = cms.PSet(
                alignParams = cms.vstring('TrackerTIDModuleUnit,000001')
            )
        ),

#### TOB

        cms.PSet(
            presigma = cms.double(0.0050),
            Selector = cms.PSet(
                alignParams = cms.vstring('TOBDets,111000')
            )
        ),
       cms.PSet(
            presigma = cms.double(5e-04),
            Selector = cms.PSet(
                alignParams = cms.vstring('TOBDets,000110')
            )
        ),
        cms.PSet(
            presigma = cms.double(2e-03),
            Selector = cms.PSet(
                alignParams = cms.vstring('TOBDets,000001')
            )
        ),
        cms.PSet(
            presigma = cms.double(0.0050),
            Selector = cms.PSet(
                alignParams = cms.vstring('TrackerTOBModuleUnit,111000')
            )
        ),
        cms.PSet(
            presigma = cms.double(5e-04),
            Selector = cms.PSet(
                alignParams = cms.vstring('TrackerTOBModuleUnit,000110')
            )
        ),
        cms.PSet(
            presigma = cms.double(2e-03),
            Selector = cms.PSet(
                alignParams = cms.vstring('TrackerTOBModuleUnit,000001')
            )
        ),

#### TEC

        cms.PSet(
            presigma = cms.double(0.0050),
            Selector = cms.PSet(
                alignParams = cms.vstring('TECDets,111000')
            )
        ),

        cms.PSet(
            presigma = cms.double(5e-04),
```

```
            Selector = cms.PSet(
                alignParams = cms.vstring('TECDets,000110')
            )
        ),
        cms.PSet(
            presigma = cms.double(2e-03),
            Selector = cms.PSet(
                alignParams = cms.vstring('TECDets,000001')
            )
        ),

        cms.PSet(
            presigma = cms.double(0.0050),
            Selector = cms.PSet(
                alignParams = cms.vstring('TrackerTECModuleUnit,111000')
            )
        ),

        cms.PSet(
            presigma = cms.double(5e-04),
            Selector = cms.PSet(
                alignParams = cms.vstring('TrackerTECModuleUnit,000110')
            )
        ),
        cms.PSet(
            presigma = cms.double(2e-03),
            Selector = cms.PSet(
                alignParams = cms.vstring('TrackerTECModuleUnit,000001')
            )
        ))
)
```

Appendix B

More on systematic misalignment studies

In addition to the the studies presented in Section 4.4, other systematic distorsions for a cylindrical geometry have been investigated and reported here for completeness. Only aligned modules are shown in the geometry comparison plots.

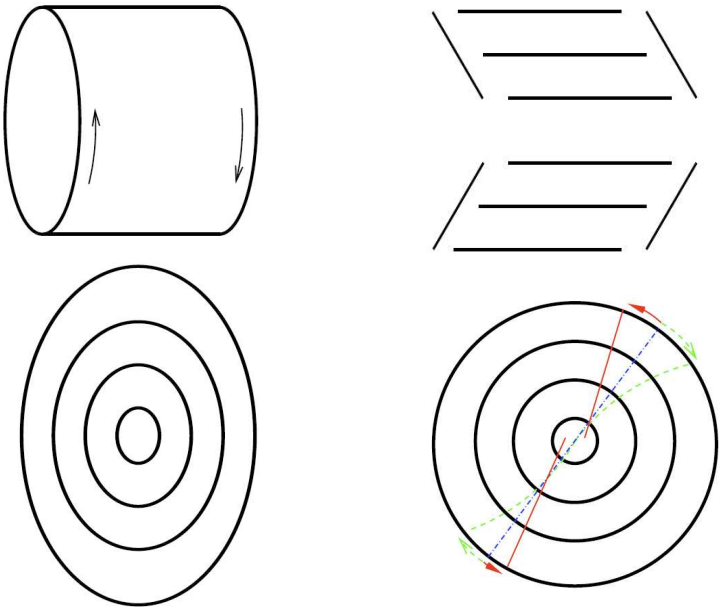

Figure B.1: *Schematic illustration of some χ^2 invariant weak mode: barrel* twist *(top left), barrel* telescope *(top right),* elliptical *(bottom left),* curl *(red) and* sagitta *(green) (bottom right) [24]*

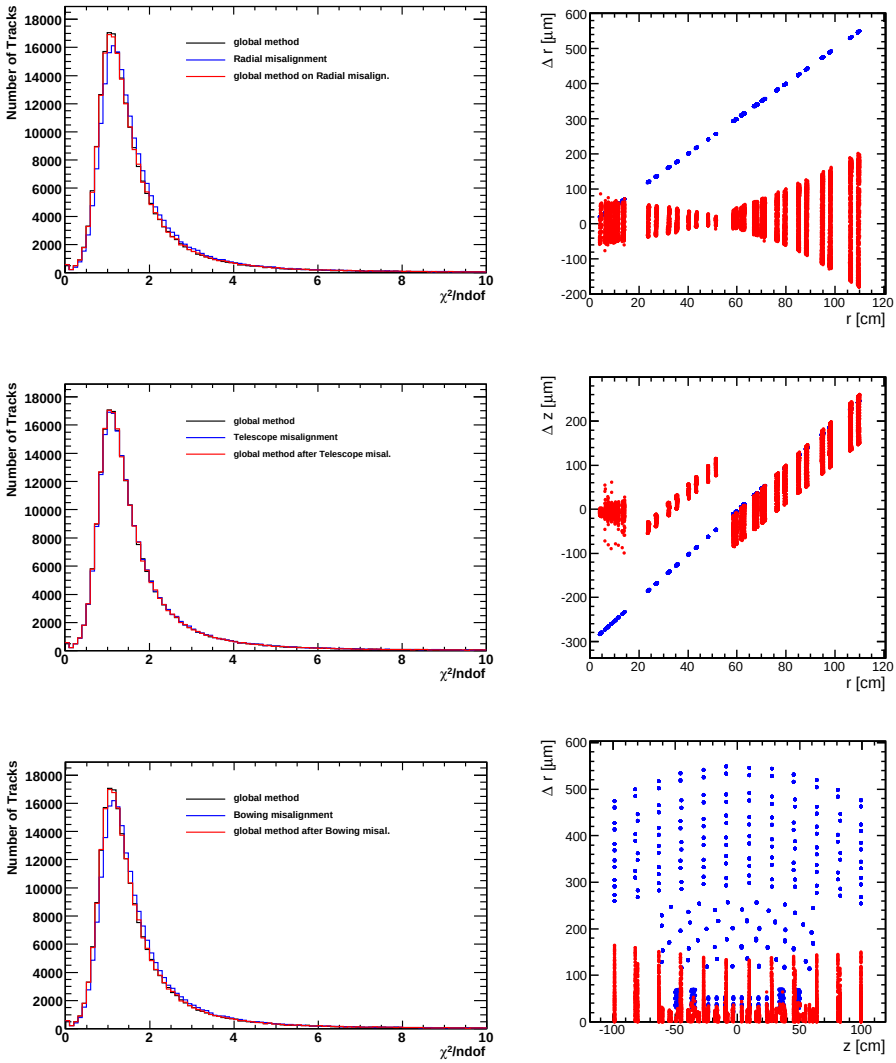

Figure B.2: *Left column.* χ^2/ndf *of the reconstructed tracks with different geometries, aligned with global method (black line), misaligned with the systematic mode (blue line), re-aligned with the global method on top of the misalignment (red line). Right column. Deviations of the modules in the barrel (TIB and TOB) with respect to the starting aligned geometry after the applied systematic misalignment (blue points) and after the alignment on top of it (red points). From top to bottom, three different modes are reported: Radial expansion, Telescope, Bowing. Only TIB, TOB and Pixel modules are shown.*

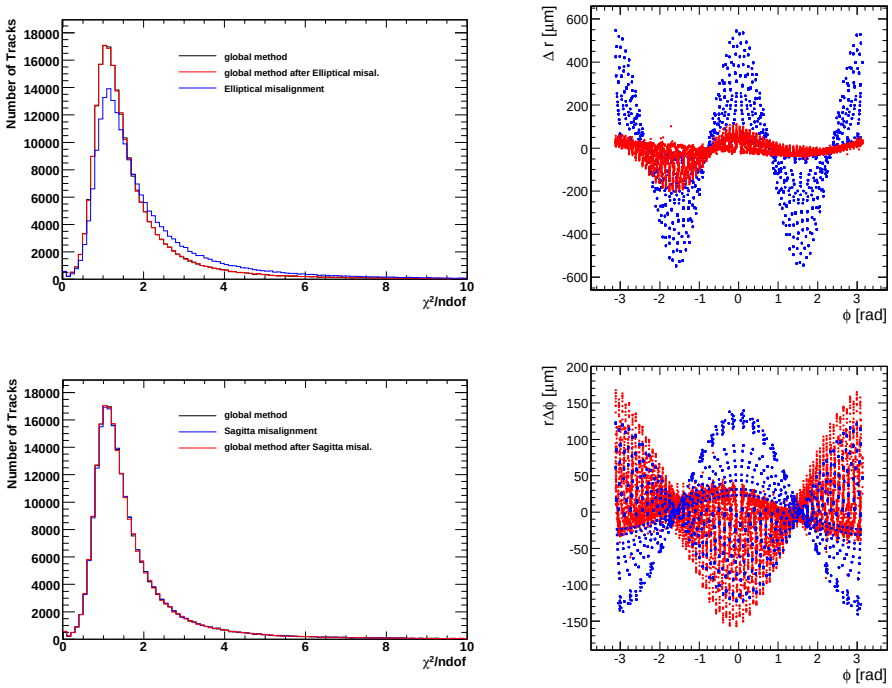

Figure B.3: *Left column.* χ^2/ndf *of the reconstructed tracks with different geometries, aligned with global method (black line), misaligned with the systematic mode (blue line), re-aligned with the global method on top of the misalignment (red line). Right column. Deviations of the modules in the barrel (TIB and TOB) with respect to the starting aligned geometry after the applied systematic misalignment (blue points) and after the alignment on top of it (red points). From top to bottom, the two remaining modes are reported: Elliptical distorsion and Sagitta. Only TIB, TOB and Pixel modules are shown.*

The plots show as in general some distorsions, like the *bowing* of the Tracker barrel structure and the *elliptical* deformation, can be partially recovered through alignment with cosmic ray tracks. On the other hand, deformations like *radial* expansion appear to be almost unsensitive to the variation of the χ^2, despite the misplacements of the modules after the misalignment. The *sagitta* mode, as it is constructed, has its maximum amplitude at 0 and π radiants, where the cosmic flux is quite reduced with respect to the slices at $\pm\pi/2$ where the detector has the most illuminated region. Anyway the

shape is recovered for TIB and Pixel modules, while the modulation is still present for the TOB modules.
In general for almost all the deformation examined, the normalized χ^2 distribution after the re-alignment (red-line) is back to the original shape before the misalignment (black line): in those cases the remaining scatter after the re-alignment on top of the misaligned geometry can be interpreted as the residual weak modes amplitude.
Only tracks from LHC beam interactions will provide better sensitivity to those systematic deformations.

Summary

The challenging demands of the Compact Muon Solenoid detector for the measurement of the particles momentum, led to design an extremely complex inner tracking system. The unknown position of the 15 000 independent modules is one of the main source of systematic error affecting the muon momentum measurement, and consequently the related physics observables. This thesis presents the main achievements obtained in the study of the Tracker detector performance, focusing on the alignment of the system using the only available source of data before the collision phase, the cosmic ray muons.
During several months of operation at Tracker Integration Facility in the Spring and Summer of 2007, about five million cosmic track events were collected with a partially active CMS Tracker. Despite the unavailability of the magnetic field for the measurement of muon momentum, encouraging results were already obtained. The comparison with simulation shows that the achieved alignment precision in the barrel part of the Tracker leads to residual distributions similar to those obtained with a random misalignment of 50/80 μm RMS in the outer/inner part of the barrel.
However at the nominal detector performance, the track based alignment procedure is expected to reduce the module position uncertainties of the level of few microns. The first occasion to operate with the magnetic field on was the Cosmic Run at Four Tesla in the Fall of 2008. The adopted strategy provided a resulting measured position for the Tracker components which significantly improved the reconstruction of the tracks. The precision of the detector position has been derived from the distribution of the median of the cosmic muon tracks residuals to be $3 - 4\,\mu$m RMS in the barrel region and $4 - 15\,\mu$m in the endcaps in the most sensitive coordinate with respect to particle trajectories. A detailed study using cosmic track sample on the remaining correlated displacements of the sensors, the so called *weak* modes, provided evidence of insensitivity to some systematic deformations, like expansion along global z axis or global z movements for different regions of ϕ. However, the study shows also as deformations along the sensitive $r\phi$ coordinate can be detected and even recoverd using only the available cosmic track topology.
The impact of the remaining misalignment after alignment with cosmic rays,

properly modeled by a misalignment scenario has been evaluated on a sample of simulated resonance decays, $Z \rightarrow \mu\mu$ and $\Upsilon \rightarrow \mu\mu$ expected after $\int \mathcal{L}dt = 10$ pb^{-1}. Exploiting an existing method based on a multivariate likelihood approach, the momentum scale corrections of the muons due to the application of both random and systematic misalignment scenario, has been evaluated, modeled and properly corrected.

In conclusion, performances obtained after the alignment, together with the muon momentum scale correction of its possible remaining effects, reveal as the CMS Tracker is ready to perform the first accessible physics measurements during the collision phase, which started out in December 2009.

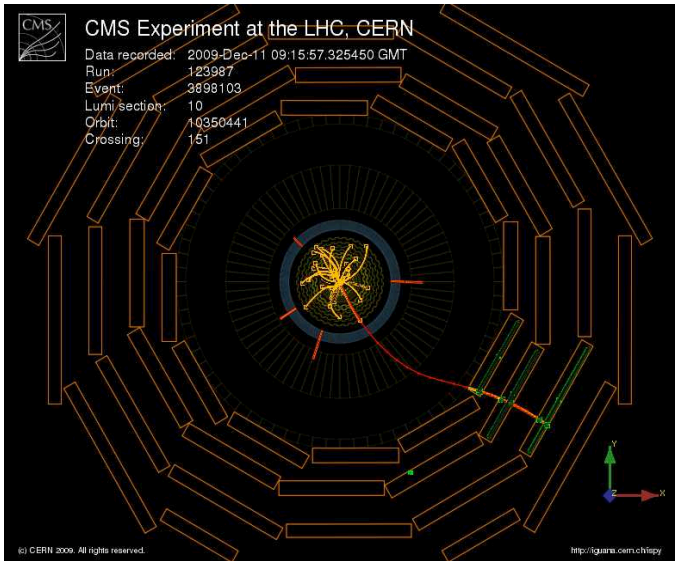

Figure B.4: 11^{th} *December 2009. First muon detected by CMS produced from pp collision at* $\sqrt{s} = 900\,\text{GeV}$. *The Tracker geometry used in the reconstruction is the one obtained after alignment with cosmic rays during CRAFT.*

Bibliography

[1] S. L. Glashow, *Partial-symmetries of weak interactions*, Nucl. Phys. 22, pg.579-588 (1961);

[2] S. Weiberg, *A Model of Leptons*, Phys. Rev. Lett. 19, pg.1264-1266 (1967);

[3] A. Salam, *Weak and Electromagnetic Interactions*, Elementary Particle Theory pg.367-377, Proceedings Of The Nobel Symposium, Stockholm, Sweden (1968);

[4] P. W. Higgs, *Spontaneous Symmetry Breakdown without Massless Bosons*, Phys. Rev. 145, pg.1156-1163 (1966);

[5] The LEP collaboration, the LEP electroweak working group and the SLD Heavy Flavour Group, *A Combination of Preliminary Electroweak Measurements and Constraints on the Standard Model*, LEPEWWG/2003-01 (2003); `http://lepewwg.web.cern.ch/LEPEWWG/`;

[6] The LHC study group, *LHC the Large Hadron Collider: conceptual design*, CERN/AC/95-05 vol.II (1995);

[7] J. M. Campbell et al., *Hard interactions of quarks and gluons: a primer for LHC physics*, Rep. Prog. Phys. 70, pg.89-193 (2007);

[8] H. L. Lai et. al., *Improved Parton Distributions from Global Analysis of Recent Deep Inelastic Scattering and Inclusive Jet Data*, Phys. Rev. D55, 1280, e-print: `hep-ph/9606399` (1997);

[9] C. Amsler et al. (Particle Data Group), Physics Letters B667, 1 (2008) and 2009 partial update for the 2010 edition;

[10] A. D. Martin et al. *Uncertainties of predictions from parton distributions I: Experimental errors*, Eur. Phys. J. C 28 pg.455 (2003);

[11] J. Pumplin et al. *New Generation of Parton Distributions with Uncertainties from Global QCD Analysis*, JHEP 2002-07:012, `arXiv:hep-ph/0201195v3` (2002);

[12] *HERA and LHC: a Workshop on the Implication of HERA for LHC Physics*, e-print: `hep-ph/0601012` (2004-2005);

[13] H. T. Haber et al. *The search for Supersimmetry: probing physics beyond the Standard Model*, Physics Report 117, pg.75 (1985);

[14] The CMS collaboration, *Detector performance and software*, Physics Technical Design Report, Vol. I, CERN/LHC 2006-001, CMS TDR 8.1 (2006)

[15] R. Adolphi et al., *The CMS experiment at the CERN LHC*, JINST **0803** (2008) S08004 [JINST **3** (2008) S08004];

[16] The CMS collaboration, *The Tracker Project*, Technical Design Report, CERN/LHC 1998-006, CMS TDR 5 (1998);

[17] M. Raymond et al., *The CMS Tracker APV25 0.25 mm CMOS Readout Chip*, Proceedings of the 6^{th} workshop on electronics for LHC experiments, Krakow, Poland (2000);

[18] R. Frühwirth, *Application Of Kalman Filtering to Track and Vertex Fitting*, Nucl. Instrum. Meth. A 262, pg.444 (1987);

[19] W. Adam et al., *Stand-alone Cosmic Muon Reconstruction Before Installation of the CMS Silicon Strip Tracker*, e-Print: `arXiv:0902.1860` (2009);

[20] O. Brandt, *Alignment of the ATLAS Inner Detector Tracking System*, `http://cdsweb.cern.ch/record/1187846/files/ATL-INDET-SLIDE-2009-176.pdf`;

[21] V. Blobel, C. Kleinwort *A New Method for the High-Precision Alignment of Track Detectors*, Proceedings of the Conference on Advanced Statistical Techniques in Particle Physics, Durham (UK), e-print: `hep-ex/0208021`, March 2002;

[22] C. C. Paige and M. A. Saunders, *Solution of sparse indefinite system of linear equations*, SIAM, Numerical Analysis 12, page 617-623, (1975);

[23] V. Blobel, *Software alignment for tracking detectors*, Nucl. Instrum. Meth. **A 566** (2006) 5, http://www.desy.de/~blobel/Mptwo.tgz;

[24] M. Stoye, *Calibration and alignment of the CMS silicon tracking detector*, DESY-THESIS-2007-026, CERN-THESIS-2007-049, (2007);

[25] V. Karimäki, T. Lampen, F.P. Schilling, *The HIP Algorithm for Track Based Alignment and its Application to the CMS Pixel Detector*, CMS NOTE-2006/018, (2006);

[26] D. N. Brown, A. V. Gritsan, Z. J. Guo, D. A. Roberts, *Local Alignment of the BABAR Silicon Vertex Tracker*, Nucl. Instr. Methods Phys. Res. **A 603**, 467, 2009;

[27] E. Widl, R. Frühwirth and W. Adam *A Kalman Filter for Track-based Alignment*, CMS-NOTE-2006-022;

[28] R. Adolphi et al., *The 2008 CMS Computing, Software and Analysis Challenge*, CMS IN-2008/044;

[29] W. Adam et al., *Alignment of the CMS Silicon Strip Tracker during stand-alone Commissioning*, JINST **4:T07001** (2009);

[30] P. Biallass, T. Hebbeker, *Improved Parameterization of the Cosmic Muon Flux for the Generator CMSCGEN*, CMS-NOTE-2007-033;

[31] M. Boezio et al., *Energy spectra for atmospheric muons measured with the CAPRICE98 balloon experiment*, Phys. Rev. **D67** 072003 (2007);

[32] T. Lampen, N. de Filippis, F. P. Schilling, A. Schmidt, M. Weber, *Comprehensive Set of(Misalignment Scenarios for the CMS Tracker*, CMS NOTE 2008/029;

[33] The CMS collaboration, *Alignment of the CMS Silicon Tracker during Commissioning with Cosmic Rays*, accepted by JINST, arXiv:0910.2505;

[34] The CMS collaboration, *Commissioning of the CMS Experiment and the Cosmic Run at Four Tesla*, submitted to JINST, arXiv:0911.4845;

[35] The CMS collaboration, *Commissioning and Performance of the CMS Pixel Tracker with Cosmic Ray Muons*, submitted to JINST, arXiv:0911.5434;

[36] The CMS collaboration, *Commissioning and Performance of the CMS Silcon Strip Tracker with Cosmic Ray Muons*, submitted to JINST, arXiv:0911.4996;

[37] R. Castello, *The calibration of muon momentum scale in the CMS detector*, CMS CR-2009-306, Proceeding of XXIX International Symposium on Physics in Collision 2009, Kobe, Japan;

[38] R. Castello et al., `https://twiki.cern.ch/twiki/bin/viewauth/CMS/MuonScaleCalib`;

[39] S. Bolognesi, *Muon Detection in CMS: from the Detector Commissioning to the Standard Model Higgs Search*, CMS TS-2009-020 ;

[40] T. Sjöstrand, S. Mrenna and P. Skands, *PYTHIA 6.4 physics and manual*, JHEP 05 (2006) 026, e-print: `hep-ph/0603175`;